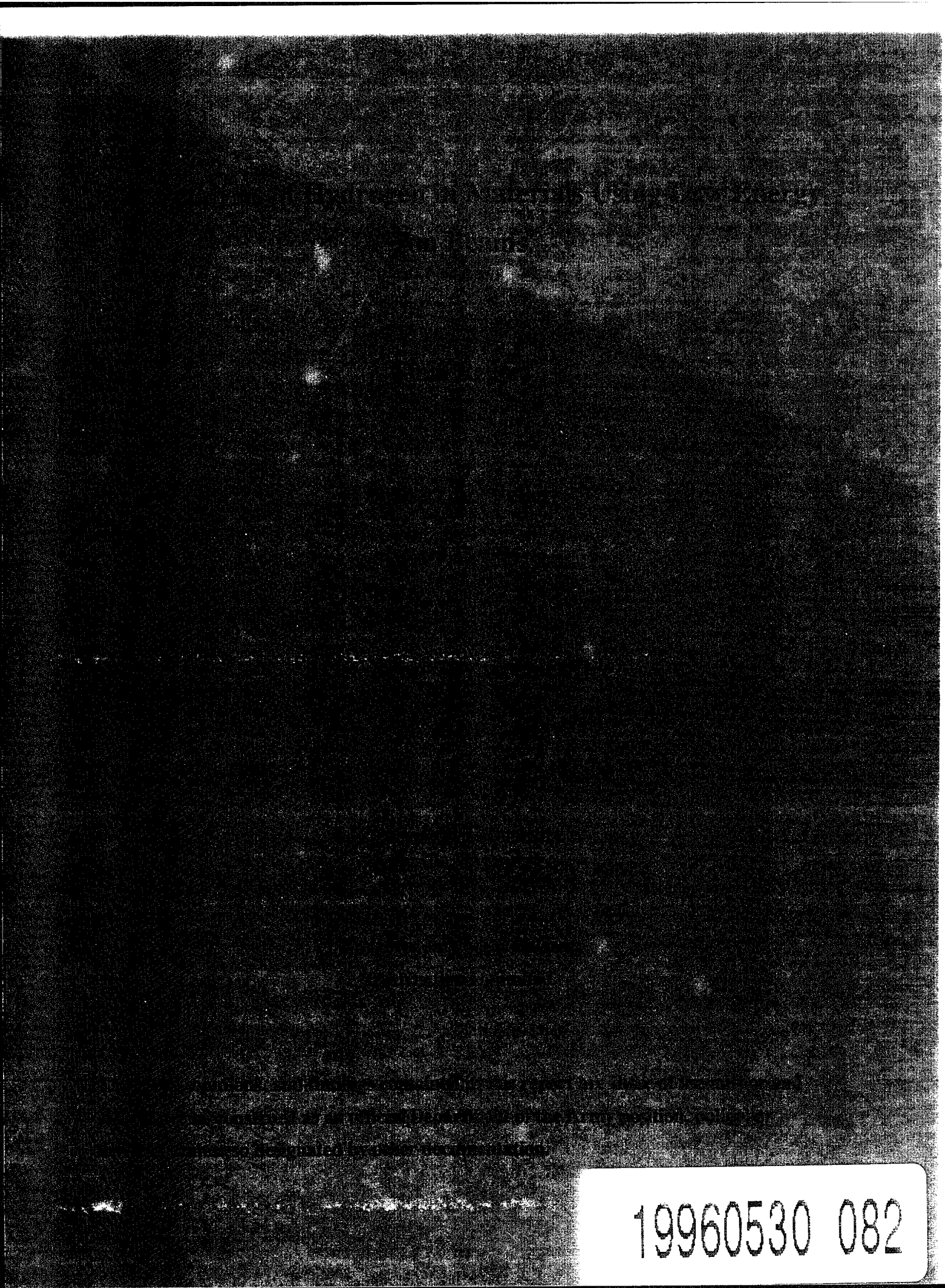

REPORT DOCUMENTATION PAGE

Form Approved
OMB NO. 0704-0188

1. AGENCY USE ONLY *(Leave blank)*	2. REPORT DATE	3. REPORT TYPE AND DATES COVERED
	April 15, 1996	Final 1 Mar 92 - 28 Feb 96

4. TITLE AND SUBTITLE

The Analysis of Hydrogen in Materials Using Low Energy Ion Beams

5. FUNDING NUMBERS

DAAL03-92-G-0037

6. AUTHOR(S)

Robert A. Weller

7. PERFORMING ORGANIZATION NAMES(S) AND ADDRESS(ES)

Vanderbilt University
Nashville, Tennessee 37235

8. PERFORMING ORGANIZATION REPORT NUMBER

9. SPONSORING / MONITORING AGENCY NAME(S) AND ADDRESS(ES)

U.S. Army Research Office
P.O. Box 12211
Research Triangle Park, NC 27709-2211

10. SPONSORING / MONITORING AGENCY REPORT NUMBER

ARO 29071.16-MS

11. SUPPLEMENTARY NOTES

The views, opinions and/or findings contained in this report are those of the author(s) and should not be construed as an official Department of the Army position, policy or decision, unless so designated by other documentation.

12a. DISTRIBUTION / AVAILABILITY STATEMENT

Approved for public release; distribution unlimited.

12 b. DISTRIBUTION CODE

13. ABSTRACT *(Maximum 200 words)*

Medium energy backscattering and forward recoil spectrometry have been developed into powerful quantitative analytical tools during the course of this research. This final report reviews the technical accomplishments of the project as well as several applications which have been undertaken in support of other related research.

14. SUBJECT TERMS

hydrogen, ion beam analysis, Rutherford backscattering, recoil spectrometry, Langmuir-Blodgett films, depth profiling

15. NUMBER IF PAGES

156

16. PRICE CODE

17. SECURITY CLASSIFICATION OR REPORT	18. SECURITY CLASSIFICATION OF THIS PAGE	19. SECURITY CLASSIFICATION OF ABSTRACT	20. LIMITATION OF ABSTRACT
UNCLASSIFIED	UNCLASSIFIED	UNCLASSIFIED	UL

The Analysis of Hydrogen in Materials Using Low Energy Ion Beams

Final Report

Robert A. Weller

April 15, 1996

U. S. Army Research Office

DAAL 03-92-G-0037

Vanderbilt University
Nashville, Tennessee

1. Foreword

Although there were a number of earlier, elegant examples of the use of nuclear techniques for materials analysis, the field began in earnest around 1970 with the wide application of Rutherford backscattering spectrometry to study issues of importance in semiconductor manufacturing. While other charged-particle spectrometers were available, the tool of choice for this work was the silicon surface barrier detector, which had been developed and perfected during the previous decade. The surface barrier detector is an invention which is so well suited to its purpose, so practical, and so relatively inexpensive that its appearance essentially eliminated competing technologies for backscattering spectrometry. In nuclear physics, however, there were instances, particularly involving heavy ions, where surface barrier detectors alone were not sufficient or even appropriate. In order to measure both the mass and energy of nuclear reaction products, particle telescopes combining time-of-flight and energy spectrometers were developed. In 1989, Marcus H. Mendenhall and I realized that similar time-of-flight spectrometers could be used for backscattering and forward-recoil spectrometry with primary ions in the energy range from about 50 keV to 500 keV that before had not been widely used for materials analysis. It soon became apparent that this approach had the potential to provide information about thin films which was not accessible by conventional methods.

2. Table of contents

3. Technical report[†]

3A. Statement of the Problem

The objective of this project was to optimize the equipment for high-resolution, time-of-flight medium energy particle-scattering spectrometry, to identify and investigate scientific issues relating to the performance of the time-of-flight spectrometer, and to explore its use for the sensitive detection of hydrogen on surfaces, emphasizing particularly the concurrent measurement of hydrogen and other low-atomic-mass constituents such as carbon and oxygen which cannot readily be accomplished by other hydrogen measurement techniques such as nuclear reaction analysis. Issues of particular importance included depth resolution, maximum analyzable depth, and sensitivity of the technique for hydrogen, optimum values of parameters such as incident projectile mass and energy, and experimental determination of the intrinsic efficiency of the spectrometer as a function of energy and mass of the particle being analyzed.

3B. Summary of important results

All of the basic objectives of the project were accomplished and are documented in the publications produced during the course of this work, copies of which are included in the Appendix. Rather than repeat details found there or in previous progress reports, I will attempt here to give a broad overview of the significance of the findings.

Spectrometer design and technology

At the beginning of the project, two physical designs of the time-of-flight spectrometer were under consideration. The first comprised of a separate start and stop detector with normal to the carbon foil tilted at an angle of 30° with respect to the spectrometer axis. This design had a known deficiency insofar as the tilt of the foil resulted in different trajectories having slightly different path lengths. A second design had the carbon foil mounted perpendicular to the spectrometer axis and used the same microchannel plate to detect both secondary electrons from the foil transit and the subsequent arrival of the heavy ion. Although the latter design had

---

[†] References refer to the numbered list of publications appearing in section 3C.

an appealing simplicity, early tests showed it to be inferior to the former. In all subsequent work, we have used the version with a separate start and stop detector.

Important engineering advances in spectrometer design included a more robust and easily serviced start foil assembly and a scheme to permit us to operate commercial microchannel plate assemblies with grounded cathodes. The latter was achieved through a combination of a novel ultra-high vacuum flange and a commercially-manufactured microwave circuit for which Prof. Mendenhall received a patent. By operating the start detector with grounded cathode we were able to reduce the bias on the carbon foil to the range of 300-400 V and thereby to greatly improve the quality of isolated peaks in spectra which had previously been degraded by splitting caused by charge exchange in the foil. Other important technical advances included the installation of an extremely effective Faraday enclosure for accurate charge integration and, late in the project, the installation of a three axis goniometer to enable us to make more effective use of target orientation as an experimental parameter. Both of these devices were obtained through financial support from Texas Instruments, Inc.

During the course of this research, we joined with a group at Sandia National Laboratories to design and build a special, high-sensitivity instrument for the analysis of trace contaminants on semiconductor surfaces. This work was conducted under the sponsorship of Sematech and resulted in the establishment of a user facility at Sandia for Sematech member companies. Although the goal of high sensitivity was incidental to the primary objectives of this project, the effort nevertheless demonstrated an extremely important technological application of medium energy backscattering. In addition, we are using experience which we gained working with large-diameter microchannel plates to improve future versions of our general-purpose spectrometers.

Finally, we note a design improvement conceived toward the end of the project for which a proof of concept was obtained both by computer simulation and a preliminary experiment. This involved the issue of resolution degradation attributable to the tilt of the start foil. We realized that, by judiciously tilting the stop detector with respect to the spectrometer axis, we could not only reduce path-length dispersion within the spectrometer but also actually cancel some of the kinematic dispersion due to the finite size of the spectrometer's entrance aperture

[13]. The further refinement of this idea is an objective of our current ARO project which is builds upon the research described herein.

Spectrometer physics

Perhaps the most important single outcome of this research was not envisioned at the time that the proposal was written. We knew from simple considerations that the efficiency of the spectrometer (defined as is the probability that a particle entering the spectrometer along a valid trajectory would produce a valid event) was not unity and was almost certainly energy dependent. We had assumed that it would be necessary to use empirical curves to account for this, and one important task envisioned for the project was measuring these empirical curves for all important ions, including H, He, C, N, O and probably Ne and Ar, in the energy range of interest. However, as the work progressed it became increasingly clear that, with a detailed knowledge of the physics of the various process which occur in the spectrometer, mathematical modeling should be possible [6,8].

The culmination of this effort was our prediction using our model that the variation in efficiency for detecting hydrogen should be qualitatively different from that for other low mass ions by having a clear maximum in the energy region of interest to us. The experimental observation of this behavior provided convincing confirmation of the essential features of the model [8]. While the model is complete enough, in principle, to provide *a priori* estimates of spectrometer efficiency without adjustable parameters, in practice, the input variables are sufficiently uncertain to make this impractical. We prefer to use the model as a tool for interpolating experimental values. Even so, it dramatically reduces the effort necessary to calibrate the spectrometer. We believe that our work constructing and verifying this model, together with contributions on spectral shape and the sensitivity of medium energy backscattering [1,4,10], are among the most important outcomes of this project, because they can be used directly by others both to design equipment for time-of-flight spectrometry and to interpret the results of experiments. Our own work with Sandia could not have been completed successfully without the predictive power of these models.

Hydrogen measurement

Cumulative experience with forward-recoil measurements of H have established that O^{2+} and Ar^{3+} beams at 540 keV and 810 keV, respectively, are near optimum for our accelerator and scattering geometry [2,3,9,11,15,16,17]. The oxygen beam, which experiences less energy straggling and multiple scattering, is preferable for depth profiling H in Si. The argon beam gives superior results when the objective is to simultaneously measure H, C, O and N, as found, for example, in surface hydrocarbons. Using present equipment and techniques, the sensitivity for hydrogen was found to be in the range of $10^{13}/cm^2$. For abundant hydrogen in the target, a near surface depth resolution of about 6 nm was observed [16,17].

From a purely procedural standpoint, the most important element of the forward recoil measurement of hydrogen was probably charge integration. This problem received unusual attention as described above. The energy of the beam was also an issue.

While we found clear advantages in backscattering associated with He beams in the 300 keV range, this was not so for forward scattering. One of the most important advantages of recoil spectrometry, when compared, for example, with nuclear reaction analysis, is the ability to measure hydrogen and carbon simultaneously [9,11]. In order to obtain satisfactory results for carbon, it was necessary to use a very heavy ion. While we are quite pleased with the results we obtained using 810 keV Ar^{3+}, we would very much have liked to go higher. How much higher is not completely clear. However, it is easy to make an estimate. The maximum efficiency for H detection was found to be around 100 keV. Below about 50 keV the efficiency for H decreases rapidly while from 100 keV to around 300 keV it decreases by only about 20%. If the most energetic hydrogen, that scattered near the surface, had an energy of 300 keV and the beam were Ar, then the Ar energy would have to be approximately 5.7 MeV (assuming a recoil angle of 42° as in our apparatus). This energy should be accessible to the 2 MV Van de Graaff accelerator that is now being installed in the Accelerator Laboratory at Vanderbilt in conjunction with the start of Professor Len C. Feldman's research program. This accelerator will play a prominent role in the further development of medium energy forward-recoil spectrometry now being undertaken as part of ARO contract DAAH 04-95-1-0565.

Labile organic films

One of the first applications of our forward-recoil technique was to obtain hydrogen and carbon in a Langmuir-Blodgett film of interest to one of our industrial collaborators. Langmuir-Blodgett films were also of interest because of their inherent property of self-organization. Throughout this work, obtaining thin films whose composition and structure were known has been a continuing challenge. Langmuir-Blodgett films made from precursor molecules with a metallic atom at one end held the promise of being excellent examples of a single monolayers because nature assembles the layer with the metallic atoms in well-defined positions. While L-B films proved too fragile to act as single-monolayer, thin-film standards, they did serve well to define the limits of our ability to analyze very fragile structures [9]. Such films have also been used by other researchers as precursors for the production of ultra-thin protective coatings similar in some ways to ion implanted layers [9, and references therein]. We found that it was possible to determine the composition of a film with as few as 10^{11} total incident ions. We used this capability to undertake a systematic study of the effects of particle radiation on L-B films and others made of nitrocellulose [11]. Results from the latter were particularly striking because they showed clearly that N_2O groups were preferentially excised in the early stages of irradiation. This was seen directly by observing the change in total N and O as a function of dose. The measurement was obtained using less than 1 nA of 810 keV Ar^{3+} beam.

Industrial collaborations and technology transfer

During the period of this project we have had active collaborations with groups at Texas Instrument, Inc., Sandia National Laboratories, and Motorola, Inc. The Sandia project involved the development of a medium energy backscattering system optimized for ultra-sensitive, trace-element detection and was described above [10,14]. The collaborations with TI and Motorola each dealt with specific applications of backscattering spectrometry to high-resolution depth profiling. The TI project dealt with the measurement of thin oxide and oxynitride films [13]. The Motorola work involved the measurement of graded silicon-germanium layers. (The latter work has not yet been published but is being presented at the Materials Research Society in April, 1996.)

The semiconductor industry has long been the largest consumer of ion beam analytical technology. The specific characteristic of medium energy backscattering which has garnered this industrial interest is its high depth resolution when compared with conventional backscattering spectrometry. During this project, we obtained over $150k in direct support for equipment from Texas Instruments, including over $60k for a three-axis goniometer. This supplemental support was primarily for semiconductor objectives but it had an important direct and indirect impact on the project as a whole. Conversely, if this effort had not been underway, these industrial collaborations would probably not have been possible.

3C. List of publications

1. Instrumental effects on time-of-flight spectra, Robert A. Weller, Nucl. Instr. and Meth. B 79 (1993) 817-820.

2. Medium energy elastic recoil analysis of surface hydrogen, James H. Arps and Robert A. Weller, Nucl. Nucl. Instr. and Meth. B 79 (1993) 539-544.

3. Surface characterization by medium energy particle scattering, James H. Arps and Robert A. Weller, in R. E. Green, et al. ed., *Nondestructive Characterization of Materials VI*, Plenum Press, New York, 1994, pp. 781-789.

4. An algorithm for ab initio computation of small-angle multiple scattering angular distributions, Marcus H. Mendenhall and Robert A. Weller, Nucl. Instr. and Meth. B 93 (1994) 5-10.

5. Energy dependence in the degradation of calcium fluoride thin films irradiated by helium ions, Martha Riherd Weller, Mark E. Miklis and Robert A. Weller, J. Applied Physics, submitted.

6. A model of the intrinsic efficiency of a time-of-flight spectrometer for keV ions, Robert A. Weller, James H. Arps, Diane Pedersen and Marcus H. Mendenhall, Nucl. Instr. and Meth. A 353 (1994) 579-582.

7. Adaptation of particle-telescope technology for medium energy ion beam analysis, James H. Arps, Mark E. Miklis and Robert A. Weller, Rev. Sci. Instrum. 65 (1994) 1575-1579.

8. Measurement of time-of-flight spectrometer efficiency for light ions at medium energies, James H. Arps and Robert A. Weller, Nucl. Instr. and Meth. B 90 (1994) 547-551.

9. Medium energy ion beam analysis and modification of Langmuir-Blodgett thin films, J. H. Arps, R. A. Weller, Y. S. Tung and D. O. Henderson, Nucl. Instr. and Meth. B 99 (1995) 623-626.

10. The impact of spectrometer efficiency on the trace-element sensitivity of time-of-flight medium energy backscattering, Robert A. Weller, Nucl. Instr. and Meth. B 99 (1995) 491-494.

11. Time-of-flight elastic recoil analysis of ion beam modified nitrocellulose thin films, James H. Arps and Robert A. Weller, B 100 (1995) 331-335.

12. Loss of material from a Ga-In liquid surface during bombardment by hyperthermal Ta, Pt, and Au atoms, Martha Riherd Weller and Robert A. Weller, Nucl. Instr. and Meth. B 100 (1995) 444-449.

13. Analysis of a thin, silicon-oxide, silicon-nitride multilayer target by time-of-flight medium energy backscattering, Robert A. Weller, Kyle McDonald, Diane Pedersen, and Joseph A. Keenan, Nucl. Instr. and Meth. B, in press.

14. Sputtering and migration of trace quantities of transition metal atoms on silicon, Diane Pedersen, Robert A. Weller, Martha Riherd Weller, Victor J. Montemayor, J. C. Banks and J. A. Knapp, Nucl. Instr. and Meth. B, in press.

15. Effect of lithium wall conditioning on deuterium in-vessel retention in the TdeV tokamak, B. Terreault, H. Y. Guo, D. Kéroack, R. W. Paynter, W. W. Zuzak, G. Abel, M. Ennaceur, J.-L. Gauvereau, E. Haddad, L. Leblanc, G. G. Ross, H. H. Mai, N. Richard, B. L. Stansfield, TdeV Team, M. Caorlin, D. K. Owens, D. Mueller, S. Pitcher, P. H. La Marche, J. D. Strachan, J. H. Arps and R. A. Weller, J. Nucl. Mater. 220-222 (1995) 1130-1134.

16. Determination of the hydrogen sensitivity and depth resolution of medium-energy, time-of-flight forward recoil spectrometry, James H. Arps and Robert A. Weller, Nucl. Instr. and Meth., submitted.

17. The measurement of low-mass surface constituents by medium energy time-of-flight forward recoil spectrometry, James H. Arps, Ph.D. Thesis, Vanderbilt University, 1995.

3D. List of participating scientific personnel

1. Robert A. Weller, Associate Professor of Materials Science and Associate Professor of Physics, Vanderbilt University.

2. Marcus H. Mendenhall, Associate Director, Vanderbilt Free Electron Laser Center.

3. Martha Riherd Weller, Associate Professor of Physics, Middle Tennessee State University.

4. Victor J. Montemayor, Associate Professor of Physics, Middle Tennessee State University.

5. James H. Arps, Ph.D. (Dr. Arps's degree was earned while working on this project. He is now a staff member at Southwest Research Institute, San Antonio, Texas.)

6. Kyle McDonald, graduate student. (Mr. McDonald will take his Ph.D. qualifying exam in August, 1996.)

7. Diane Pedersen, graduate student.

8. Mark E. Miklis, summer undergraduate research assistant.

9. Ivan E. Milosavljevic, summer undergraduate research assistant.

10. Laura B. Bussa, summer undergraduate research assistant.

4. Report of inventions

During the course of this work Dr. Marcus H. Mendenhall filed a patent disclosure with Vanderbilt's patent office covering the method which was devised to operate the start microchannel plate at ground potential. Subsequently, a patent for this was issued by the U. S. Patent Office.

5. Appendix

This appendix contains the collected works supported by this project with the exception of the doctoral thesis of James H. Arps. For convenience, they have been numbered to correspond with the list of publications above.

1. Instrumental effects on time-of-flight spectra

Nuclear Instruments and Methods in Physics Research B79 (1993) 817–820
North-Holland

NIM B
Beam Interactions with Materials & Atoms

Instrumental effects on time-of-flight spectra *

Robert A. Weller
Vanderbilt University, Nashville, Tennessee, USA

Using two detectors to time individual scattered particles, time-of-flight, medium-energy backscattering has established a new standard for depth resolution by ion backscattering and has been suggested as a means to measure very low levels of contamination on semiconductor surfaces. This paper sets forth a criterion for backscattering sensitivity to trace contaminants based upon the limit imposed by sputtering and analyzes the implications of random coincidence background in time-of-flight spectra for reaching this theoretical limit. The effects of high count rates on spectral shape are discussed as are the effects of the quantum efficiencies of start and stop detectors. An integral equation relating an intrinsic spectrum and the corresponding measured data set is presented along with its formal solution.

1. Introduction

The scattering cross section for 200 keV $^{12}C^{+}$ on Fe at 150° is over 700 times larger than the comparable cross section for 2 MeV $^{4}He^{+}$. This very large increase in cross section, together with technical advances in the energy spectrometry of backscattered ions in this energy range, has raised the possibility that medium energy backscattering, particularly with heavy ions, may be a superior means of detecting very low levels of trace impurities in semiconductors. Following this reasoning, Knapp and Doyle [1] have developed a technique using surface barrier detectors preceded by range foils which they call HIBS (heavy ion backscattering spectrometry) specifically aimed at very high sensitivity trace element analysis at surfaces, while Mendenhall and Weller [2], following a somewhat more general line, have developed a time-of-flight approach to medium energy backscattering (MEBS) which emphasizes both resolution and sensitivity.

The ultimate sensitivity of both the time-of-flight and range foil techniques is limited by similar physical processes. Two of the most important are multiple scattering, by which ions with energies higher than is kinematically possible from a single collision are reflected from the target, and sputtering, by which all atoms of interest are eventually removed from the target. Brice has recently completed a theoretical investigation of multiple scattering relevant to this application [3]. In this paper, I suggest a criterion for the limit of sensitivity to trace elements which is imposed by sputtering and present a mathematical model of a time-of-flight spectrometer which may be used to calculate the random coincidence background which, along with sputtering, limits the sensitivity of the time-of-flight approach.

In Chu, Mayer, and Nicolet [4], the standard reference on backscattering spectrometry, the authors do not quantify the limit of sensitivity of backscattering which is imposed by sputtering. However, a more recent text by Feldman and Mayer [5] does consider the issue. These authors assume that the total erosion by the incident beam must be less than the original film thickness for a statistically significant measurement. This is a useful estimate but one which contains a subtle ambiguity which arises because the degree of erosion is not connected more directly with the statistical uncertainty of the measurement. Consider, for example, the meaning of a result with 10% counting statistics (100 counts) when 100% of the target layer has been removed during the measurement. A more consistent estimate of sensitivity can be obtained if the fraction of the trace constituent which is sputtered away during the backscattering measurement is approximately the same as the fractional statistical uncertainty of its measured areal density. In the following section, I will quantify this sensitivity criterion and use it to assess the relative merits of MEBS with ions of several masses.

The principal source of background in a time-of-flight backscattering spectrum is random coincidences between start and stop signals which are produced by different particles. The rate of these random events is clearly related to the rate of true events and this relationship controls the signal-to-background in time-

* Supported by the U.S. Army Research Office (DAAL 03-92-G-0037). Additional support was provided by a grant from Texas Instruments, Inc.

of-flight spectra. The third section will develop the relationship between an intrinsic time-of-flight spectrum and the random background which accompanies it.

2. Sensitivity criterion

Consider a backscattering experiment to measure a surface contaminant in which the physical quantities are defined as follows. Let ρ be the areal density of the contaminant species, σ the differential scattering cross section, Ω the detector solid angle, η the detector quantum efficiency, N the number of primary ions, A the cross-sectional area of the incident beam, C the measured number of backscattered particles, B the background in the spectral region of the backscatters from all sources, P the number of sputtered contaminant atoms per primary ion, and $\epsilon = \Delta\rho/\rho$ the fraction of the contaminant layer that is removed during the measurement. The number of backscatters is:

$$C = N\sigma\rho\Omega\eta. \tag{1}$$

Similarly, the number of sputtered contaminant atoms is:

$$NP = A\Delta\rho = \rho\epsilon A. \tag{2}$$

To these well known relationships we add the condition defined above, that the statistical uncertainty in the measurement be equal to the fraction of the material removed:

$$\epsilon = \frac{\Delta\rho}{\rho} = \frac{\sqrt{C + 2B}}{C}. \tag{3}$$

From these, we obtain an expression for the sensitivity of a measurement in terms of the required fractional statistical uncertainty of the result

$$\rho^2 = \frac{1 + \sqrt{1 + 8\epsilon^2 B}}{2\epsilon^3}\,\frac{P}{A\sigma\Omega\eta}. \tag{4}$$

Of the quantities in this equation, P is the least well known. In order to estimate P, let us assume that contaminants are removed randomly in collision cascades which are dominated by the substrate atoms. In this case, one might expect that the yield of the contaminant is just the yield of the substrate reduced by the proportion of contaminant atoms in the total pool from which sputtered atoms are drawn:

$$P \approx Y_s\frac{\rho}{\rho_s}, \tag{5}$$

where ρ_s ($\gg\rho$) is the areal density of a layer of the substrate from which sputtered atoms originate; that is, a region about three atomic layers thick. With this added assumption, we arrive at the final expression for the minimum density layer given a number B of background counts and a required precision ϵ of the result:

$$\rho = \frac{1 + \sqrt{1 + 8\epsilon^2 B}}{2\epsilon^3}\,\frac{Y_s}{\rho_s A\sigma\Omega\eta}. \tag{6}$$

Table 1
Detectable level ρ of Au on Si with various 100 keV beams in the absence of background. Also shown are σ_{LJ}, the Lenz–Jensen cross section for scattering from Au at 150°, and Y_s, the sputtering yield of the Si substrate. N is the number of incident ions required for the measurement. These values are based upon assumptions that $\rho_s = 4\times10^{15}$ cm^{-2}, $A = 0.03$ cm^2, $\Omega\eta = 10^{-4}$ sr, and $\epsilon = 0.3$

Beam	σ_{LJ} [10^{-22} cm^2]	Y_s	ρ [10^9 cm^{-2}]	N [10^{15} cm^{-2}]
^{20}Ne	344	0.40	36	0.09
^{16}O	255	0.23	28	0.15
^{12}C	169	0.11	20	0.32
^{11}B	128	0.075	18	0.48
^{4}He	28	0.0046	5.1	7.8
^{1}H	8	0.00024	0.9	150

Casual intuition suggests that the increase of scattering cross section with increasing atomic number of the projectile would favor heavy ions for highest sensitivity. This conjecture is tested in table 1 which gives the level at which Au can be detected on Si with several different ions. Table 1 assumes that $\epsilon = 30\%$ (that is a non-zero result with a confidence level of three standard deviations), that $B = 0$, and that the beam energy is 100 keV. Notice that the greatest sensitivity (smallest ρ) is obtained for the lightest projectile even though the cross section is lowest in this case. The reason for this rather surprising result is that sputtering is the dominant effect. Greatest sensitivity is obtained by using light ions but at a cost of longer (often much longer) run times. Heavy ions are preferred only when constraints are placed on the allowed duration of the measurement. One would, therefore, expect that it would be desirable to use as large a beam current as possible, in order to perform the measurement in the least time. Unfortunately, as the following section shows, with time-of-flight detection it is not possible to compensate in this way, because using large beam currents drives up the background, B.

3. TOF background

Eq. (6) shows the effect of background on the best attainable sensitivity for trace element analysis. In a time-of-flight spectrometer such as is described in ref. [2], most background events occur when a start pulse and stop pulse are initiated by different particles. In

this section, I present an integral equation which describes the distortion of time-of-flight spectra which results from these random coincidences in the spectrometer. Let us assume that the true rate of particles entering the spectrometer is λ, that the normalized intrinsic distribution of flight times t is $f(t)$, and that the efficiencies of the start and stop detectors as a function of flight time are $\eta_1(t)$ and $\eta_2(t)$. We assume further that the rate of random start and stop pulses caused, for example, by electronic noise, cosmic rays, etc. can be neglected. Define the mean efficiencies of the detectors as:

$$\eta_1 = \int \eta_1(t) f(t)\, \mathrm{d}t \quad \text{and} \quad \eta_2 = \int \eta_2(t) f(t)\, \mathrm{d}t. \quad (7)$$

With these definitions, it is possible to express the mathematical form of the probability, $P(t)$, that an ion entering the time-of-flight spectrometer generates an event with flight time t, in terms of the intrinsic distribution $f(t)$ and the true event rate λ. The expression is:

$$P(t) = p\, \mathrm{e}^{-\eta_2 \lambda t}\Big[\eta_1(t)\eta_2(t) f(t) + \eta_1 \eta_2 \lambda - \eta_2 \lambda \int_0^t \eta_1(t')\eta_2(t') f(t')\, \mathrm{d}t'\Big]. \quad (8)$$

Here p is the probability that the system is not busy with a previous pulse at the time that a start pulse arrives. This expression is derived by considering all possible variations for an event. For example, the first term in the brackets corresponds to the composition of probabilities in the following sequence: 1) the particle entering the spectrometer has flight time t, $f(t)\,\mathrm{d}t$; 2) the spectrometer is not busy, p; 3) the start detector is triggered, $\eta_1(t)$; 4) no random stop occurs during the interval $(0, t)$, $\mathrm{e}^{-\eta_2 \lambda t}$; and finally; 5) the stop detector is triggered, $\eta_2(t)$.

The principal predictions of eq. (8) are that there is a component of additive random background proportional to λ and that a multiplicative exponential damping factor $\mathrm{e}^{-\lambda_2 t}$ ($\lambda_2 \equiv \eta_2 \lambda$) tends to attenuate the spectrum at long arrival times. In measured time-of-flight backscattering spectra, such as fig. 1, this attenuation is ordinarily negligible in the portion of the spectrum that has features of interest and so can be ignored. It is the rate dependent background which defeats the use of increased beam current to shorten measurement times. Fortunately, the principal constituent of the additive background, at least for the common case of analyzing heavy constituents on a lighter substrate, is $\eta_1 \eta_2 \lambda$, a constant that can be determined easily by examining regions of the spectrum which do not contain kinematically allowable backscattering events. Thus, background subtraction in time-of-flight spectra is straightforward in contrast to subtraction of pulse pile-up which is experienced in energy spectra measured with surface barrier detectors. However, as eq. (6) clearly shows, even theoretically well understood background exacts a toll in diminished sensitivity.

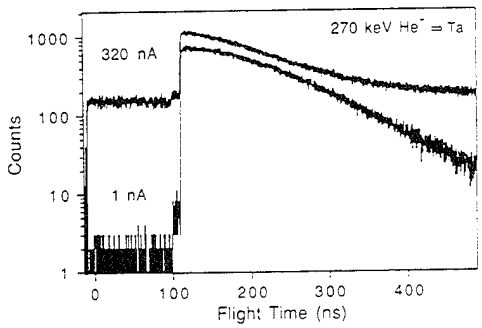

Fig. 1. Time-of-flight spectra for $^4He^+$ backscattering at 150° from a solid Ta target with the same total charge delivered by beam currents of 1 and 320 nA. The event rates were $\eta_1\lambda$ = 7500 s^{-1} and 740 ks^{-1} respectively and $\eta_2\lambda$ = 1000 s^{-1} and 320 ks^{-1} respectively. Several factors, including the uncertainty of the current integration for the 1 nA spectrum and an electronic time-out at 500 ns, complicate the quantitative comparison of these data with eq. (8). However, the trend toward higher relative background at the high event rate is clear as is the essential flatness of the background in the kinematically inaccessible region of the spectrum. The small step in the level of the background near the Ta edge is an artifact of the external electronics which has now been eliminated.

Two additional points need to be made with reference to eq. (8). First, although the background increases approximately linearly at low event rates, this is true only so long as p is near unity. At very high rates, the effect of this factor, which is discussed further below, must also be considered. Finally, even at low counting rates, it is necessary to measure the total system efficiency $\eta(t) \equiv \eta_1(t)\eta_2(t)$, which is, of course, dependent on the ion being analyzed, in order to recover $f(t)$ from a measured spectrum. This is a minor inconvenience of time-of-flight spectrometry when compared with the near unit quantum efficiency of energy spectrometry using surface barrier detectors.

Eq. (8) can be converted to a differential equation and so can be formally inverted to obtain the best achievable approximation, $\eta_1(t)\eta_2(t)f(t)$, to the true distribution, $f(t)$, from the measured distribution $P(t)$. The result is of theoretical interest but is not very useful for practical data analysis, since in a real experiment one does not ordinarily sample the distribution for a large enough range of t values. The formal inversion of eq. (8) is:

$$\eta_1(t)\eta_2(t) f(t) = p^{-1}\, \mathrm{e}^{\eta_2 \lambda t} \int_0^t \big[\eta_2 \lambda P(t') + P'(t')\big]\, \mathrm{d}t', \quad (9)$$

where P' denotes the derivative, $P(t)$ and $\eta_2\lambda$ are known from experiment, and it is assumed that $\eta_1(t)\eta_2(t)f(t) = 0$ when $t = 0$. Using the simple assumption that the detector's mean dead time τ is the mean duration of observed events, one obtains for τ:

$$\tau = \frac{\int_0^\infty tP(t)\,\mathrm{d}t}{\int_0^\infty P(t)\,\mathrm{d}t} \tag{10}$$

and, consequently, for the live time factor, p:

$$p = \frac{1}{1 + \eta_1\lambda\tau}. \tag{11}$$

This equation is, of course, only valid when $\lambda_1 \equiv \eta_1\lambda$ is not too large. The random coincidence background sets a lower limit on the sensitivity of time-of-flight measurements but, as eq. (8) shows, this background depends upon the rate of events in the stop detector. If a significant portion of the total counts in a spectrum is generated by uninteresting, low-energy particles such as backscatters from the substrate, then the signal-to-noise performance of a spectrometer can be enhanced by placing a range foil like that used by Knapp and Doyle [1] just before the stop detector. In this location, the foil introduces negligible loss of timing resolution for the particles which pass through it, and pin holes in the foil only cause an increase in the uniform background, not localized distortions in the spectrum.

4. Conclusion

Here are the principal conclusions of this paper. 1) When total measurement time is unlimited, maximum sensitivity for detecting heavy contaminants on a light substrate is obtained with light ions such as H or He rather than heavier ions such as C or Ne. 2) When run time (or total number N of incident ions) is limited, eqs. (2), (3) and (5) together imply that heavier ions are required, but from eq. (6) one then finds that less overall sensitivity can be achieved. 3) Measured time-of-flight spectra contain a flight-time-dependent efficiency factor which is independent of count rate and an approximately uniform rate dependent background. Thus, greatest sensitivity is obtained with low beam currents so long as the actual rate of detected events is a few times larger than the true electronic background. 4) An effective strategy for reducing background with minimal loss of timing resolution, and therefore increasing sensitivity to heavy trace contaminants, is to tailor the response $\eta_2(t)$ of the stop detector to reduce the rate of uninteresting backscatters from the substrate. One obvious way to do this is to place a foil in front of the stop detector which is thick enough to eliminate most particles backscattered from the substrate but thin enough to pass those which are scattered from the species of interest.

As of this writing, the only reliable method to obtain the quantum efficiency $\eta(t) = \eta_1(t)\eta_2(t)$ of a time-of-flight spectrometer is to measure it. It is clear that one factor strongly affecting $\eta_1(t)$ is the secondary electron emission of the 2–3 $\mu g/cm^2$ carbon foil which generates the electrons which trigger the start detector. Similarly, multiple scattering in this foil is very important in determining $\eta_2(t)$ since particles deflected from the axial trajectory of the spectrometer will not be detected. The degree to which the flight-time-dependent functions $\eta_1(t)$ and $\eta_2(t)$ can be predicted from first principles is presently unknown, but is the subject of active research.

References

[1] J.A. Knapp and B.L. Doyle, Nucl. Instr. and Meth. B45 (1990) 143.
[2] M.H. Mendenhall and R.A. Weller, Nucl. Instr. and Meth. B59/60 (1991) 120.
[3] D.K. Brice, Nucl. Instr. and Meth. B69 (1992) 349.
[4] W.-K. Chu, J.W. Mayer and M.-A. Nicolet, Backscattering Spectrometry (Academic Press, New York, 1978).
[5] L.C. Feldman and J.W. Mayer, Fundamentals of Surface and Thin Film Analysis (North-Holland, New York, 1986) p. 54.

2. Medium energy elastic recoil analysis of hydrogen

Nuclear Instruments and Methods in Physics Research B79 (1993) 539–544
North-Holland

NIM B
Beam Interactions with Materials & Atoms

Medium energy elastic recoil analysis of surface hydrogen

James H. Arps and Robert A. Weller
Vanderbilt University, Nashville, Tennessee, USA

We describe a technique for the detection of light mass constituents at or near the surface of a material using two microchannel detectors to time the individual recoils. Sensitivity to hydrogen is demonstrated by probing samples of Kapton, hydrated titanium, and wafer grade silicon with 270 keV helium, neon, and argon ions. Because the detector is sensitive to particle velocity rather than energy, recoil atoms and scattered ions are easily distinguished. Processes which affect the system's sensitivity to hydrogen are identified and a value for the hydrogen detection efficiency is established. The method may realize a number of advantages over conventional elastic recoil detection, including the elimination of the absorber foil, heightened sensitivity, and improved depth resolution.

1. Introduction

The greatest strength of surface analysis by ion backscattering is that the fundamental interaction cross section describing the probability of collision between the ions of the beam and the atoms of the sample is calculable from first principles. If, in addition, the species of interest is present in a thin layer at or near the surface and has an atomic mass greater than that of the bulk of the sample, then the resulting spectra are especially easy to interpret. Conversely, if the species of interest has an atomic mass lighter than the substrate upon which it rests, then backscattering spectra are difficult to interpret and the quality of the resulting data is lower. This is particularly true of hydrogen, which is invisible in backscattering spectra.

Hydrogen is present to a greater or lesser degree on almost all surfaces. Its presence in significant quantities in a material may be useful, as in the case of silicon [1] or, as in the case of titanium [2], may significantly degrade the material's performance. In either case, detecting and quantifying hydrogen, especially in small quantities, is a continuing challenge. It is, of course, invisible to electron spectroscopies, and, while it is readily observable by secondary ion mass spectrometry, these observations are virually impossible to quantify.

The most reliable quantitative techniques for measuring surface hydrogen make use of energetic ion beams. The most highly developed is nuclear resonant reaction analysis in which a beam of particles such as ^{15}N causes the specimen to emit γ radiation in proportion to the hydrogen concentration by, in this case, the nuclear reaction $^{15}N(p, \alpha\gamma)^{12}C$ [3]. Narrow resonances in the reaction are used to obtain information not only about the quantity of hydrogen present, but also its depth distribution. An alternative technique, known as elastic recoil detection (ERD), is more direct. An energetic beam is directed onto the surface to be analyzed at an oblique angle so that low angle forward recoils as well as scattered beam ions can be detected. In this way target constituents with low atomic masses are visible even when they reside on substrates with much larger atomic mass. Much of the original development of ERD used silicon surface barrier detectors for the energy spectrometry of recoiling atoms [4]. In order to effectively profile hydrogen, it was necessary to use them in conjunction with range foils to remove the scattered ions and heavy recoils. Thomas et al. [5] first observed that the correct parameter to use to differentiate particles in the forward geometry is not energy (which surface barrier detectors measure) but rather time, since lighter forward recoils move faster (up to nearly twice the speed of the incident projectiles). Using technology in common use for heavy ion nuclear spectroscopy, he showed that time-of-flight detection could produce superior depth resolution and discrimination of species when used with beam energies ranging up to a few tens of MeV.

Our group has previously demonstrated that backscattering spectrometry using time-of-flight detection and beams with energies in the range 200–300 keV is a valuable complement to conventional Rutherford backscattering (RBS) [6]. The extension of the medium energy time-of-flight technique to forward scattering is natural because a number of advantages of using lower energy beams, such as less total deposited energy and a smaller accelerator, also obviously apply

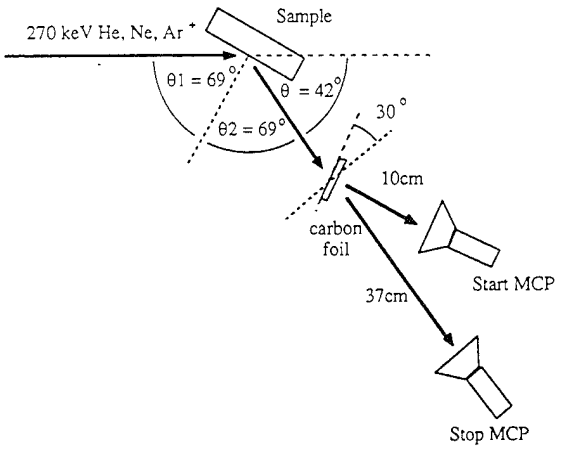

Fig. 1. Schematic of scattering geometry and detector layout.

to this case. Others, such as enhanced sensitivity and depth resolution, must be verified experimentally.

In this paper, we report preliminary measurements of hydrogen and other low mass surface species using time-of-flight medium energy elastic recoil detection. Samples of clean and hydrated titanium, etched and oxidized device-grade silicon, and Kapton have been studied. Beams of 270 keV He^+, Ne^+, and Ar^+ ions were used to study the effects of probe species on the sensitivity of the system to hydrogen. Near surface concentrations of hydrogen and oxygen have been estimated and the relative depth distributions of hydrogen in these materials are compared.

2. Experiment

The scattering and detection geometry is shown in fig. 1. Beams of singly charged He, Ne, and Ar ions were focused on the target in spots approximately 3 mm in diameter. Beam currents were typically in the 1–2 nA range with a total deposited charge of approximately 200 nC. The sample was oriented so that the scattering angle was 42° and incident and scattered angles, θ_1 and θ_2, were 69° with respect to the target normal. Both the detector and the analysis chamber were maintained at a base pressure of $\sim 1 \times 10^{-8}$ Torr.

The time-of-flight detector used for these measurements is similar to the one discussed in an earlier paper [7]. A recoil or scattered atom (charged or neutral) passes through a rotateable 3 $\mu g/cm^2$ carbon foil which is ordinarily tilted at 30° with respect to the particle's trajectory, and traverses a 36.4 cm long flight path before encountering the stop detector. The stop pulse is produced when the atom strikes a microchannel plate (Galileo ElectroOptics FTD-2003). The secondary electrons generated in the foil are accelerated to 800 eV and detected by a second microchannel plate assembly. The microchannel plate pulses are amplified and time markers are generated by constant fraction discriminators. The time markers are used to generate a time-proportional analog pulse using a time-to-amplitude converter. A multichannel analyzer converts and histograms the pulses into 2048 channel spectra. The measured timing resolution of the elastic recoil TOF system is approximately 1.5 ns. The detector solid angle, defined by a small aperture in front of the detector, was 1.5×10^{-4} sr.

The detection efficiency for hydrogen was investigated by bombarding an 8.5 $\mu g/cm^2$ carbon foil with protons with energies from 50 to 270 keV. The foil was oriented normal to the beam and scattered H was measured at $\theta = 42°$ with respect to the beam. The transmitted beam was collected by a Faraday cup and the resulting current was used, along with a correction for charge neutralization in the foil, to estabilsh the total number of incident ions. Preliminary measurements of the efficiencies for helium, carbon, and oxygen have also been studied similarly.

Samples were chosen to contain hydrogen in a range of concentrations both on the surface and in the bulk. A Kapton ($C_{22}H_{10}N_2O_4$, $\rho = 1{,}42$ g/cm^3) sample was cut to size from a 35 μm thick sheet made commercially by DuPont. Hydrated titanium was prepared from a 0.127 mm thick, 99.98% titanium foil in an electrolysis cell assembled using the titanium as the cathode and high purity graphite as the anode. The electrodes were immersed in a 0.05M solution of hy-

Table 1
Comparison of probe beams and respective parameters which affect the measurement of hydrogen in silicon. The columns from left to right indicate (1) probe beam species, (2) recoil hydrogen cross section, (3) surface recoil H flight time in the detector, (4) surface scattered beam flight time, (5) surface recoil Si flight time, (6) resolveable surface contaminants, and (7) Si normal incidence sputtering yield

Ion	$\sigma_H(42°)$ [10^{-23} cm^2]	Δt_H [ns]	Δt_{ion} [ns]	Δt_{Si} [ns]	Resolveable species	Y_{Si}
$^4He^-$	1.73	92.1	112.2	599.5	H, D	0.022
$^{20}Ne^-$	694	171.5	287.9	384.8	H, D, C	0.19
$^{40}Ar^-$	6750	239.5	641.0	385.5	H, D, C, O, F	0.84

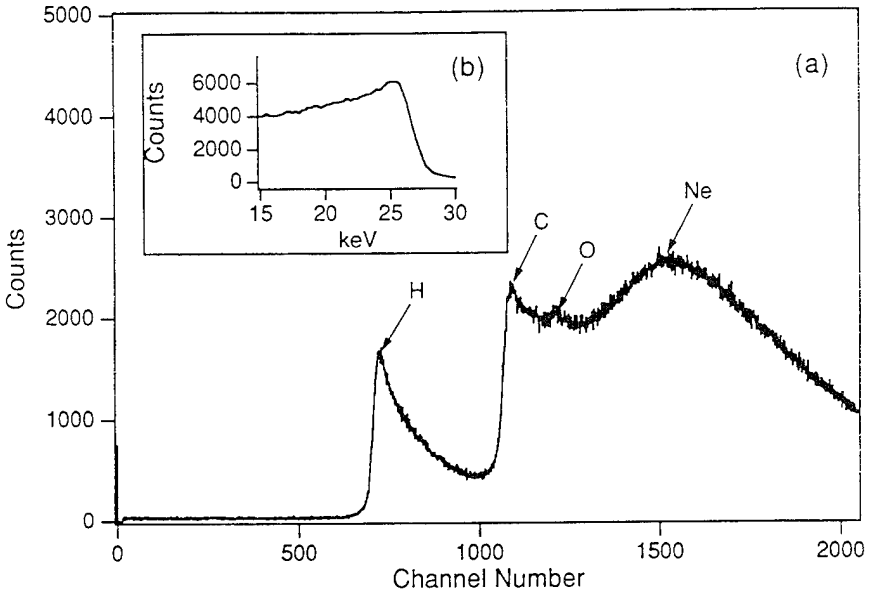

Fig. 2. (a) TOF spectra for 270 keV Ne^+ on the polymer Kapton. A total charge of 1.25×10^{13} ions was deposited during the analysis. (b) Transformed energy spectrum for recoil hydrogen in Kapton.

drochloric acid in deionized water for 3 h while a current of 100 mA at 30 V was passed between them. Two silicon samples were cut from a pristine, 6-in., device-quality wafer cleaved along the [100] surface. One sample was dipped in reagent grade hydrofluoric acid (49%) for 1 min and rinsed in deionized water for 2 min with the intent of removing the surface oxide.

3. Results and discussion

For quantitative work it is essential to know the quantum efficiency of the time-of-flight detector. We define this simply as the probability that an ion entering the detector will generate an observable event. The efficiency was determined for protons scattered from carbon based on known values for the cross section, the number of scattering centers/cm^2 and the number of incident ions. For protons the result was an efficiency of $30 \pm 5\%$ over a wide energy range. The value is comparable with other reported results [8]. Because the energy loss for protons in the carbon start foil is nearly a maximum over our range of interest, the efficiency of secondary electron emission is high. However, this is offset by multiple scattering in the start foil. A significant increase in the count rate at the stop detector was observed during a sample irradiation when the start foil was rotated out of the particle's flight path. Calculations using an independent implementation of the TRIM algorithm [9] suggest that at least half of the recoil protons in the range 25–50 keV will be scattered out of the 2° acceptance half-angle of our stop microchannel plate. Multiple scattering of an incident beam of Ne or Ar is even greater by comparison. This can be used to advantage because it limits the count rate from scattered beam ions which provide little useful information yet contribute to the background.

A comparison of the effects of the probe beam on some crucial parameters of the spectrum of hydrogen in silicon are shown in table 1. Hydrogen recoil cross sections, calculated using the Lenz–Jensen potential, favor Ne and Ar for optimal sensitivity. It should be noted that the recoil cross section using 270 keV $^{20}Ne^+$ is 5 orders of magnitude larger than 4 MeV $^4He^+$ and $\sim$ 1000 times larger than 30 MeV Cl^+, a typical probe beam used in conventional ERD. However, at medium energies, sputtering of the surface is a greater concern. Sputter yields from silicon calculated using the empirical formula of Matsunami et al. [10] clearly indicate that the deposited charge should be minimized when the heavier probe ions are used.

The flight time of an atom in the detector can be calculated using

$$\Delta t = \sqrt{\frac{mL^2}{2\left(E - x\dfrac{\mathrm{d}E}{\mathrm{d}x}\right)}} - t_0, \qquad (1)$$

where m is the mass of the particle, L is the flight

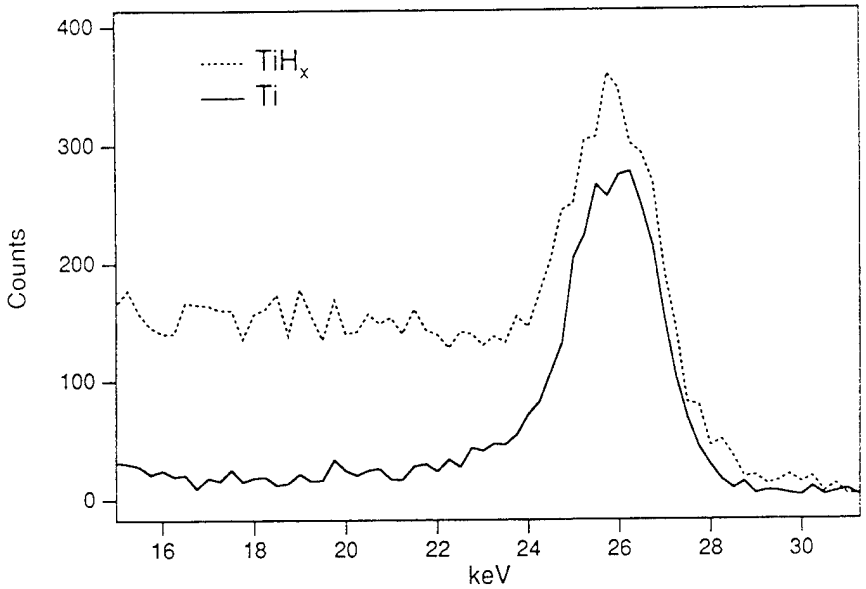

Fig. 3. Hydrogen recoil energy spectra for pure and hydrated titanium, for a deposited charge of 1.25×10^{12} ions.

path, x is the foil thickness, and dE/dx is the stopping power of the atom at an energy E in carbon. The electron flight time is contained in t_0. In general, the difference in flight times between recoil hydrogen and the scattered beam will increase with increasing probe mass, while the time difference between hydrogen and other recoils from the host material will decrease. This must be considered when trying to maximize the analyzable depth for hydrogen in a material. For our system, a Ne probe beam seems to be the best compro-

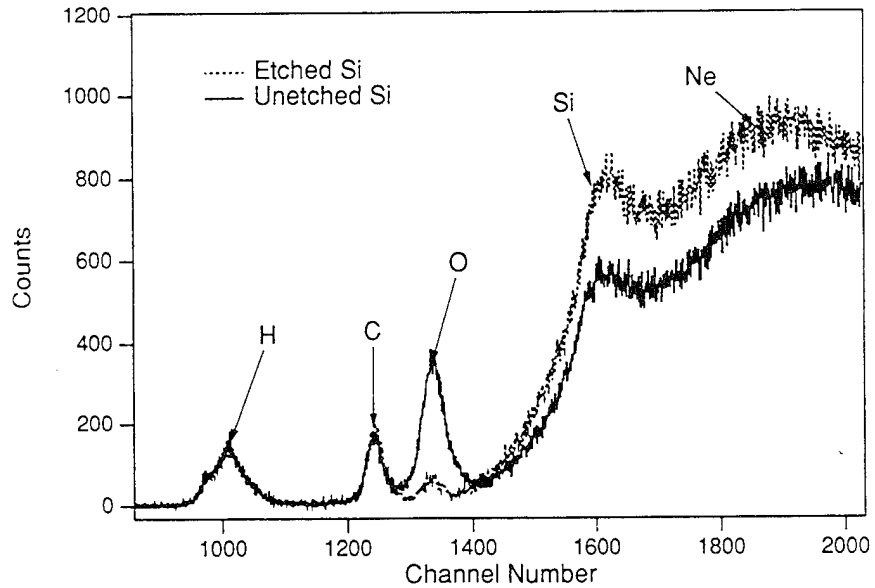

Fig. 4. TOF spectra for 270 keV Ar^+ on etched and unetched silicon; total charge of 1.25×10^{12} ions.

mise for the sensitive profiling of near surface hydrogen in materials.

Fig. 2a shows a time-of-flight spectrum for 270 keV Ne^+ on Kapton. The deposited charge was increased for this analysis to increase the visibility of the oxygen feature and improve the signal to background. Recoil carbon, oxygen and scattered neon are observed in addition to a substantial hydrogen feature. The hydrogen region is transformed from time into energy and displayed in fig. 2b. The atomic concentration of hydrogen near the surface may be calculated using relations derived from ref. [11]:

$$C_H = N_H \frac{\epsilon(E_0)\cos\theta_1}{\Delta E} \times 100\%, \quad (2)$$

where

$$N_H = \frac{Y}{\sigma_r Q \Omega \eta} \quad (3)$$

gives the concentration in atoms/cm^2. Y is the yield over the energy range ΔE. σ_r is the recoil cross section, Q is the number of incident ions, Ω is the solid angle, η is the detector efficiency, and

$$\epsilon(E_0) = \frac{1}{\cos\theta_1} K' S(E_0)_{Ne} + \frac{1}{\cos\theta_2} S(K'E_0)_H, \quad (4)$$

with K' the recoil kinematic factor and $S(E)$ the stopping cross section in eV/10^{15} atoms/cm^2. With $\theta_1 = \theta_2$, the angular dependence in eqs. (2) and (4) cancels. We estimate the hydrogen atomic concentration to be $31 \pm 5\%$, in reasonable agreement with a prediction of 26% based on stoicheometry. The analyzable depth for Kapton using neon is approximately 100 nm.

The recoil hydrogen energy spectra for pure and hydrated titanium are overlaid in fig 3. Both samples show a hydrogen enrichment at the surface probably due to hydrocarbon adsorption. The measured hydrogen coverage for the pure sample was 6×10^{15} cm^{-2} at the surface. Our measurements yield a result of $18 \pm 4\%$ for the bulk atomic hydrogen concentration in hydrated titanium. The estimate is complicated by the fact that the hydrogen concentration enters into the computation of the stopping cross section in eq. (4). Moreover, depletion of hydrogen near the surface of the hydrated sample was observed after only 6.25×10^{12} ions were deposited. However, this is still roughly 5 times the charge deposited during a typical analysis.

As noted in table 1, a 270 keV argon beam is capable of simultaneously resolving hydrogen, carbon, and oxygen surface contaminants on silicon. Fig. 4 shows the time of flight spectra for etched and unetched silicon using such a probe. As expected, reduction in the native oxide caused by the etch is very apparent while little variation was observed in the hydrogen and carbon features attributable to organic contaminants which are not affected by the treatment. Based on our experience in helium backscattering from silicon, the scattering yield from the substrate is stongly influenced by channeling and blocking. We therefore attribute the variation in size of the recoil Si and scattered Ar features to the random orientation of the samples. The thickness of the native oxide layer was determined to be 15 Å, based upon an estimate of the detector efficiency for oxygen of roughly 25% and a density of 2.5 g/cm^3 of SiO_2. After etching, only $\sim 1 \times 10^{15}$ cm^{-2} of oxygen were found to remain. A third silicon sample, etched in HF but not rinsed, had a detectable fluorine residue estimated to be $\sim 1 \times 10^{14}$ cm^{-2}.

The fluorine coverage of the etched Si sample probably approaches the limit of sensitivity to heavier contaminants currently possible with our apparatus. Because of the recoil cross section and detector response, we estimate the minimum detectable level of hydrogen to be lower. Let us define a minimally detectable feature as one whose integrated yield is three times the standard error. Then the analysis of the sample of pure titanium, with an integrated region of 80 channels for hydrogen and a background of 6 counts/channel nearby, would establish a minimum detectable coverage of 3×10^{13} H atoms/cm^2 near the surface. The lowest limit for hydrogen surface sensitivity we have found reported in the literature for conventional ERD is 1×10^{12} H atoms/cm^2 [12]. The result was based on the detection of a single recoil H atom. Using our sensitivity criteria this limit would be increased by at least an order of magnitude, and is comparable with our reported value.

4. Conclusion

We have demonstrated the feasibility of elastic recoil detection of light elements in materials using 270 keV ions of several species in conjunction with time-of-flight spectroscopy. The quantum efficiency for hydrogen detection of the present detector configuration is approximately 30% and is relatively independent of energy in the range studied. Using this efficiency, it has been possible to obtain reasonable agreement between the measured and theoretical concentration of hydrogen in Kapton. Extrapolating from the measurement of hydrogen in titanium, we estimate that the minimum detectable areal density of surface hydrogen is about 3×10^{13} cm^{-2} with the current experimental geometry. Experiments currently under way are designed to study the depth resolution of the technique including the degree to which surface and bulk hydrogen can be resolved.

Acknowledgements

This work was supported in part by the U.S. Army Research Office and by a grant from Texas Instruments, Inc.

References

[1] D.B. Fenner, D.K. Biegelsen and R.D. Bringans, J. Appl. Phys. 66 (1989) 419.
[2] R.J. Brewer, J.K. Gimzewski and S. Veprek, J. Nucl. Mater. 103 (1982) 465.
[3] W.A. Lanford, H.P. Trautvetter, J.F. Ziegler and J. Keller, Appl. Phys. Lett. 28 (1976) 566.
[4] B.L. Doyle and P.S. Peercy, Appl. Phys. Lett. 34 (1979) 811.
[5] J.P. Thomas, M. Fallavier and A. Ziani, Nucl. Instr. and Meth. B15 (1986) 443.
[6] M.H. Mendenhall and R.A. Weller, Nucl. Instr. and Meth. B47 (1990) 193.
[7] M.H. Mendenhall and R.A. Weller, Nucl. Instr. and Meth. B40/41 (1989) 1239.
[8] S.C. Gujrathi and S. Bultena, Nucl. Instr. and Meth. B64 (1992) 789.
[9] J.P. Biersack and L.G. Haggmark, Nucl. Instr. and Meth. 174 (1980) 257.
[10] N. Matsunami et al., Atom Data Nucl. Data Tables 31 (1984) 1.
[11] W.K. Chu, J.W. Mayer and M.A. Nicloet, Backscattering Spectrometry (Academic Press, New York, 1978) chaps. 3 and 4.
[12] H. Nagai, S. Hayashi, M. Aratani, T. Nozaki, M. Yanokura, I. Kohno, O. Kuboi and Y. Yatsurugi, Nucl. Instr. and Meth. B28 (1987) 59.

3. Surface characterization by medium energy scattering

SURFACE CHARACTERIZATION BY MEDIUM ENERGY PARTICLE SCATTERING

James H. Arps and Robert A. Weller

Vanderbilt University
Nashville, Tennessee 37235

INTRODUCTION

At the atomic scale, it is quite difficult to devise truly non-destructive measurement procedures because to do so requires a probe which gives specific quantitative, chemical or structural information without breaking chemical bonds. Ion beam analytical techniques using MeV beams are well known and versatile tools for characterizing surfaces and are generally considered to be nondestructive to most inorganic materials, although the electrical properties of the sample are usually altered. In this article, we discuss recently developed scattering techniques using time-of-flight particle detection that work well with ions whose energies are at least an order of magnitude lower than those required for conventional analyses. This reduction in the ion beam energy makes possible novel measurements such as the characterization of thin films on polymer substrates as well as enhanced capabilities such as improved depth resolution and increased sensitivity for trace element detection.

Surfaces are of immense importance in modern materials science. They are both areas where processes such as wear and corrosion are concentrated and sites for the fabrication of unique structures such as semiconductor devices. Moreover, they are the regions of transition between layers of bulk materials and between bulk materials and the surrounding environment and, therefore, often have unique electrical and chemical properties.

When characterizing a surface, one seeks to learn the electrical, chemical and geometrical structure usually of both the first atomic layer, which is the true surface, and the near surface region or exostrate which may, according to the problem of interest, be from a single atomic layer up to perhaps a few tens of nanometers thick. A truly impressive array of tools has been developed over the years for surface characterization[1]. For example, one learns about surface electrical structure from ultra-violet photoelectron spectroscopy while surface atomic arrangement is found by low-energy electron diffraction. Elemental composition may be found from Auger electron spectroscopy while the chemical

Nondestructive Characterization of Materials VI
Edited by R.E. Green, Jr. *et al.*, Plenum Press, New York, 1994

environment of the various atoms is accessible from x-ray photoelectron spectroscopy.

It is universally understood among practitioners of surface analysis that no single technique is right for all problems and that almost always a battery of measurements from complementary techniques is required to understand a problem in surface physics. However, one technique, Rutherford Backscattering Spectrometry (RBS) has been found to be particularly useful when one seeks to understand quantitatively the elemental composition of thin films as a function of depth.

The principles that underlie RBS are quite simple. An ion beam, e.g. He^+, of perhaps 2 MeV is directed onto the surface under study and the number of scattered projectiles at a specific angle is measured as a function of energy. Since the scattering cross section can be computed and the rate at which the ions lose energy as they penetrate the sample (stopping power) is known from measurements, the energy spectrum of backscattered particles is a representation of the depth distributions of the various constituents of the surface.

The disadvantages of RBS are that it does not work well with layers of low-atomic-weight materials on substrates of heavier elements (because backscatters from the light surface atoms have the same energies as scatters from the heavier and much more numerous atoms found more deeply in the target), that it requires a relatively large and costly accelerator, and that it has limits of depth resolution and sensitivity both of which are traceable to the properties of and constraints imposed by the silicon surface-barrier detectors that are almost universally used to measure the number and energy of the backscattered ions. The limitation on analyzing low-atomic-mass layers is fundamental to backscattering and may only be addressed by other techniques or, as we shall discuss below, by another scattering geometry. In all the other areas mentioned, improvements can in principle be realized by the use of lower energy primary ions, provided that the region of the sample which is of interest is sufficiently near the surface.

The purpose of this article is to describe a new detection technology for low and medium energy ions with which the potential gains from using lower energy primary ions may be realized. The new procedure involves replacing the solid-state, surface-barrier detector ordinarily used for RBS by a time-of-flight spectrometer. The following sections give an overview of the spectrometer operation and performance, and illustrate its advantages over conventional techniques in both backscattering and forward recoil geometry.

TIME-OF-FLIGHT SPECTROMETRY

Although time-of-flight spectrometry has been used extensively in the past for ion beam and nuclear studies[2], its application to medium energy scattering problems is relatively recent[3]. Figure 1 shows a time-of-flight spectrometer in a backscattering configuration. The primary ion beam enters from the right and strikes a target which is usually normal to the beam during backscattering analysis. Backscattered particles (with a distribution of charge states) enter the time-of-flight spectrometer and pass through a 2-3 $\mu g/cm^2$ carbon foil mounted on a high transmission mesh between two similar grounded meshes. The foil bias is typically -400 V. Secondary electrons emitted from the foil as the particle exits are accelerated by the bias toward a microchannel plate operated with its sensitive cathode at ground potential.

When the electrons arrive at the microchannel plate, a start pulse is generated. The ions, meanwhile, continue toward the stop detector with somewhat decreased energy and trajectories that have been perturbed by multiple scattering in the foil. When a stop pulse is generated within the coincidence resolving time of the external electronics, an event is recorded. Since the ion flight path length is known, the interval between start and stop pulses is a direct measure of particle velocity. In a backscattering experiment, this is equivalent to knowing the energy since the particle's mass is known. It is important to note that the charge state of the particle entering the spectrometer is not a crucial variable in the measurement because secondary electron emission from the carbon foil is at most very weakly dependent upon it. Thus, in this technique charge exchange at the target surface is not an important factor complicating the interpretation of measurements as it is in some other low energy ion beam analytical procedures.

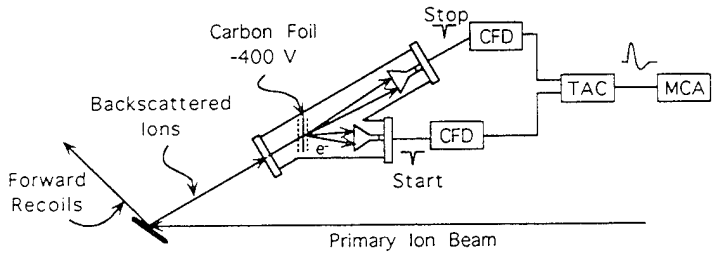

Figure 1. Schematic of the forward and backscattering experimental arrangements including a diagram of the time-of-flight spectrometer and a schematic of the external electronics. The forward recoil spectrometer is identical to the one shown and so is omitted from the figure. Abbreviations used are, constant-fraction discriminator (CFD), time-to-amplitude converter (TAC) and multichannel analyzer (MCA). Note that preamplifiers are no longer used to amplify the the timing signals.

The detector configuration shown in figure 1 is typically used for particles with energies from about 10 keV up to several hundred keV. However, it has been shown experimentally to respond to ions ranging from 5 keV protons to argon ions approaching 1 MeV as well as to 5 MeV α particles from a radioactive source. With a drift length of about 37 cm, typical flight times are from less than 100 ns to several hundred ns. The detector timing resolution is most appropriately measured with a fast particle such as an α from a radioactive source, but has been shown recently with protons from our accelerator to be well under 1 ns, a value at which it does not significantly detract from the quality of measurements. With the recent introduction of a biasing scheme for the start microchannel plate based upon microwave technology, it is now likely that the factors limiting overall spectrometer resolution are the path length uncertainty arising from our use of a start foil which is not perpendicular to the spectrometer

axis, and the uncertainty in ion energy in the drift region between the foil and the stop detector attributable to charge exchange in the carbon foil[4]. The latter is approximately two times the bias, or 800 eV for most particles.

Along with resolution, the other key parameter affecting the performance of a time-of-flight spectrometer is quantum efficiency, or the probability that an ion entering the detector actually generates an event. For the surface-barrier detector, the efficiency is usually assumed with reasonable accuracy to be unity for particles of all energies. This is extremely convenient since, in this case, a simple measure of detector geometric solid angle is sufficient to relate measured counts to the areal concentrations of the various surface constituents (where, of course, the scattering cross section and quantity of beam are assumed to be know). Unfortunately, for the time-of-flight spectrometer the efficiency is considerably more complicated.

The physical processes affecting the efficiency of the time-of-flight spectrometer are secondary electron emission from the carbon foil, multiple scattering of the ions passing through the carbon foil, the responses of the microchannel plates to electrons and ions, and some geometrical factors. A detailed discussion of the ways in which these processes contribute quantitatively to the spectrometer efficiency is beyond the scope of this article but will be treated in detail in a forthcoming paper now in preparation by our group. It is sufficient for our present review to observe that by taking what is known individually about each of these physical processes and combining this knowledge in a mathematical model of the spectrometer, one can obtain reasonable agreement between theory and the measured efficiency as a function of particle species and energy. Thus, uncertainty about the spectrometer quantum efficiency should not pose a significant impediment to routine use of time-of-flight detectors for quantitative work.

A final issue concerning the practicality of time-of-flight spectrometry is the rate of data acquisition. Here, the time-of-flight spectrometer and the surface barrier detector are approximately comparable and offer significantly higher throughput than pulsed beam time-of-flight systems or electrostatic or magnetic spectrometers which are charge-state sensitive and can only analyze one energy at a time. At higher count rates both time-of-flight and surface-barrier detector spectra develop artifacts, the former from random coincidences in the spectrometer and the latter by a process called pulse pile-up. A complete theory of the effects of count rate on time-of-flight spectra has been published recently[5]. Its most important conclusion is that the random background is independent of flight time and proportional to count rate. Thus, background can be lowered by decreasing beam current, measured by examining regions of a spectrum kinematically forbidden to have real events, and removed by a simple background subtraction. By contrast, pile-up is a convolution and it is, therefore, much more difficult to extract true signal in its presence.

BACKSCATTERING MEASUREMENTS

The objective of backscattering measurements is to determine the composition and structure of thin films. The advantages of time-of-flight medium energy backscattering (MEBS) when compared with conventional RBS are 1) less total energy deposited in the sample, 2) greater sensitivity per primary ion (because of the larger cross section at lower energies), and 3) improved depth resolution (because of the higher resolution of the time-of-flight spectrometer

when compared with surface barrier detectors). In this section, we illustrate the first and last of these with specific experimental examples.

Improved sensitivity to trace elements and, in particular, to surface contaminants is probably the most important consequence of the larger cross section at medium energies. This is particularly important in the semiconductor industry where minute traces of elements such as iron or copper on silicon wafers can render devices unusable[6]. As of this writing, total reflection x-ray fluorescence spectrometry is the method of choice for the analysis of such contamination[7]. However, estimates based upon plausible assumptions and supported by preliminary experimental results suggest that medium energy backscattering spectrometry may be an effective alternative technique[5,8]. This conjecture is the subject of active investigation in our laboratory and elsewhere.

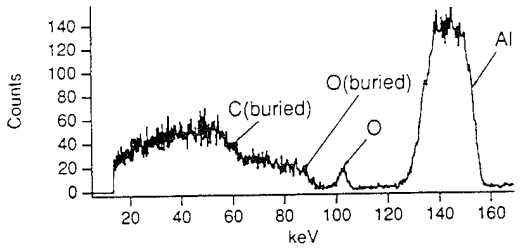

Figure 2. Backscattering spectrum of a metallized plastic. Analysis of the data revealed that the metallic film was Al about 10 nm thick. Note also the small oxygen peak attributable to the surface oxide. The plastic substrate was virtually unaffected by the analysis.

The energy deposition which accompanies conventional backscattering is sufficiently large that it is extremely difficult to analyze films on polymer substrates. Typically, the organic substrate is at least discolored by the radiation damage produced by the beam and, more often, is destroyed completely. Figure 2 shows a medium energy backscattering spectrum, mathematically rendered as an energy spectrum for the convenience of readers familiar with RBS. This spectrum was made by backscattering 270 keV He^+ ions from a metallized plastic of unknown composition. The purpose of the experiment was to determine the composition and thickness of the metallic layer. The signature of this layer is the isolated peak which, from its placement in energy and its thickness, unambiguously indicates that the metal is aluminum and that the layer is about 10 nm thick. Inspection of the area exposed to the beam after removing the sample from the vacuum chamber revealed a very slight discoloration but no structural damage to the underlying organic material. In fact, direct exposure of the substrate during a backscattering run to determine its composition also produced barely visible damage.

The extraordinary depth resolution of MEBS is illustrated by figure 3 which is a composite of four backscattering spectra made by 270 keV He^+ ions incident upon TiN films of increasing thickness deposited on oxidized silicon wafers. The isolated mesa-like feature in these spectra results from He^+ scattering from Ti in the surface layer. From the width of the features we conclude that the layers range from about 41 nm to about 47 nm thick. Thus, the differences indicated by the varying widths of the peaks are only of order 2 nm and are clearly visible by inspection. Experience suggests that under favorable conditions the positions of these edges may be determined with an error of less than 100 eV. This approaches single atomic layer thickness discrimination and suggests that MEBS may be a very effective tool in corrosion studies such as described by Hübler *et al.*[9] The shifting of edge positions has also been used to quantify minute changes in the thickness of an optical coating flown aboard NASA's long-duration exposure (LDEF) satellite which apparently resulted from the uptake of atomic oxygen[10]. In that case, a shift of 1 keV was observed to be ten standard deviations larger than the experimental error.

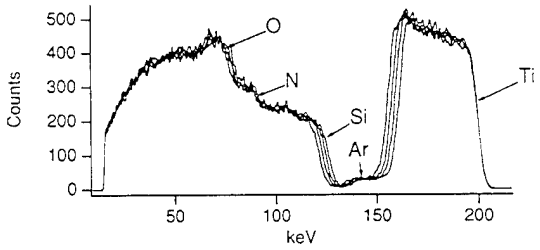

Figure 3. Backscattering spectra of four TiN thin films on SiO_2. Film thicknesses range from 41 nm to 47 nm in approximately 2 nm increments.

FORWARD SCATTERING MEASUREMENTS

One of the most active areas of research in our laboratory is the application of time-of-flight spectrometry to the analysis of forward recoils in a medium energy version of what is known at higher energies as elastic recoil detection or ERD[11]. This experimental configuration is shown in figure 1 by the arrow indicating the trajectory of forward recoils. Not shown in the figure is another time-of-flight spectrometer which, in our chamber, is at an angle of 42° with respect to the beam direction. At forward angles, both scattered beam ions and recoiling target constituents can enter the detector. This is precisely what is needed to identify low atomic mass constituents on the surface of a heavier substrate. By using a relatively heavy beam such as carbon, neon, or even argon, surface atoms are ejected in the direction of the forward detector with velocities up to nearly twice that of the incident ion. Since the time-of-flight

spectrometer ultimately differentiates velocities, the light elements arrive at the detector and are analyzed with no background from scattered beam ions in a significantly wide region of the spectrum. Thus, oxygen may be easily seen on the surfaces of Al, Si and heavier materials. Perhaps even more important, though, is the ability of this technique to measure hydrogen.

Hydrogen is a ubiquitous, critical, surface contaminant which also is one of the most difficult elements to measure[12]. High energy elastic recoil detection using MeV beams, especially when used in conjunction with time-of-flight detection, has been quite effective[13]. However, as with conventional RBS, the equipment is large and expensive and the beam is very damaging to many materials. Typical results obtainable with medium energy elastic recoil detection are shown in figure 4.

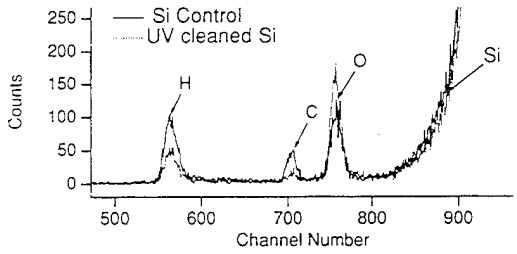

Figure 4. Forward recoil spectrum of a Si wafer before and after UV/ozone cleaning. The incident beam was 810 keV Ar^{3+}.

Figure 4 shows forward recoil spectra made by 810 keV Ar^{3+} bombardment of a Si wafer before and after cleaning by exposure to UV radiation in air[14]. This spectrum is left in its original time-of-flight form since, with several species present that have different masses, the transformation from a velocity to an energy representation is not appropriate. The effects on the quantities of H, C, and O are obvious by inspection. Clearly, if the removal of surface hydrocarbon contamination is the goal, the cleaning process succeeds. However, it does so at the expense of increased oxide thickness. The quantity of hydrogen remaining on the UV irradiated surface after the cleaning is estimated from the number of counts in the peak to be 5×10^{14} cm^{-2} while the number of C atoms is similarly 3×10^{14} cm^{-2}. From these and other data we estimate the current sensitivity for hydrogen detection (defined to be a signal three standard deviations above background) to be about 3×10^{13} H/cm^2.

The ability of medium energy elastic recoil analysis to give information about the depth distribution of hydrogen is illustrated by figure 5. This forward recoil spectrum, again made with 810 keV Ar^{3+}, represents a Si wafer onto which has been floated a carbon foil containing about 10^{17} C atoms/cm^2 and a small atomic percentage of hydrogen. Note the structure in the hydrogen feature.

Clearly the amount of hydrogen is largest near the surface of the foil and at the interface between the carbon and the silicon. It is likely that the latter is from water trapped at the interface during the operation of floating the foil. These data indicate that the depth resolution near the surface is less than 5 nm, although it is important to note that this resolution degrades rapidly as a function of depth when heavy primary ions such as Ar^{3+} are used.

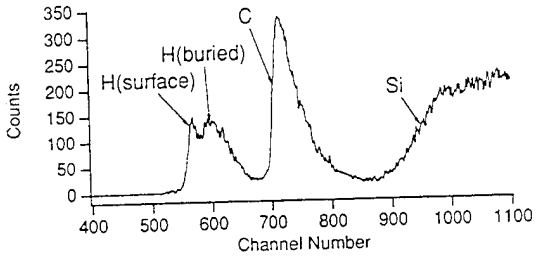

Figure 5. Forward recoil spectrum of a hydrogen-containing C layer on the surface of Si. The carbon layer is about 10^{17} atoms/cm^2 thick. Note the structure of the hydrogen feature. The spectrum reveals that there is both an excess of surface hydrogen relative to the bulk and a concentration of hydrogen at the Si-C interface.

CONCLUSION

Medium energy ion beam analysis using time-of-flight spectrometry is an important new tool for the analysis of surfaces which is particularly well suited to studies of the exostrate up to a depth of perhaps 100 nm. In backscattering mode, the depth resolution exceeds that which can be obtained by higher energy ion beam techniques by a considerable margin, and there is reason to believe that with further development medium energy backscattering may equal or exceed TXRF for the detection and measurement of trace levels of contamination on Si wafers. In forward scattering mode, existing data indicate a sensitivity and depth resolution for H measurement comparable with the best obtainable by other techniques. These are obtained with equipment whose size, in principle, should resemble more that of an electron microscope than that of the traditional electrostatic particle accelerator.

While still in a process of evolution, medium energy time-of-flight techniques offer unique capabilities for the study of thin films, for the detection of trace elements and for applications as diverse as semiconductor device characterization and gaseous corrosion studies. It may even be possible under favorable conditions to obtain information about biological membranes. Requiring smaller and less costly equipment, medium energy techniques will, in the future, make ion beam analysis available to a larger community than ever before.

ACKNOWLEDGMENTS

The authors wish to thank Martha R. Weller for creating an electronic form of figure 1 and Alain Diebold of Sematech for providing us with the high quality TiN films which were the subject of figure 3. This work was supported in part by the U.S. Army Research Office under contract DAAL 03-92-G-0037.

REFERENCES

1. Leonard C. Feldman and James W. Mayer, "Fundamentals of Surface and Thin Film Analysis", North Holland, Amsterdam (1986).
2. Harry J. Whitlow, Time of flight spectroscopy methods for analysis of materials with heavy ions: a tutorial, *in*: "High Energy and Heavy Ion Beams in Materials Analysis," J. R. Tesmer, C. J. Maggiore, M. Nastasi, J. C. Barbour and J. W. Mayer, eds., Materials Research Society, Pittsburgh (1990).
3. Marcus H. Mendenhall and Robert A. Weller, High resolution medium energy backscattering spectrometry *Nucl. Instr. and Meth.* B59/60:120 (1991).
4. Marcus H. Mendenhall and Robert A. Weller, Performance of a time-of-flight spectrometer for thin film analysis by medium energy ion scattering, *Nucl. Instr. and Meth.* B47:193 (1990).
5. Robert A. Weller, Instrumental effects in time-of-flight spectra, *Nucl. Instr. and Meth.* B, in press, (1993).
6. D. C. Jacobson, J. M. Poate, G. S. Higashi and T. Boone, Implanted standards for detection of transition metal contamination of silicon surfaces, *Nucl. Instr. and Meth.* B74:281 (1993).
7. U. Weisbrod, R. Gutschke, J. Knoth, and H. Schwenke, Total reflection x-ray fluorescence spectrometry for quantitative surface layer analysis, *Appl. Phys.* A53:449 (1991).
8. J. A. Knapp and B. L. Doyle, Heavy-ion backscattering spectrometry (HIBS) for high-sensitivity surface impurity detection, *Nucl. Instr. and Meth.* B45:143 (1990).
9. R. Hübler, A. Schröer, W. Ensinger, G. Wolf, F. C. Stedile, W. H. Schreiner and I. J. R. Baumvol, Corrosion behavior of steel coated with thin film TiN/Ti composites, *J. Vac. Sci. Technol.* A11(2):451 (1993).
10. Marcus H. Mendenhall, Robert A. Weller, and Ann F. Whitaker, Evolution of optical coatings in Earth orbit, *Optics Letters* 16:1466 (1991) .
11. James H. Arps and Robert A. Weller, Medium energy elastic recoil analysis of surface hydrogen, *Nucl. Instr. and Meth.* B in press (1993).
12. "The Analysis of Hydrogen in Solids", Proceedings of a Workshop Summarizing Developing Techniques and Formulating Requirements for the Future," Sandia National Laboratories, Albuquerque, NM, January 23-25, 1979, United States Department of Energy DOE/ER-0026, April 1979.
13. J. P. Thomas, M. Fallavier and A. Ziani, Light elements depth-profiling using time-of-flight and energy detection of recoils, *Nucl. Instr. and Meth.* B15:443 (1986), and references therein.
14. John R. Vig, UV/ozone cleaning of surfaces, *in:* "Treatise on Clean Surface Technology, Volume 1," K. L. Mittal, ed., Plenum, New York (1987).

4. An algorithm for computation of multiple scattering

Nuclear Instruments and Methods in Physics Research B 93 (1994) 5–10
North-Holland

NIM B
Beam Interactions with Materials & Atoms

An algorithm for ab initio computation of small-angle multiple scattering angular distributions

Marcus H. Mendenhall and Robert A. Weller *
Vanderbilt University, Nashville, TN 37235, USA

Received 7 January 1994 and in revised form 8 March 1994

Small-angle multiple scattering is a venerable problem in nuclear and particle–solid interaction physics and has received extensive theoretical treatment. In this paper, motivated by the need to establish the efficiency of time-of-flight spectrometers which employ thin foils to generate "start" signals, we revisit this problem. Our objective is to develop an efficient, general computational procedure which is not tied to the current state of computing machinery or specific cross sections, but which takes advantage of significant numerical-algorithmic advances which have occurred since the multiple-scattering problem was originally formulated. By introducing a new approach for dealing with the azimuthal symmetry of the problem, we avoid Hankel transforms which have been used in all previous treatments and, in so doing, make it possible to apply the fast Fourier transform algorithm in one dimension. The resulting computation can be carried out to arbitrary accuracy with sufficiently dense sampling of the cross section and is very fast when compared with numerically computed Hankel transforms. Angular distributions for several scattering potentials and a compound target are compared.

1. Introduction

To apply time-of-flight spectrometry to surface analysis using a continuous beam accelerator, you must devise a scheme to determine when a individual scattered ion or neutral particle enters and leaves a drift region with a known length [1]. It is easy to establish when a particle completes the course, since it may be intercepted by any one of a number of styles of particle detectors. However, establishing the time that the particle enters the measured course is another matter, since this determination must be made with minimal perturbation of the particle's speed and trajectory. The most widely adopted scheme has been to place a thin, self-supporting carbon foil in the particle's path and to detect bursts of secondary electrons that accompany its passage through the foil. The disadvantage of this technique is that small-angle multiple scattering in the carbon foil can alter the trajectory of the ion sufficiently that it misses the second detector at the end of the drift space and so does not produce a measurable event. Thus, multiple scattering is one of the physical processes which, along with secondary electron emission and the intrinsic responses of the detectors which comprise the spectrometer, determines the overall spectrometer efficiency [2].

* Corresponding author, tel. +1 615 343 6027, fax +1 615 343 7263, e-mail weller@vuse.vanderbilt.edu.

The general procedure for computing small angle multiple scattering was developed several decades ago, has been reviewed thoroughly [3], and revisited by several authors subsequently as computing technology and the quality of scattering cross sections has advanced [4–6]. Moreover, the results of multiple-scattering computations continue to be of interest for practical experimental work [7], additional theoretical development [8], and continuing experimental verification [9]. We will confine our attention to the simplification of the general problem in which angles can be assumed to be small in the sense that $\sin(\theta) \approx \theta$. Also, we adopt the assumptions, including the neglect of energy loss, binary collisions and a random scattering medium, which have been summarized by Sigmund and Winterbon [6]. In this approximation, the angular distribution of particles as a function of depth of penetration into the solid is described by a transport equation which involves a convolution. This equation is solved, in turn, by integral transforms using the convolution theorem. The desired distribution is recovered by inversion of the integral transform. The cylindrical symmetry of the problem at once suggests the use of Hankel transforms [10] and, so far as our research reveals, this has been the approach which has been used universally in the literature. The results are theoretically appealing, concise and are nicely connected with the large-angle version of the problem through mathematical relationships between special functions [11]. However, Hankel transforms are cumbersome to compute numerically.

SSDI 0168-583X(94)00173-S

This is not the case for Fourier transforms. With the widespread dissemination of the fast Fourier transform (FFT) algorithm in the mid 1960s, it became possible to compute the transform of very large arrays of numbers, even in multiple dimensions, in an acceptable amount of time [12]. Contemporary with this development, and also important for the present application, were the introduction of adaptive quadratures (such as ref. [13]) which, by intelligent selection of sample points, were able to generate high quality numerical integrals very efficiently.

It is possible to attack the multiple scattering problem by brute force using a two-dimensional FFT. However, by using the axial symmetry about the beam direction, the problem can be reduced to a one-dimensional FFT of a set of points each one of which is obtained by numerical integration of a very smooth function. This is the approach taken in this paper. We begin with a brief restatement of the theory which is applicable to our problem, emphasizing the novel approach which we have taken to reduce the dimensionality from two to one. A subsequent section deals with the numerical details of the computation. Finally, we present some sample calculations for the cases of the Rutherford, the Lenz–Jensen [14], and the Ziegler–Biersack–Littmark "universal" [15] scattering cross sections. The algorithms which are presented here are sufficiently simple and general that they can be easily adapted to other cross sections as well as to routine multiple scattering computations in support of experiment and theory.

2. Theory

The quantity of interest in the discussion which follows is $f(z, \theta_x, \theta_y)$, the probability that a particle which enters a foil along the z axis will be scattered into an element of solid angle described by θ_x and θ_y after penetrating a distance z into the foil. It is possible to describe the direction of the scattered particle by orthogonal displacements (θ_x, θ_y) in a plane because of the small angle approximation. The change in f which is attributed to penetrating from z to $z + \mathrm{d}z$ is the sum of the probability that the particle is scattered into the specific solid angle from another direction, less the probability that a particle is already traveling in the appropriate direction and is scattered to any other direction. The total cross section for scattering is denoted by σ_{tot} while the number density of scattering centers is N.

$$f(z + \mathrm{d}z, \theta_x, \theta_y) = f(z, \theta_x, \theta_y) + N\,\mathrm{d}z \int \sigma(\Theta) f(z, \eta_x, \eta_y)\,\mathrm{d}\eta_x\,\mathrm{d}\eta_y - N\sigma_{\mathrm{tot}} f(z, \theta_x, \theta_y)\,\mathrm{d}z, \quad (1)$$

where $\Theta = [(\theta_x - \eta_x)^2 + (\theta_y - \eta_y)^2]^{1/2}$ and $\sigma(\Theta)$ is the laboratory-frame, differential scattering cross section. The Fourier transform of this equation with respect to θ_x and θ_y is:

$$\tilde{f}(z + \mathrm{d}z, \omega_x, \omega_y) = \tilde{f}(z, \omega_x, \omega_y) + N\,\mathrm{d}z\tilde{\sigma}(\omega_x, \omega_y)\tilde{f}(z, \omega_x, \omega_y) - N\sigma_{\mathrm{tot}}\tilde{f}(z, \omega_x, \omega_y)\,\mathrm{d}z, \quad (2)$$

where:

$$\tilde{\sigma}(\omega_x, \omega_y) = \int\int \sigma(\theta_x, \theta_y)\, \mathrm{e}^{-\mathrm{i}(\omega_x\theta_x + \omega_y\theta_y)}\,\mathrm{d}\theta_x\,\mathrm{d}\theta_y, \quad (3)$$

and similarly for $\tilde{f}(z, \omega_x, \omega_y)$, and where we have invoked the convolution theorem to express the transform of the term representing atoms scattered into the solid angle of interest as the product of the $\tilde{f}$ and of $\tilde{\sigma}$. In the limit of small $\mathrm{d}z$, this becomes a differential equation for the Fourier transform $\tilde{f}$

$$\frac{\partial \tilde{f}(z, \omega_x, \omega_y)}{\partial z} = N\big(\tilde{\sigma}(\omega_x, \omega_y)\tilde{f}(z, \omega_x, \omega_y) - \sigma_{\mathrm{tot}}\tilde{f}(z, \omega_x, \omega_y)\big). \quad (4)$$

This is an elementary equation with solution:

$$\tilde{f}(z, \omega_x, \omega_y) = \exp\big[N \cdot z\big(\tilde{\sigma}(\omega_x, \omega_y) - \sigma_{\mathrm{tot}}\big)\big], \quad (5)$$

where we assume that $f(0, \theta_x, \theta_y) = \delta(\theta_x)\delta(\theta_y)$ is a two-dimensional Dirac delta function whose transform is, of course, unity throughout the reciprocal space. The angular distribution is obtained from Eq. (5) by the inverse transform:

$$f(z, \theta_x, \theta_y) = \frac{1}{(2\pi)^2}\iint \tilde{f}(z, \omega_x, \omega_y) e^{\mathrm{i}(\omega_x\theta_x + \omega_y\theta_y)}\,\mathrm{d}\omega_x\,\mathrm{d}\omega_y. \quad (6)$$

Since the cross section σ is cylindrically symmetrical, previous authors have reduced the two-dimensional Fourier transforms given in Eqs. (3) and (6) to one-dimensional Hankel transforms involving the Bessel function J_0. It is at this point that our treatment of the problem diverges from previous ones. If a function is cylindrically symmetrical in space, then its Fourier transform is cylindrically symmetrical in reciprocal space. Note that for a cylindrically symmetric function, where $g(x, y) = g((x^2 + y^2)^{1/2})$, $g(x, 0)$ completely characterizes the function. Similarly, $\tilde{\sigma}(\omega_x, \omega_y)$ is completely determined by $\tilde{\sigma}(\omega_x, 0)$ and $f(z, \theta_x, \theta_y)$ by $f(z, \theta_x, 0)$. From the definition of the Fourier transform

$$\tilde{\sigma}(\omega_x, \omega_y) = \iint \sigma(\Theta) e^{-\mathrm{i}(\omega_x\theta_x + \omega_y\theta_y)}\,\mathrm{d}\theta_x\,\mathrm{d}\theta_y, \quad (7)$$

we see that for $\omega_y = 0$,

$$\tilde{\sigma}(\omega_x, 0) = \iint \sigma(\Theta)\, e^{-i\omega_x\theta_x}\, d\theta_x\, d\theta_y = \int \left(\int \sigma(\Theta)\, d\theta_y \right) e^{-i\omega_x\theta_x}\, d\theta_x. \quad (8)$$

Since $\sigma(\Theta) = \sigma(\sqrt{\theta_x^2 + \theta_y^2})$, one can define a new function

$$s(\theta) = \int \sigma\left(\sqrt{\theta^2 + \eta^2}\right) d\eta \quad (9)$$

such that $\tilde{\sigma}(\omega_x, 0) \equiv \tilde{s}(\omega)$ is computed by a one-dimensional Fourier transform of $s(\theta)$. In the same way, returning to Eq. (5), we can then write for the angular distribution:

$$\tilde{f}(z, \omega_x, \omega_y) \equiv \tilde{g}\left(z, \sqrt{\omega_x^2 + \omega_y^2}\right) \equiv \tilde{g}(z, \omega) = \exp\left(N \cdot z\left(\tilde{s}(\omega) - \sigma_{tot}\right)\right). \quad (10)$$

Now, in analogy to Eq. (9), this function can be integrated to allow inversion with a one-dimensional transform. Define $\tilde{\gamma}$ to be the integral:

$$\tilde{\gamma}(z, \omega) \equiv \int \tilde{g}\left(z, \sqrt{\omega^2 + \eta^2}\right) d\eta. \quad (11)$$

The angular distribution of scattered particles follows immediately as the inverse Fourier transform of $\tilde{\gamma}$:

$$f(z, \theta) = \frac{1}{(2\pi)^2} \int \tilde{\gamma}(z, \omega)\, e^{i\theta\cdot\omega}\, d\omega. \quad (12)$$

Alternatively, it may be desirable in some circumstances to simply generate a rectangular array in reciprocal space using:

$$\tilde{f}(z, \omega_x, \omega_y) = \exp\left[N \cdot z\left(\tilde{s}\left(\sqrt{\omega_x^2 + \omega_y^2} \right) - \sigma_{tot} \right) \right] \quad (13)$$

and do a two-dimensional FFT, thus saving the effort expended on the quadratures. The complete solution for $f(z, \theta)$ consists of computing in order $s(\theta)$, $\tilde{s}(\omega)$, $\tilde{g}(z, \omega)$, $\tilde{\gamma}(z, \omega)$, and finally $f(z, \theta)$, or, instead, applying the two-dimensional inverse FFT to Eq. (13). Note that for varying film thicknesses, the form factor $\tilde{s}(\omega)$ does not need to be re-computed.

An important point which needs to be considered in the above calculation concerns the existence of σ_{tot}, the total scattering cross section. Classically, a potential which extends to infinity, such as those usually used in ion scattering computations, implies a total cross section σ_{tot} which is also infinite. Consequently, the above equations must be interpreted carefully. Of course, one way to deal with the apparent difficulty would be to simply truncate the interaction at some radius beyond which it is non-physical anyway. It turns out, however, that the divergence is not important, as we shall now demonstrate in two different ways, by examining first the analytical transforms and then the sampled transforms.

Consider the quantity $\sigma_{tot} - \tilde{\sigma}(\omega_x, \omega_y)$. Since σ_{tot} only occurs in this form, it is sufficient to show that this difference is always finite. For simplicity we shall denote the latter term using vector notation as $\tilde{\sigma}(\omega)$. Then we can write:

$$\sigma_{tot} - \tilde{\sigma}(\omega) = \int \sigma(|\theta|) \cdot (1 - \exp(-i \cdot \omega \cdot \theta))\, d^2\theta. \quad (14)$$

The total cross section diverges because $\sigma(|\theta|)$ diverges at the origin. However, near $|\theta| \equiv \theta = 0$, the complete integrand of Eq. (14) varies as $\frac{1}{2}\pi\omega^2\sigma(\theta)\cdot\theta^3$. Thus, the Rutherford cross section, which diverges as θ^{-4} for small θ, does, indeed, lead to a logarithmically divergent value for $\sigma_{tot} - \tilde{\sigma}(\omega)$. However, screened potentials which are used for ion–solid computations are much softer and yield cross sections correspondingly less singular. Since a singularity in σ of order less than 4 is integrable, the quantity $\sigma_{tot} - \tilde{\sigma}(\omega)$ is finite for all practical cross sections. Now let us examine the case in which we are using a discretely sampled function, which changes the nature of the problem at the origin.

Consider the function $s(\theta)$ from Eq. (9) which is to be sampled to compute the form factor, $\tilde{s}(\omega)$. For most potentials, $s(0)$ will be infinite. However, instead of using $s(0)$, one can substitute an adjusted value using, for example, $s(\Delta\theta/2)$, where $\Delta\theta$ is the sampling grid size in θ. This amounts to adjusting the single sampled point at the origin by an unknown amount. However, if the sampled function is adjusted at only one point, it amounts to creating a new function $s'(\theta) = s(\theta) + a\delta(\theta)$ where $\delta(\theta)$ is the Kronecker δ function and a is a (probably infinite) constant. Since the Fourier transform is linear, and the transform of $a\ \delta(\theta)$ is just a, this adds a to all components of $\tilde{s}(\omega)$. However, if σ_{tot} is computed by summing over the sampled values of $s(\theta)$, this also adds a to σ_{tot}, so when Eq. (10) is evaluated, a cancels out exactly. Thus, any reasonable choice for $s(0)$ makes no difference to the calculation and either setting it to 0 or to the value suggested above will provide the correct answer.

The steps outlined above can be followed relatively directly in order to generate the desired angular distributions as a function of foil thickness or of the dimensionless parameter $\tau \equiv N \cdot z$. In the following section we give the details of our implementation.

3. Computation

The computation of distributions as outlined above can be implemented very easily by taking advantage of

the extremely smooth nature of the functions involved and of the efficiency with which functions can be evaluated from interpolation tables. First, if $\sigma(\theta)$ requires significant time to compute (which it typically does), it is convenient to tabulate $\log(\sigma(e^t))$ at uniformly spaced values of t corresponding to angles ranging from the kinematically allowed maximum angle down to some very small angle, typically 10^{-7} rad. If σ has any tendency towards power law behavior, this tabulated function is extremely smooth, and only about 100 points need to be computed to provide cubic interpolation errors below 10^{-4} in the cross section at all angles.

Now, since $\sigma(\theta)$ is singular as $\theta \to 0$ and the integral in Eq. (9) has the particular form that it does, the computation of $s(\theta)$ can be greatly simplified by the change of variable $\eta = \theta \tan(\zeta)$. The result is that Eq. (9) becomes:

$$s(\theta) = 2\theta \int_0^{\zeta_{\max}} \frac{\sigma\left[\dfrac{\theta}{\cos(\zeta)}\right] d\zeta}{\cos^2(\zeta)}, \tag{15}$$

where $\zeta_{\max} = \arccos(\theta/\theta_{\max})$ and $\theta_{\max}$ is the maximum value for which the cross section σ is kinematically defined. This transforms the nearly improper integral in which most of the value comes from a very tiny region near the origin into one in which the integration algorithm samples the function primarily where it is large and avoids expending a lot of computing effort integrating the very tiny tails of the integrand near the kinematic limit of θ. Using this integral and the tabulated σ value, one can tabulate $\log(s(e^t))$ in exactly the same manner as σ, since s needs to be evaluated on a fairly fine grid to compute $\tilde{s}(\omega)$. Again, about 100 points seems to suffice in the tabulation. Then, using the tabulated value, one computes s at typically 1024 or 2048 points for θ ranging out to about 5 times the largest angles of interest. This table can then be Fourier transformed to provide $\tilde{s}(\omega)$ from which $\tilde{g}(z, \omega)$ is calculated for any film thickness.

To compute $f(z, \theta)$, we use Eq. (11) and a modified form of the change of variable suggested in Eq. (15), $\eta = \frac{1}{2}\sqrt{\omega^2 + \omega_{1/2}^2} \cdot \tan(\phi)$, to obtain the following result:

$$\tilde{\gamma}(z, \omega) = 2\sqrt{\omega^2 + \omega_{1/2}^2} \times \int_0^{\phi_{\max}} \frac{\tilde{g}\left[z, \sqrt{\dfrac{\omega^2 + \omega_{1/2}^2}{\cos^2(\phi)} - \omega_{1/2}^2}\right] d\phi}{\cos^2(\phi)}, \tag{16}$$

where $\phi_{\max} = \arccos(((\omega^2 + \omega_{1/2}^2)/(\omega_{\max}^2 + \omega_{1/2}^2))^{1/2})$ above, with the cutoff $\omega_{\max}$ set to the highest frequency being included in the transform. The parameter $\omega_{1/2}$ is the estimated half-width of $\tilde{g}$, as described below. This modified change of variable correctly accounts for the fact that $\tilde{g}$ is not singular at $\omega = 0$, as is $\sigma(\theta)$ at $\theta = 0$, and reduces to the previous one in the limit $\omega_{1/2} \to 0$. When the inverse transform is computed according to Eq. (12), the result is $f(z, \theta)$, the scattering density at polar angle θ away from the initial beam direction.

To avoid computing many unnecessary values of $\tilde{\gamma}(z, \omega)$ (which is a relatively slow process), it is useful to adaptively determine the range of $\tilde{\gamma}(z, \omega)$ which contains real information. We accomplish this by numerically measuring the half-height point $\omega_{1/2}$ of $\tilde{g}(z, \omega)$ from Eq. (10). We have empirically determined that $\tilde{\gamma}(z, \omega)$ is typically about twice as wide as $\tilde{g}(z, \omega)$, so by sampling $\tilde{\gamma}(z, \omega)$ at 20 points, ranging from $\omega = 0$ to $\omega_{\max} = 8\ \omega_{1/2}$, we have included frequency components ranging from about 1/5 of the half-width of the actual spectrum to about four half-widths. This sampling includes essentially all the information, since the spectrum decreases quite quickly with increasing frequency. However, if for any particular application, the result is not sufficiently accurate, the sampling density can always be increased. The inverse Fourier transform of the sampled function $\tilde{\gamma}(z, \omega)$ (with zero padding of higher frequency values out to typically 128 points) is then the final scattering distribution for the foil thickness and cross section chosen.

We have implemented the above algorithms in the form of a *Mathematica*® [16] package, for the sake of simplicity of use and portability. Although one could surely create a compiled program in, for example, C, which would run much faster than our version, it is probably not worth the effort for most applications. Running *Mathematica*® on an Apple Macintosh Quadra 800 (33 MHz 68040 CPU), the time required for the entire process of generating an angular distribution from a cross section is typically about 1 min. However, if the distribution is required for more than one film thickness, it requires of order 10 s starting with an $\tilde{s}(\omega)$ table to compute each new distribution.

4. Results and discussion

In this section we present a comparison of the results of a computation using our algorithm with previous work, a comparison of multiple scattering for three different cross sections and two foil thicknesses, and a computation of the effect on multiple scattering of hydrogen in the scattering foil. The beam species and energy which we have chosen is 270 keV He. This is the most common beam which we use for medium energy backscattering. Fig. 1 shows the angular distribution of He after passing through a 2 $\mu g/cm^2$ carbon foil, typical of the thickness that is used in time-of-flight spectrometers. The scattering cross section which has

been used is the approximate Lenz–Jensen cross section given by Sigmund and Winterbon [6]. Also shown in Fig. 1 for comparison is the result of a computation using the Hankel-transform method described in ref. [6]. The graph has been plotted on a log scale to emphasize the range over which the two curves agree. We have deliberately chosen the parameters of our computation to emphasize the disagreement at large angles. The error in the tail of our curve is an intrinsic artifact of the use of the FFT. The periodic boundary conditions which are inherent in this technique cause the distribution function to be over-estimated at the boundary by a factor of two. It is possible to achieve any reasonable accuracy over a specified range of angles by selecting the total range to be large enough. In this case, we specified a region of interest which included approximately five half-widths of the distribution. The result was excellent agreement over nearly four orders of magnitude in the distribution function. This was achieved while saving several orders of magnitude in computer time relative to the Hankel-transform method.

For practical computations needed in the analysis of time-of-flight spectrometers it is not necessary to demand the large dynamic range shown in Fig. 1. Fig. 2 shows the result of the same 270 keV He beam, again on a 2 $\mu g/cm^2$ carbon foil, but this time with three different assumptions about the scattering cross section. The lower curve represents the (completely unphysical) result obtained from unshielded Coulomb scattering. The two upper curves are more realistic. They were obtained using screened Coulomb interactions with a Lenz–Jensen screening function [14] for the lower curve and the Ziegler–Biersack–Littmark universal screening function [17] for the upper curve. In each case, the cross sections were computed exactly

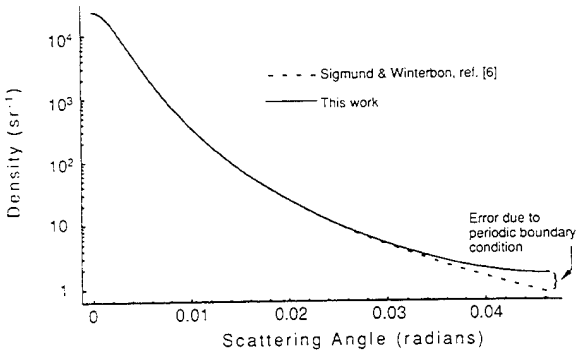

Fig. 1. A comparison of the multiple scattering angular distribution for 270 keV He on 2 $\mu g/cm^2$ C foils as computed by the methods of Sigmund and Winterbon [6] and this work. The discrepancy at large angles is the result of our use of periodic boundary conditions and can be reduced by simply extending the angular range of the calculation.

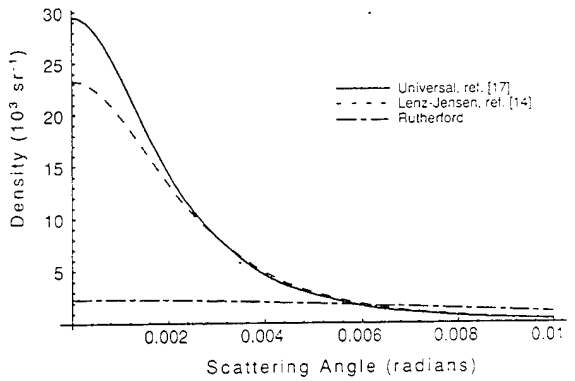

Fig. 2. A comparison of the computed multiple scattering angular distributions for 270 keV He on 2 $\mu g/cm^2$ C foils for Rutherford, Lenz–Jensen [14], and universal [17] cross sections.

using an improved version of the algorithms described in ref. [18].

In ref. [18], we concluded that Lenz–Jensen screening is more appropriate for computing scattering cross sections of interest for medium energy backscattering. Our preference for this screening over the more-recently-developed universal screening was based, in part, on the failure of the latter to agree with Hartree–Fock results near the origin. In fact, the universal screening was developed for stopping power where soft collisions dominate. Thus, we might expect that for multiple scattering it is a better representation of nature.

Fig. 3 shows curves identical to Fig. 2 except that the foil thickness is 100 $\mu g/cm^2$. Notice that the difference between the Lenz–Jensen and universal screening functions is diminished for thicker foils.

Fig. 4 shows the effect on the multiple scattering distribution of the addition of hydrogen to the scattering foil. From top to bottom the curves represent multiple scattering by $10^{18}/cm^2$ of pure C, CH, and

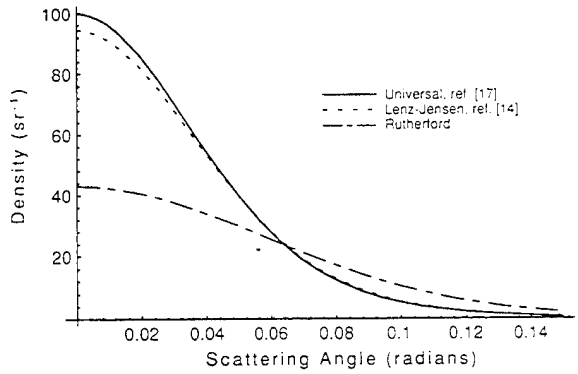

Fig. 3. A comparison of the computed multiple scattering angular distributions for 270 keV He on 100 $\mu g/cm^2$ C foils for Rutherford, Lenz–Jensen [14], and universal [17] cross sections.

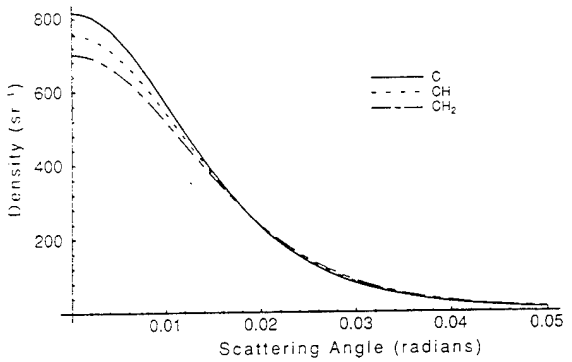

Fig. 4. A comparison of the computed multiple scattering angular distributions for 270 keV He on foils containing 10^{18} carbon atoms/cm^2 in the form C, CH and CH_2. The cross section was derived from the universal screening function [17].

CH_2. Again the projectile is He^+. This figure is particularly significant since it cannot be inferred from the tables of Sigmund and Winterbon [6]. It is perhaps the greatest strength of the new method that multiple scattering can be evaluated in compound targets as easily as in elemental ones. As this figure shows, even a low mass constituent can significantly affect the number of particles which strike a fixed aperture upstream of a scattering foil.

5. Conclusion

Routine computations of time-of-flight detector efficiency require fast and accurate evaluation of the multiple scattering produced by ions passing through 1–10 μg/cm^2 foils. By using the axial symmetry of the problem in a novel way, we have constructed algorithms for computing multiple scattering which are independent of any specific choice of cross section, able to handle compound targets, independent of any specific assumptions about computer hardware or software, and fast enough to make ab initio computations practical on currently available desktop computers. These algorithms are sufficiently general that they can provide mathematical precision comfortably exceeding that of the scattering potentials and the small-angle approximation while still rendering angular distributions in reasonable computing time. The results of such computations will form the basis of a mathematical model of time-of-flight spectrometer efficiency which will be discussed in a forthcoming paper.

Acknowledgments

This work was supported in part by the U.S. Army Research Office under contract DAAL 03-92-G-0037 and by Sandia National Laboratories under contract AH-3292.

References

[1] M.H. Mendenhall and R.A. Weller, Nucl. Instr. and Meth. B 47 (1990) 193.
[2] J.H. Arps and R.A. Weller, Nucl. Instr. and Meth. B 90 (1994) 547.
[3] W.T. Scott, Rev. Mod. Phys. 35 (1963) 231.
[4] J.B. Marion and B.A. Zimmerman, Nucl. Instr. and Meth. 51 (1967) 93.
[5] L. Meyer, Phys. Status Solidi (b) 44 (1971) 253.
[6] P. Sigmund and K.B. Winterbon, Nucl. Instr. and Meth. 119 (1974) 541, and Nucl. Instr. and Meth. 125 (1975) 491.
[7] P. Jaracz and S. Mirowski, Nucl. Instr. and Meth. B 43 (1989) 210.
[8] P. Bauer, E. Steinbauer and J.P. Biersack, Nucl. Instr. and Meth. B 64 (1992) 711.
[9] D.J. Schlyer and P.S. Plascjak, Nucl. Instr. and Meth. B 56/57 (1991) 464.
[10] W. Magnus, F. Oberhettinger and R.P. Soni, Formulas and Theorems for the Special Functions of Mathematical Physics (Springer, New York, 1966) p. 397.
[11] H.A. Bethe, Phys. Rev. 89 (1953) 1256.
[12] W.H. Press, B.P. Flannery, S.A. Teukolsky and W.T. Vetterling, Numerical Recipes in C (Cambridge University Press, Cambridge, 1988) p. 407.
[13] Carl de Boor, in: Mathematical Software, ed. J.R. Rice (Academic Press, New York, 1971) p. 417.
[14] P. Loftager, F. Besenbacher, O.S. Jensen and V.S. Sorensen, Phys. Rev. A 20 (1979) 1443.
[15] J.F. Ziegler, J.P. Biersack and U. Littmark, The Stopping and Range of Ions in Solids (Pergamon Press, New York, 1985) p. 202.
[16] Wolfram Research, Inc., *Mathematica*, version 2.2.1 (Champaign, Illinois, USA, 1993).
[17] J.F. Ziegler, J.P. Biersack and U. Littmark, op. cit., p. 48.
[18] M.H. Mendenhall and R.A. Weller, Nucl. Instr. and Meth. B 58 (1991) 11.

5. Energy dependence of calcium fluoride thin film erosion

Energy Dependence in the Degradation of Calcium Fluoride Thin Films Irradiated by Helium Ions

Martha Riherd Weller

Middle Tennessee State University, Murfreesboro, TN 37132

Mark E. Miklis and Robert A. Weller

Vanderbilt University, Nashville, TN 37235

Abstract

We have investigated composition changes in calcium fluoride thin films bombarded by helium ions with energies between 120 keV and 270 keV, using medium energy backscattering to determine film compositions before and after irradiation. Films were also monitored during irradiation. At all energies, we observed a monotonic decrease in fluorine concentration with no concurrent loss of calcium. The rate of fluorine loss per incident helium ion showed a slight increase with increasing bombardment energy. This suggests that the phenomenon is associated with the loss of energy by the helium ion to electrons in the solid rather than through processes involving nuclear or whole atom collisions.

Introduction

Metallic halides are important materials with a range of practical uses. Magnesium fluoride is a common antireflective coating for optical devices and calcium fluoride is frequently used in multilayer optical coatings. These materials are also useful for semiconductor device applications[1] because they can be grown epitaxially on silicon. In both applications, thin metallic halide films may be placed in environments where they are exposed to particle radiation. Fluorine loss is known to occur in these films during irradiation by electron[2], photon[3], or ion[4,5] beams. In fact, calcium fluoride and other alkaline earth halides have been suggested as potential materials for three-dimensional integrated circuits because of their tendency to lose fluorine under these conditions.

Because of the detrimental effects of thin film degradation in many applications and the usefulness of the same phenomenon for other applications, it is important to understand both the extent of fluorine loss in these films and the mechanisms responsible. Losses from both electron and photon irradiation have been ascribed[3,6] to the formation and subsequent desorption of F^+ from the surface via the Knotek-Feibelman mechanism. However, the work of Mendenhall and Weller[4,5] suggests that other processes must be invoked to explain the fluorine losses during ion bombardment. Most of the fluorine in CaF_2 and MgF_2 films was lost during irradiation by 250 keV He^+ ions. While these losses might result from desorption of fluorine atoms from the surface, enhanced mobility of the fluorine atoms within the film is required to account for losses below the surface. It is also possible that non-electronic processes are responsible for the loss of fluorine during ion bombardment. The purpose of this work is to further elucidate the governing mechanisms for fluorine loss during ion bombardment by measuring the rate of fluorine loss from CaF_2 thin films as a function of the energy of incident He^+ ions.

Experimental Procedure

We prepared a set of targets, each consisting of a CaF_2 thin film which was vapor deposited onto a high purity beryllium substrate. After deposition, a preliminary analysis of each target

was made at several locations by time-of-flight medium energy backscattering using 270 keV helium ions. This analysis indicated a uniform composition for all of the thin films. We also determined that the film thickness was uniform over an area of at least 1 cm^2 on each target and varied by less than 10% from its mean value of 35 nm when comparisons were made between targets.

The He^+ irradiation consisted of three distinct operations. We used 270 keV helium ions to analyze the composition of two or three locations on the target prior to extensive sputtering of the target. After these analyses, the helium beam energy was decreased to the selected irradiation energy. These energies ranged from 120 keV to 270 keV. After a second analysis of the target at the new beam energy, a beam scanner was activated to insure uniform exposure of the selected region during the irradiation process. Targets were exposed for a dose which ranged between 20 mC/cm^2 and 40 mC/cm^2. During this period, the target composition was monitored by time-of-flight analysis of the scattered helium ions. These data were not expected to accurately reflect the composition of previously analyzed regions because of possible edge effects. Nevertheless, they did provide a real time indication for the evolution of the target composition. After the irradiation was completed, the beam scanner was de-activated and the target was analyzed at both the sputtering energy and at 270 keV. Locations for analysis after irradiation were the same as those before irradiation. One of these locations was at the center of the irradiated region while at least one lay well outside the irradiated region. The latter location thus served as a control for data analysis purposes. Sample analyses at all energies were performed using a beam dose of 24 μC.

Irradiation and analysis were performed in an ultra-high vacuum system with a base pressure which was typically below 10^{-9} Torr. However, during irradiation, the indicated pressure rose to values in excess of 10^{-7} Torr. Since the gas load was primarily helium, it was not expected to significantly affect interaction of the ion beam with the sample. However, it did lead to difficulties with current integration which were resolved in the process of data analysis.

Another significant source of experimental uncertainty in our measurement was the determination of the size of the irradiated area. This was done by direct measurement of the damaged area of the samples after irradiation. The results are uncertain by approximately 20% leading to a similar uncertainty in the charge per square centimeter for the sputtering dose.

Results

Fig. 1 shows typical time-of-flight spectra obtained from the irradiated portion of a sample before and after the irradiation. In all cases, we found a significant (≈10% in most cases) increase in the area of the calcium peak for both irradiated and unirradiated regions of the sample. The area of the fluorine peak increased by a comparable amount for unirradiated regions of the target, confirming that the target composition was unchanged in that region. In irradiated regions of the target, the area of the fluorine peak decreased in most cases. Comparison with the calcium peak showed an increase in the Ca/F ratio for all irradiated regions of the target.

The apparent increase in the size of all the peaks in the unirradiated regions is attributed to inaccuracies in current integration due to increased pressure in the target chamber during the final analyses of the target, rather than to actual changes in the target thickness. This hypothesis was confirmed by converting the time-of-flight spectra to energy spectra and calculating the target thickness from the widths of the calcium and fluorine peaks. Using this procedure, the thickness of the unirradiated region of the target was found to be unchanged from its original value.

While the Ca/F ratio for both regions of the target could be calculated directly from the ratio of counts in each peak (after appropriate scaling for the cross sections and for detector effects), the absolute areal densities of Ca and F were more difficult to determine. As noted above, target thicknesses for the unirradiated regions could be calculated from peak widths. This was not possible for irradiated regions because the target composition was no longer uniform with depth into the film. However, since changes in the target chamber pressure occurred primarily while the targets were being irradiated and not during the relatively short analysis period, it is

reasonable to assume that errors in current integration during final analysis were the same for all points on a given target. Areal densities of Ca and F for the irradiated regions were calculated by scaling the analysis charge inversely as the ratio of counts in the unirradiated control regions before and after sputtering.

Fig. 2 shows a comparison of the target composition for one of the targets before and after irradiation. This figure was obtained by converting time-of-flight spectra to energy spectra and then scaling the final analysis by the factor obtained from the unirradiated region of the target. In this figure, the Ca peak is taller and narrower after irradiation compared with before while the F peak is reduced in both height and width. Integration of both peaks shows that the total number of Ca atoms is essentially unchanged while there is a significant decrease in the number of F atoms. Qualitatively similar results were obtained for the irradiated regions of all targets.

The rate of fluorine loss per incident helium ion was calculated for each target. Fig. 3 shows the results of this calculation plotted as a function of helium energy. The datum at 250 keV is from Mendenhall and Weller.[4] Since all targets were not irradiated for the same incident charge per area, results were adjusted to obtain a loss rate corresponding to an irradiation dose of 30 mC/cm^2 for all targets. This was done by assuming an exponential decrease in the fluorine concentration as was observed previously in similar measurements.[4,5] Monitoring of our targets during bombardment showed a monotonic decrease in the Ca/F ratio consistent with this assumption. Experimental errors for the loss rates shown in the figure are approximately 20%, arising primarily from uncertainties in the measurement of the area irradiated on each target.

Discussion

Fig. 3 shows that the rate of fluorine loss from a target bombarded by He^+ ions has little or no energy dependence over the range from 120 keV to 270 keV. We would expect the process which governs fluorine loss to show a similar variation with energy in this range. In fig. 3, we show the functional dependences for both the electronic and nuclear energy loss of He^+ in CaF_2

as well as the Lenz-Jensen elastic scattering cross section for He^+ scattering from F at 150°, all normalized to the datum at 270 keV. In the energy range from 120 keV to 270 keV, the Lenz-Jensen cross section decreases by an order of magnitude and the nuclear stopping power decreases by a factor of two. In contrast, the electronic stopping power increases slightly over this range.

Mendenhall and Weller[4] have suggested that the relatively large rate of fluorine loss is a consequence of fluorine desorption at the target surface combined with an enhanced mobility of fluorine ions within the target which act to replenish the target surface. This enhanced mobility could, in principle, be correlated either with nuclear energy loss via radiation enhanced diffusion processes or with electronic energy loss. The energy dependence of the fluorine loss rate strongly suggests that the process is not significantly influenced by nuclear energy loss or by processes associated with single knock-on collisions between the helium ions and the fluorine atoms. (The absence of concurrent calcium loss also argues against the effectiveness of these mechanisms at these energies.) However, CaF_2 is known to be an ionic conductor when heated with an activation energy for the mobility of vacancies at 200°C which is less than 1 eV.[7] Significant vacancy mobility may be generated in the irradiated region as a consequence of electronic stopping, leading to migration of fluorine to the surface. To further elucidate the significance of electronic energy loss for fluorine loss during ion bombardment, this measurement should be repeated over a wider energy range corresponding to more significant variation in the electronic stopping power.

A less interesting explanation for fluorine loss in irradiated targets is suggested by the physical structure of vapor deposited films. As noted by Allen et al.[8], such films exhibit a columnar structure and are highly porous as a result. Fluorine atoms may desorb from the columnar surfaces via processes similar to those resulting in fluorine loss during electron and photon irradiation. These atoms then percolate to the top of the film and are lost. To rule out this less interesting possibility, our experiment should be repeated with less porous films such as epitaxially grown CaF_2 films.

Conclusions

In CaF_2 films under irradiation by 120 - 270 keV He^+ ions, significant loss of fluorine occurs while the areal density of Ca remains unchanged. The flourine yield was found to be approximately constant in the energy region investigated as would be the case for an erosion mechanism driven by electronic energy loss. However, fluorine loss due to migration through the porous film cannot be ruled out. The data appear to be inconsistent with a mechanism based upon nuclear energy loss or upon single knock-on collisions between He^+ and fluorine.

The authors wish to thank James Arps and Victor Montemayor for invaluable assistance. We acknowledge, with thanks, the support of the Middle Tennessee State University faculty research program, Texas Instruments, Inc., and the United States Army Research Office for its support of the continuing development of medium energy time-of-flight particle spectrometry.

Figure Captions

Figure 1: Time of flight spectra obtained from 35 nm CaF_2 film before and after irradiation with 120 keV He^+ ions.

Figure 2: Equivalent energy spectra for 35 nm CaF_2 film before and after irradiation with 120 keV He^+ ions. The spectrum obtained after irradiation has been scaled to correct for current integration differences.

Figure 3: Rate of fluorine loss as a function of energy. The datum at 250 keV is from Reference [2]. Also shown are electronic and nuclear energy losses for He^+ in CaF_2 as well as the Lenz-Jensen elastic scattering cross sections for scattering from F at 150°. These functions are all normalized to the datum at 270 keV.

References

1 L.J. Showalter and R.W. Fathauer, CRC Critical Reviews in Solid State and Materials Science **15**, 367 (1989).

2 C.L. Strecker, W.E. Moddeman and J.T. Grant, J. Appl. Phys. **52**, 6921 (1981).

3 U.O. Karlsson, F.J. Himpsel, J.F. Morar, F.R. McFeely, D. Rieger, and J. A. Yarmoff, Phys. Rev. Lett. **57**, 1247 (1986).

4 M. H. Mendenhall and R. A. Weller, Nucl. Instr. and Meth. **B51**, 400 (1990).

5 M. H. Mendenhall and R. A. Weller, Appl. Phys. Lett. **57**, 1712 (1990).

6 K. Miura, K. Sugiara and H. Sugiara, Surf. Sci. Lett. **253**, L407 (1991).

7 R. W. Ure, Jr., J. Chem. Phys. **26**, 1363 (1957).

8 T. H. Allen, J. P. Lehan, and L. C. McIntyre, in *SPIE Vol. 1323 Optical Thin Films III: New Developments*, 277 (1990)

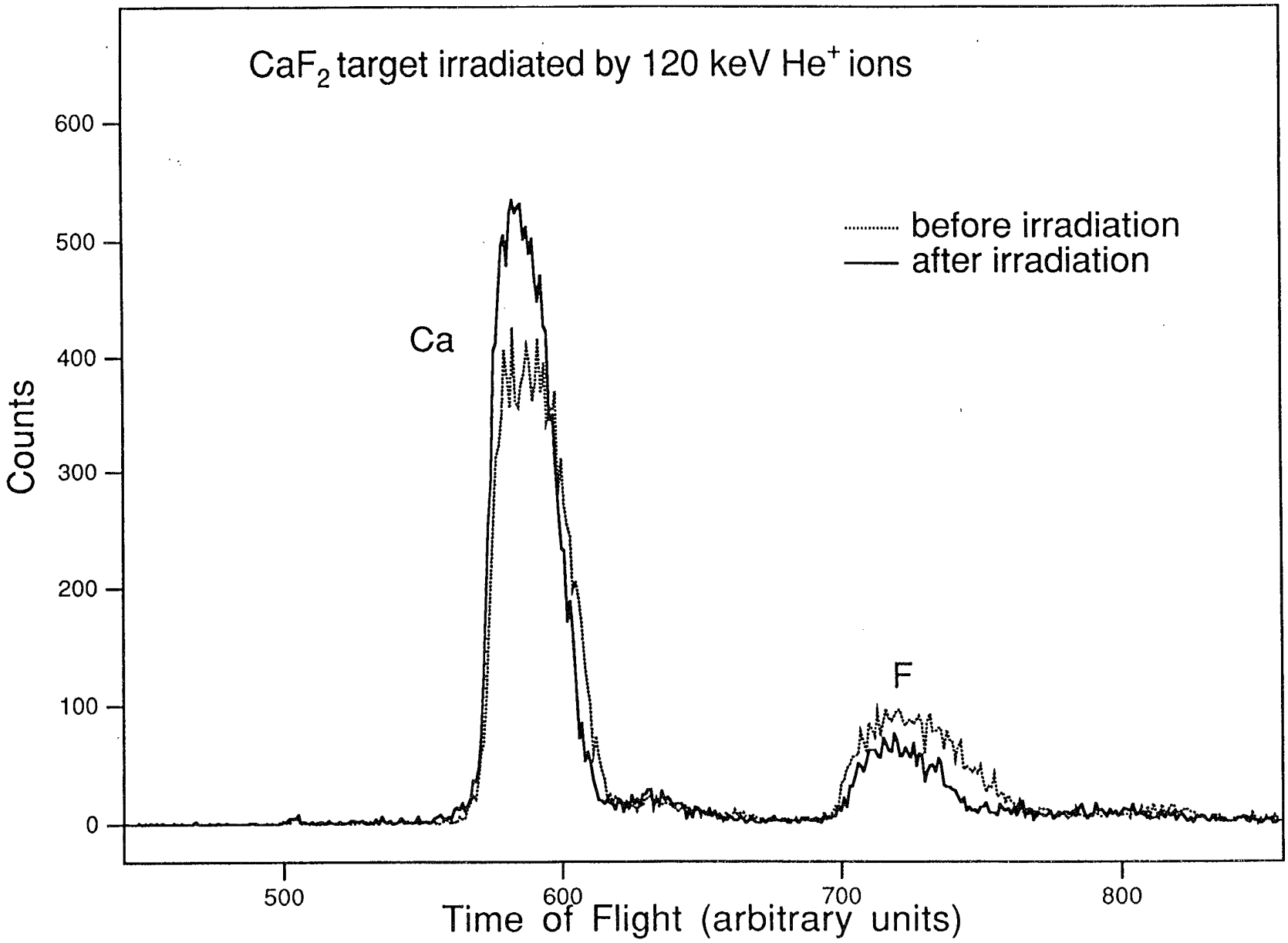
CaF2 target irradiated by 120 keV He+ ions
before irradiation
after irradiation
Ca
F
Counts
0
100
200
300
400
500
600
500
600
700
800
Time of Flight (arbitrary units)

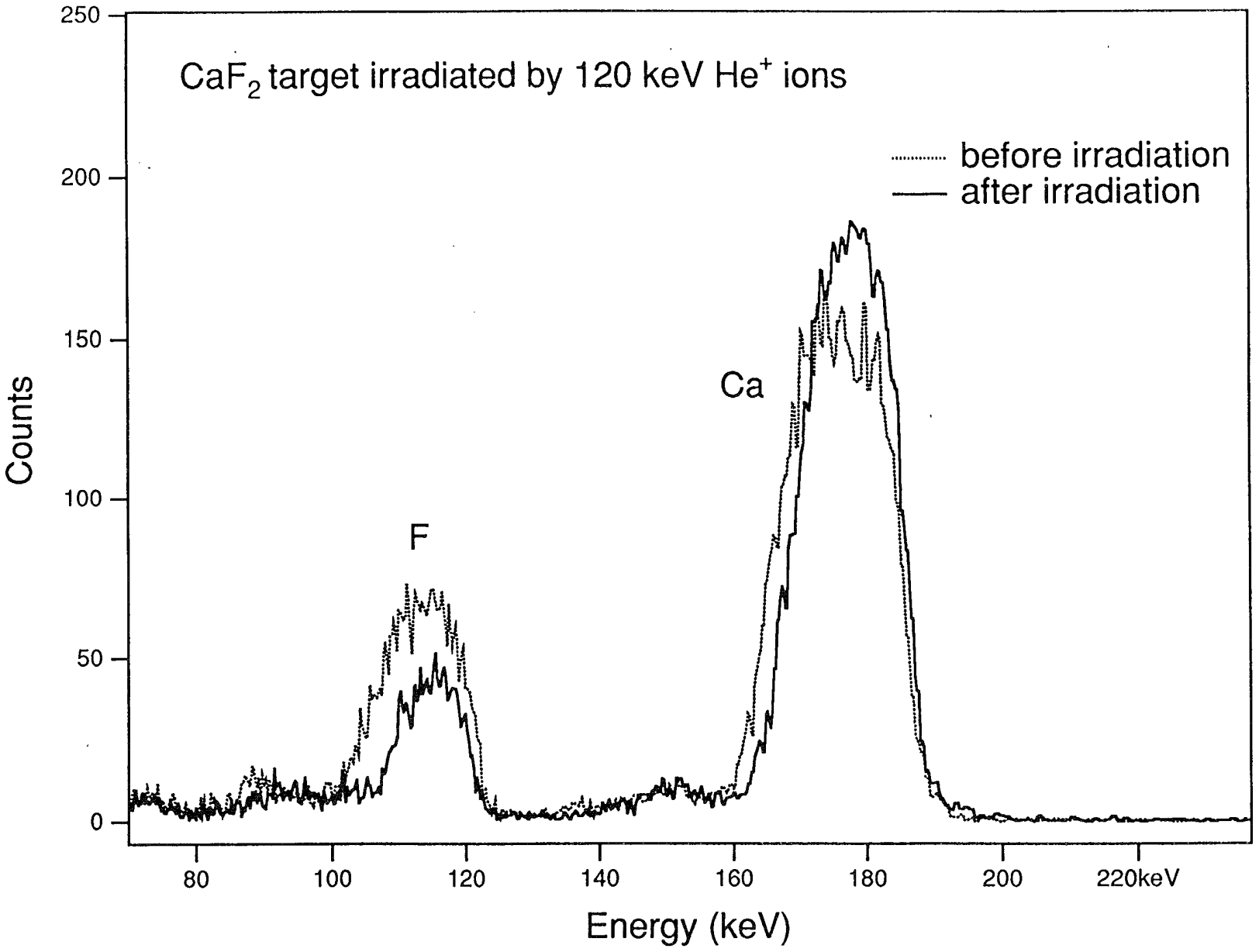
CaF2 target irradiated by 120 keV He+ ions
before irradiation
after irradiation
Ca
F
Counts
Energy (keV)
250
200
150
100
50
0
80
100
120
140
160
180
200
220keV

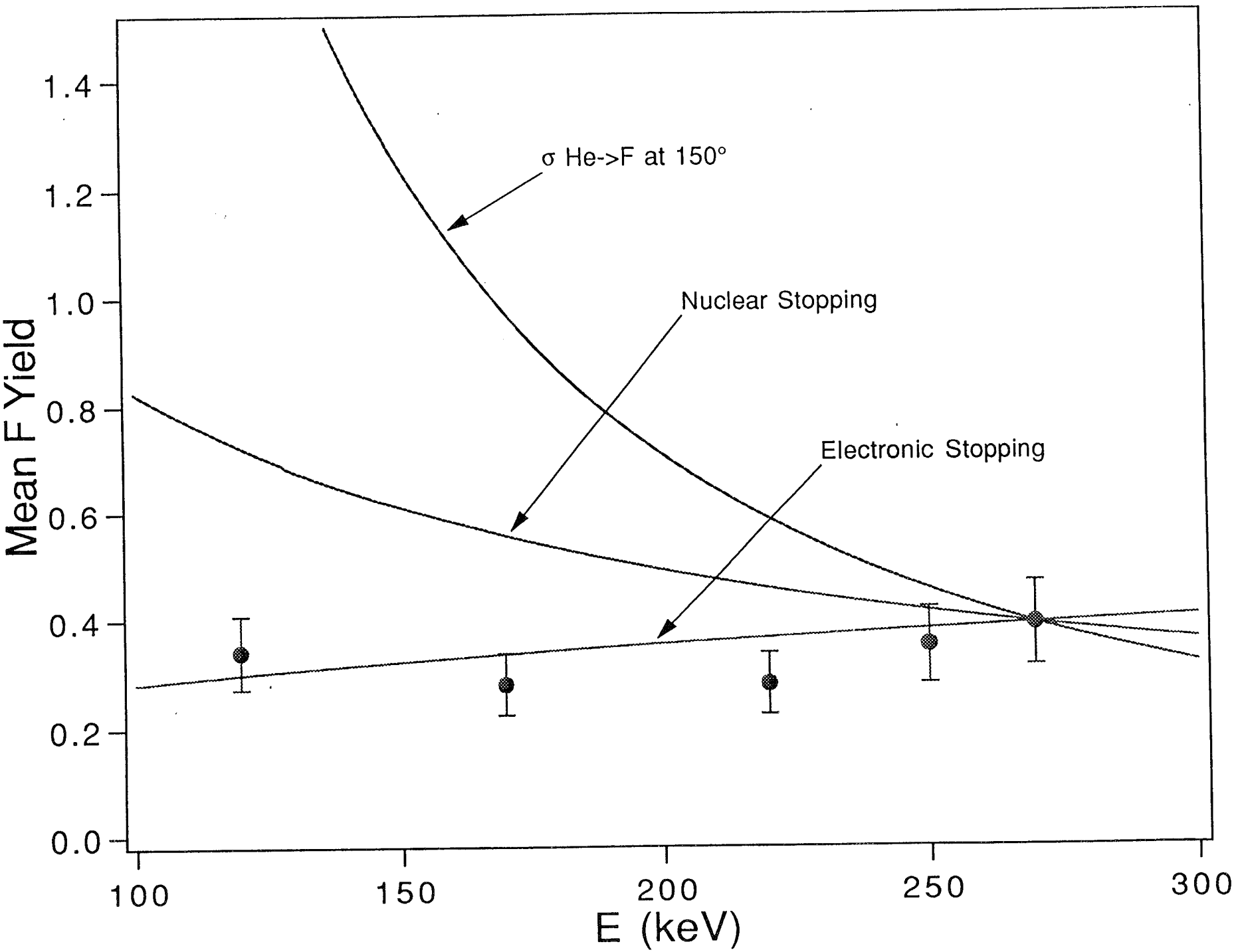
σ He->F at 150°
Nuclear Stopping
Electronic Stopping
Mean F Yield
E (keV)
0.0
0.2
0.4
0.6
0.8
1.0
1.2
1.4
100
150
200
250
300

6. A model of time-of-flight spectrometer efficiency

Nuclear Instruments and Methods in Physics Research A 353 (1994) 579–582

NUCLEAR INSTRUMENTS & METHODS IN PHYSICS RESEARCH Section A

ELSEVIER

A model of the intrinsic efficiency of a time-of-flight spectrometer for keV ions

Robert A. Weller *, James H. Arps, Diane Pedersen, Marcus H. Mendenhall

Vanderbilt University, Nashville, Tennessee 37235, USA

Abstract

We have constructed a first-order model of the intrinsic efficiency of a time-of-flight spectrometer for medium energy ions. The spectrometer uses secondary electrons from a thin carbon foil to generate a start signal and ion impact on a microchannel plate to generate the stop signal. The model includes the effects of the secondary electron yield, multiple scattering in the foil, and the response of the individual microchannel plates which comprise the instrument. We describe the model and the variation of the predicted efficiency with model parameters. Comparisons with measured efficiencies for several ions and energies ranging from 40 keV H to 500 keV O indicate that the model's predictive power is satisfactory for interpreting the results of routine surface analyses.

1. Introduction

Time-of-flight spectrometers are important tools for ion beam analysis of surfaces because they share many of the features, such as wide dynamic range and an insensitivity to a particle's charge state, which have made silicon surface barrier detectors uniquely effective for charged-particle spectrometry at tandem accelerator energies. At particle energies of tens to hundreds of keV, where surface barrier detectors are less useful, especially for heavy ions, time-of-flight spectrometers are the tools of choice for routine thin film analysis [1,2]. However, unlike surface barrier detectors which are usually assumed to have unit intrinsic efficiency, time-of-flight spectrometers have an energy-dependent efficiency which is typically considerably less than one.

In a previous publication, we examined the implications of the efficiency of a spectrometer for the shape of measured spectra and the amount of random coincidence background which these spectra contain [3]. We also suggested that the principal physical processes which limit a spectrometer's efficiency are secondary electron emission and multiple scattering in the start-foil assembly. In a subsequent publication, we presented measurements of the intrinsic efficiency of two similar time-of-flight spectrometers and compared the data with preliminary calculations based on the effects of these processes [4]. In this publication, we present a further elaboration of the efficiency model which includes a component describing the stop detector. While, in principle, this model has no adjustable parameters, in most cases the actual values of the variables are not known precisely. Thus, we explore the variation of the predicted efficiency with changes in these parameters. As we shall see, it is possible to obtain quite reasonable agreement with the results of experiments for a set of values of the parameters all of which are plausible, if not necessarily equal to a priori estimates. Indeed, our earlier speculation that it may be possible to obtain adequate estimates of efficiencies for various ions and energies using only one parameter to characterize a spectrometer continues to be a useful approximation. In its present form, this model is a useful tool both for summarizing and extrapolating the results of experimental calibrations and for evaluating the performance of hypothetical spectrometer designs.

2. The efficiency model

Fig. 1 shows a schematic of the spectrometer configuration to which the following considerations apply. Start pulses are produced when secondary electrons emitted from an electrically biased carbon foil mounted on the middle of three identical 95% transmission Ni meshes strike a microchannel plate detector (Galileo FTD-2003). The electron trajectories make an angle of 30° with respect to the spectrometer axis. The two outer meshes serve to define the electric field surrounding the foil. Stop pulses

* Corresponding author.

SSDI 0168-9002(94)00750-0

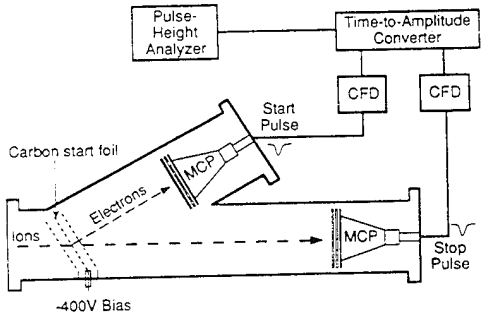

Fig. 1. Schematic of the time-of-flight spectrometer and external electronics consisting of constant fraction discriminators, time-to-amplitude converter and a multichannel analyzer.

are generated when particles impinge directly on the cathode of a second microchannel plate detector approximately 40 cm from the start assembly. A mesh serves to limit the electric field here also. The solid-angle-defining aperture is at the entrance to the spectrometer several cm up-stream of the start foil assembly. The stop detector is biased with its anode at ground potential while the start detector is configured with grounded cathode (or with cathode at about -700 V on older systems). The external electronics are also shown in Fig. 1 although, in the present version of the model, their effects through parameters such as thresholds are not explicitly considered.

The intrinsic (or quantum) efficiency of the spectrometer is defined as the probability that an individual particle entering along the instrument's nominal axis will lead to the generation of a valid event. The factors which determine this efficiency are the secondary electron yield of the start foil, the probability that electrons reach the start detector, the start detector's efficiency for electrons, small angle multiple scattering in the start foil (which causes some particles to miss the stop detector), the efficiency of the stop detector for ions, and finally the collective transmission of the various meshes which are used to control electric fields. External influences such as stray magnetic fields are not considered explicitly.

Measurements of the secondary electron yield as ions exit from thin carbon foils have been reported by Rothard et al. [5]. They report a secondary electron yield per incident ion of $\gamma_C = \Lambda S_C$, where S_C is the electronic stopping power in eV/Å and Λ is a proportionality constant which has the values 0.22 Å/eV, 0.15 Å/eV, and 0.11 Å/eV, respectively for protons, He ions and heavy ions. Since secondary electrons are accelerated to a constant energy of about 400 eV by the bias on the foil, it is only necessary to know a single number for all ions and energies to properly characterize the probability of generating a start pulse. The probability that a single secondary electron generates a start pulse shall be denoted by λ. Then, assuming that the electrons behave independently, the probability that a start pulse is generated when an ion passes through the start foil complex is $1 - e^{-\lambda \Lambda S_C}$.

Fraser has published a study which indicates that the detection efficiency of microchannel plates for few-hundred eV electrons approaches (or may even slightly exceed) the fractional open area of the plates [6]. From the manufacturer's literature, the open area of our plates is about 55%. By rotating the start foil assembly while the spectrometer is operating, we have observed that the size of the electron spot on the microchannel plate is much smaller than the total sensitive area. Thus, electron loss should be small except for the collisions with the mesh which defines the accelerating field. We conclude that a value of 0.5 is a reasonable initial estimate for the parameter λ.

The carbon foils used in our spectrometers are in the range 2–3 $\mu g/cm^2$ or, using the density for carbon of 2 g/cm^3 suggested by the manufacturer, about 10–15 nm thick. This is sufficiently thick that a very significant fraction of the particles are scattered by angles larger than the approximately 2° cone angle subtended by the stop detector. In order to quantify the contribution of multiple scattering, Mendenhall and Weller [7] have developed a set of algorithms based on the fast Fourier transform for computing the multiple scattering angular distribution for arbitrary scattering cross sections. The results of these calculations agree to high accuracy with the published tables of Sigmund and Winterbon [8] and with Monte Carlo simulations based on the TRIM algorithm [9] when the same screening functions are used. The procedure described in Ref. [7] has been used to compute the fraction of particles which fall within a 2° cone after passage through a carbon foil. This function, an implicit function of particle species and energy and foil thickness, is denoted simply as f.

The efficiency of the stop detector for ions has been the most difficult component of this problem to quantify with confidence. Fraser [6] assumed that a microchannel plate produces a pulse if there is at least one secondary electron produced within a microchannel by one of the primary electrons generated by ion impact. The probability that an ion strikes the plate in one of the channels was taken simply as the fractional open area A of the microchannel plate. Poisson statistics was assumed to govern the emission of secondary electrons both by the primary ions and by the electrons themselves. The use of Poisson statistics is certainly not rigorously correct, but as an approximation it is reasonable. The assumption that the outcome of an avalanche is determined exclusively by the first generation of electrons is not very accurate either if the secondary electron yield of the microchannel is too small. Below, we present expressions based upon Fraser's assumption and a generalization which includes additional generations of multiplication.

We denote the number of secondary electrons generated by ion impact within a channel by γ and assume, as with the carbon foil, that γ is proportional to the electronic stopping power. For computing the stopping power, we assume that the surface of the detector is SiO_2, since the

reduced, lead–silicate glass used to make microchannel plates has been observed to have a silica-rich surface layer [10]. (Of course, in some cases ions will impinge directly on the top-surface electrode which is metallic.) The constant of proportionality relating γ and the stopping power is not well known in this case. Rajopadhye et al. and others [11] have published data on secondary electron emission induced by normal-incidence electron impact on Pb glass like that which is used in microchannel plates. However, in practice, particle impacts occur at grazing angles. Moreover, the relative secondary electron yields of protons and electrons under similar conditions have not been extensively studied [12] so that extrapolating the data of Ref. [11] to ions is problematic. Initially, γ was computed using the procedure suggested by Rothard et al. [5] for estimating ion-induced secondary electron yields from a generic metallic surface.

The number of electrons emitted by each electron impact with the walls of a microchannel will be taken to be γ_s. Physical considerations suggest that the value of γ_s must lie in a relatively narrow range. If the average value of γ_s were less than or equal to 1, amplification would not take place. On the other hand, the data of Rajopadhye et al. [11] indicate that the maximum normal incidence yield is approximately 2.5. Thus, even allowing for some variation with the angle of electron impact, γ_s is not expected to be large. The probability that an ion-generated secondary electron fails to initiate an avalanche is $e^{-\gamma_s}$. Using Fraser's criterion that the first stage of amplification determines the outcome of a pulse, we obtain an expression for the microchannel plate's intrinsic efficiency for ions:

$$\eta_s = A\left(1 - e^{-\gamma(1-e^{-\gamma_s})}\right). \quad (1)$$

If γ_s is sufficiently large, say greater than 3, as it usually is in discrete dynode electron multipliers, Eq. (1) is a reasonable approximation. However, if γ_s is smaller, then an avalanche can fail at a later stage. The generalization of Eq. (1) which includes the possibility of failure later in the avalanche includes a continued exponent. Using this more general form and representing the transmission of the spectrometer attributable to meshes as T, the complete expression for the efficiency of the spectrometer is:

$$\eta = ATf\left(1 - e^{-\lambda \Lambda S_C}\right)\left(1 - e^{-\gamma(1-e^{-\gamma_s(1-e^{-\gamma_s(\cdots)})})}\right). \quad (2)$$

Since $A \approx 0.6$ and there are three 95% transmission meshes in the start assembly as well as one at the stop detector ($\approx 90\%$), a value in the range 0.4–0.5 is a reasonable expectation for the product AT.

3. Discussion

Because of the uncertainty in computing γ, in practice we have written the exponent in the final term of Eq. (2) in the form:

$$\gamma\left(1 - e^{-\gamma_s(\cdots)}\right) \equiv g \Lambda_n S_{MCP}. \quad (3)$$

Here S_{MCP} is the electronic stopping power of the ion at the surface of the microchannel plate and Λ_n is a normalized species-dependent factor analogous to Λ above. In the absence of data, the values of Λ_n were taken to be those suggested by Rothard et al. in Eq. (14) of Ref. [5]: 1.0, 0.6, and 0.3 for H, He and heavy ions, respectively. The parameter g is determined, in principle, both by the electron multiplication term in parenthesis on the left side of Eq. (3) and by the secondary electron yield of the microchannel plate though, in practice, it is adjustable. With the definition given in Eq. (3), η has three other parameters which may also be considered to be adjustable within limits: the product AT, the foil thickness, which affects f, and the probability λ. In Ref. [3], we examined the effects of multiple scattering and the start detector response on η. Using the nominal foil thicknesses specified by the manufacturer and assuming a value of 0.3 for λ, we found that it was possible to predict within 10–20% (but with systematic errors) the efficiencies of two similar spectrometers, one used for backscattering and the other for forward recoil studies. The most significant success of that effort was the prediction that the efficiency for detecting hydrogen should peak in the energy range which we examined experimentally. This work led us to the conjecture that it might be possible to characterize a spectrometer approximately by specifying the product AT alone. The systematic differences between the predicted variation of efficiency with energy and the data were attributed to our decision to assume that the stop detector's response was independent of the particle's energy.

With the inclusion of a model for the stop detector, it was reasonable to search in the space of the above parameters for a best fit to the data. This effort was only marginally successful, however, because the parameters are not completely independent. Indeed, for small λ and g, η depends only on the product $AT\lambda g$. Increasing foil thickness also has the same general effect on η as decreasing λ. We found that it was not possible to obtain high quality fits for all data using the a priori values of Λ measured by Rothard et al. [5]. However, the adjustments which were necessary were modest, being typically in the 10–20% range, and were consistent with experimental uncertainties in the data and the computation of stopping powers [13]. We also added a Λ value for Li which was determined from the data to be intermediate between those for He and heavy ions. The values which we have used for Λ in the computations below are 0.26, 0.22, 0.14, and 0.10 for H, He, Li, and heavy ions, respectively. The value 0.17 has been used for λ.

The most surprising result from the nonlinear fitting was that foil thicknesses of 3.6 $\mu g/cm^2$ and 4 $\mu g/cm^2$, respectively, for the 150° and 42° spectrometers were needed in order to achieve the best agreement with the data. These are about 25% larger than the nominal thicknesses (even allowing for the 30° tilt of the foil) and significantly outside the tolerances specified by the manu-

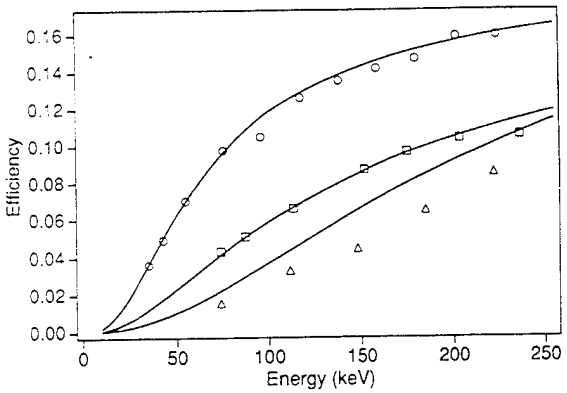

Fig. 2. Comparison of computed and measured efficiencies η of backscattering spectrometer for He (circles), Li (squares) and O (triangles).

facturer. We do not know, at this time, if this is an artifact of the poor orthogonality of the parameters or if the foils are actually unexpectedly thick.

Fig. 2 is a composite showing a comparison between computed values of η (smooth curves) and the measured efficiencies of our backscattering (150°) spectrometer for He, Li, and O. Error bars (estimated to be approximately 10% [4]) have been omitted from the graph for clarity. The value of AT is 0.24. The curves in Fig. 2 were computed with $g = 0.05 \times 10^{15}/(\text{eV cm}^2)$. Corrections for the energy loss is the start foil, both to the energy axis itself and to the multiple-scattering factor, have been investigated and, for these ions and energies, found to be negligible on the scale shown. The results of a comparison between the computed and measured efficiencies of our elastic recoil (42°) spectrometer for H and C are shown in Fig. 3, where an AT value of 0.56 was used but all other parameters were held constant.

The difference in normalization between Figs. 2 and 3 is attributable to the differences between the gains of the microchannel plates in the two spectrometers. In practice, valid low amplitude pulses may be below discriminator

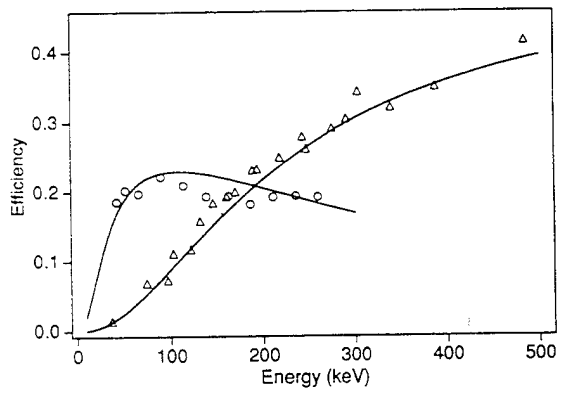

Fig. 3. Comparison of computed and measured efficiencies η of forward recoil spectrometer for H (circles) and C (triangles).

thresholds and therefore lost. This should have the same effect as changing λ and g. Thus, although the one-parameter approximation used in Figs. 2 and 3 is surprisingly robust, the relatively poor agreement obtained for oxygen in Fig. 2 demonstrates that for highest accuracy it is necessary to consider at least the relative performance of the two microchannel plates. Specifically, there is no reason to expect that values of λ or g for different systems with different ages and histories are necessarily equal.

4. Conclusion

A model of time-of-flight spectrometer intrinsic efficiency encompassing the effects of secondary electron emission and multiple scattering in the start foil, along with the efficiency of the stop detector for ions has been shown to be successful in representing measured data for ions ranging from approximately 40 keV H to 500 keV O. It should be an especially useful tool for the analysis of medium-energy, time-of-flight spectra of both backscattered and forward-recoiled ions. It affords reasonable accuracy using a priori values for its parameters and, with fitted values of these parameters, appears to be at least as accurate as other computed quantities such as cross sections and stopping powers which are used in the analysis of experiments.

Acknowledgements

This work was supported in part by the U.S. Army Research Office under contract DAAL 03-92-G-0037 and by Sandia National Laboratories under contract AH-3292.

References

[1] J.A. Knapp and J.C. Banks, Nucl. Instr. and Meth. B 79 (1993) 457.
[2] M.H. Mendenhall and R.A. Weller, Appl. Phys. Lett. 57 (1990) 1712.
[3] R.A. Weller, Nucl. Instr. and Meth. B 79 (1993) 817.
[4] J.H. Arps and R.A. Weller, Nucl. Instr. and Meth. B 90 (1994) 547.
[5] H. Rothard, K. Kroneberger, A. Clouvas, E. Veje, P. Lorenzen, N. Keller, J. Kemmler, W. Meckbach and K.O. Groeneveld, Phys. Rev. A 41 (1990) 2521.
[6] G.W. Fraser, Nucl. Instr. and Meth. 206 (1983) 445.
[7] M.H. Mendenhall and R.A. Weller, Nucl. Instr. and Meth. B 93 (1994) 5.
[8] P. Sigmund and K.B. Winterbon, Nucl. Instr. and Meth. 119 (1974) 541, and Nucl. Instr. and Meth. 125 (1975) 491.
[9] J.P. Biersack and L.G. Haggmark, Nucl. Instr. and Meth. 174 (1980) 257.
[10] A.M. Then and C.G. Pantano, Non-Cryst. Solids 120 (1990) 178.
[11] N.R. Rajopadhye, S.V. Bhoraskar and D. Chakravorty, J. Non-Cryst. Solids 105 (1988) 179, and references therein.
[12] J. Schou, Scanning Microscopy 2 (1988) 607.
[13] J.F. Ziegler, J.P. Biersack and U. Littmark, The Stopping and Range of Ions in Solids (Pergamon, New York, 1985) p. 202.

7. A particle telescope for medium-energy ion beam analysis

Adaptation of particle-telescope technology for medium energy ion beam analysis

James H. Arps, Mark E. Miklis, and Robert A. Weller
Vanderbilt University, Nashville, Tennessee 37235-1807

(Received 10 November 1993; accepted for publication 31 January 1994)

Medium energy (100–300 keV) time-of-flight spectrometry for surface analysis uses the correlated detection of an energetic ion and the secondary electrons emitted as it passes through a carbon foil. When microchannel plates are employed in this detection scheme, a typical mean efficiency of detection of less than 30% is achieved. When instead a surface barrier detector is used to detect the ion, providing simultaneous acquisition of velocity and energy information, certain advantages are realized over the two microchannel plate configuration in the characterization of low level constituents of surfaces. Specifically, energy-discriminated gating of the start pulse was observed to nearly eliminate count rate dependent background in a time-of-flight spectrum. Further reduction in background was obtained by the selective elimination of forward recoil species or backscatters from the substrate. Replacement of the stop microchannel plate by a surface barrier detector has resulted in improved detection efficiency for He, as well as provided a means for further study of the processes which affect time-of-flight spectrometer response, including multiple scattering and secondary electron emission in the start foil. In this publication, we describe the application of this particle telescope to the backscattering analysis of gold on silicon and the forward scattering measurement of hydrogen in a self-supporting carbon film.

I. INTRODUCTION

The term "particle telescope" is generally applied to any detection scheme which records information at two points along the linear trajectory of a particle. Typical measurements include energy loss, total energy, and time-correlated position, from which the particle velocity may be calculated. With knowledge of any two of these parameters, the mass of the particle may be extracted. The first applications of this technology were in nuclear physics, where it was used to characterize recoil nuclei produced by energetic heavy ion reactions.[1] More recently, particle telescopes have been used in the measurement of low Z elements in materials by elastic recoil detection analysis. Organic layers,[2] oxide layers,[3] and implanted materials[4] have been profiled using ion beams with typical atomic numbers from 2 to 20 at energies from 2 to 50 MeV.

In the analysis of the atomic composition of materials using ion beams, it is often sufficient to measure a single quantity such as scattered particle energy or velocity. Our group has applied time-of-flight (TOF) spectrometry using He ions from 100 to 300 keV in the backscattering measurement of thin optical coatings[5] and, recently, to submonolayer coverages of metals on silicon. Control of surface contamination due to iron and nickel is of particular interest to the semiconductor industry in efforts to fabricate defect-free structures. Measurements of heavy metal contaminants on silicon surfaces at levels of the order 10^{11} Pb atoms/cm^2 have been reported using medium energy TOF backscattering with heavy ions.[6] We have also used this method in the analysis of hydrocarbon films by elastic recoil detection.[7] From this experiment, we inferred a sensitivity to hydrogen of order 10^{13} atoms/cm^2.

Two factors which may hinder further improvement in the sensitivity of ion scattering to either light or heavy elements are TOF spectrometer efficiency and intrinsic random coincidence background. Recent experiments have shown that the quantum efficiency of a two microchannel plate TOF spectrometer is less than 30% for low Z ions in the energy range 100–300 keV.[8] Multiple scattering and secondary electron emission from the start foil were identified as primary contributors to detector efficiency. A theoretical investigation of the effect of count rate on TOF spectra showed that a uniform rate dependent background is generated by random start and stop pulses produced by different particles.[9] In the analysis of low level surface constituents where large beam currents may be needed to obtain a statistically significant measurement, this random coincidence background will greatly limit the detectable amount of trace elements.

In this paper, we report a modification to our existing TOF spectrometer design which shows potential for enhancing the sensitivity of ion scattering measurements to low level surface constituents and provides further insight to the processes governing TOF spectrometer efficiency. A passivated, implanted, planar silicon (PIPS) detector has been substituted for the stop microchannel plate to produce a medium energy particle telescope capable of providing TOF and energy information on the detected particles. Improved detection efficiency is realized due to the unit quantum response of the PIPS detector compared to the 50% estimated active area of the microchannel plate. Windows in energy were chosen for the acquisition of gated TOF spectra. When the contribution of PIPS detector noise to the stop count rate is eliminated by setting a minimum energy threshold, random coincidence background is diminished. Elimination of events from the substrate or other scattering features by gating further reduces background. In order to demonstrate some of the capabilities of this technique, two representative samples were considered; a monolayer of gold on silicon and a thin self-supporting carbon film contaminated with residual

 0034-6748/94/65(5)/1575/5/$6.00

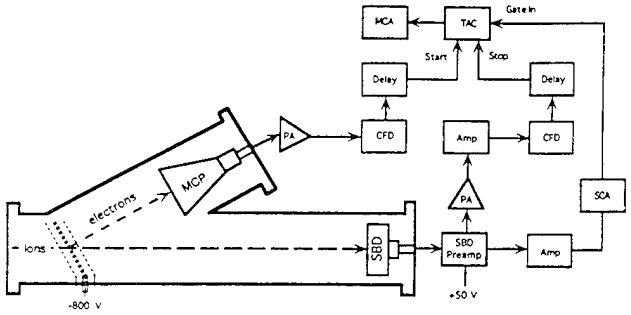

FIG. 1. Schematic of the spectrometer and associated detector electronics.

hydrogen. Some additional ideas for spectrometer design improvements are discussed as are the difficulties associated with using PIPS detectors for medium energy ions.

II. EXPERIMENTAL

A schematic of the apparatus is shown in Fig. 1. Scattered ions or neutrals enter the spectrometer through an aperture and pass through a 3 $\mu g/cm^2$ carbon foil mounted on a 90% transmission nickel mesh which has been biased at -800 V with respect to ground. Grounded meshes positioned 0.5 cm in front and back of the foil define the shape and extent of the electric field. Secondary electrons generated as the ion exits the foil are accelerated toward a microchannel plate assembly with the cathode grounded and the anode biased at $+2200$ V. The ions drift through the spectrometer and strike a passivated, implanted, planar silicon detector (Ortec Ultra-series) with a 50 mm^2 active area and a depletion depth of 100 μm. The flight path from the start foil to the stop detector is approximately 35 cm. The aperture at the entrance to the spectrometer restricts the flux of scatters while a geometric solid angle of 0.1 msr is defined by the active area of the PIPS detector.

A schematic of the electronics used to acquire energy-gated TOF spectra is included in the same figure. Start event markers are generated from the amplified pulses of the microchannel plate by a constant fraction discriminator. The stop event markers from the timing output of the PIPS detector preamp were typically much less than 5 mV in amplitude for medium energy ions, requiring two stages of amplification. Discriminator thresholds in the start and stop channels were optimized to reduce the background count rate while continuing to pass real events. Energy pulses from the stop detector were amplified (0.5 μs shaping) and passed to a single channel analyzer, which produced 500 ns pulses used to gate the time-to-amplitude converter (TAC). A $\sim$3.5 μs delay was added to each timing signal, in order to synchronize them with the gate pulse. A multichannel analyzer sorted the valid TAC events into a 0.25 ns/channel spectrum. The contribution of the external electronics to the detector timing resolution was measured with both detectors uncoupled from the system using a fast pulser ($\sim$1 ns rise time) to serve as a source of start pulses. These triggered a tail pulse generator which provided stop pulses for the PIPS preamp. The timing resolution measured by this method was 1.5 ± 0.3 ns.

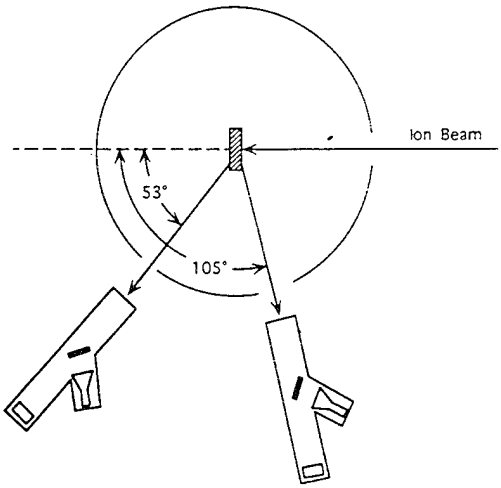

FIG. 2. Layout of forward and backscattering geometries.

The scattering geometry is shown in Fig. 2. Helium ions at 275 keV were directed at normal incidence and backscattered at $\theta=105°$ from a silicon sample having a nominal coverage of gold, verified using our conventional TOF backscattering setup, of $(1.0\pm0.1)\times10^{15}$ atoms/cm^2. In the forward scattering experiment, a self-supporting carbon foil was mounted on a stainless steel support with a 0.5-cm-diam hole. A nominal thickness of $(2.7\pm0.3)\times10^{17}$ atoms/cm^2 was quoted by the manufacturer. H ions at 105 and 275 keV were forward scattered from the foil and detected at $\theta=53°$ and an angle 14° above the horizontal plane. The integrated charge, collected with the beam incident on the foil, was adjusted by the ratio of the current deposited on a solid target to current through the foil in order to approximate the true value.

III. RESULTS AND DISCUSSION

Energy spectra obtained from the PIPS detector are shown in Fig. 3 for 275 keV H and He ions scattered from the carbon film and the gold on silicon. An energy scale was established by measuring thick target edge positions on a number of samples. The estimated energy resolution for H and He from the carbon and gold peaks is approximately 11 and 16 keV FWHM in each case. The fraction of ions detected by the PIPS detector was derived for H and He by taking the ratio of computed to geometric solid angle. The calculation was based on the known values for the number of gold or carbon scattering centers/cm^2, the Lenz–Jensen scattering or recoil cross section, the number of incident ions, and the measured number of counts in the forward and backscattering peaks. The He backscattering and H forward scattering fractions measured by the PIPS detector were $45\%\pm5\%$ and $20\%\pm2\%$, respectively. There are two important processes which give rise to the departure of these values from unit quantum efficiency. First, multiple scattering of the ions as they pass through the carbon start foil can cause them to be deflected out of the acceptance half-angle of the detector. In order to estimate the number of projectiles which are lost, we have made *ab initio* calculations of the multiple scattering distribution functions for H and He ions passing through the start foil using Bethe's equations.[10] Distribution

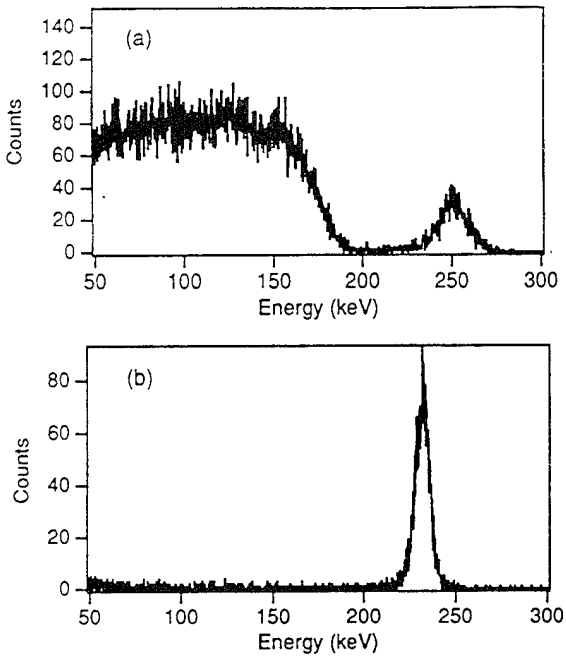

FIG. 3. PIPS detector energy spectra for (a) 275 keV He^+ backscattered from a monolayer of gold on silicon and (b) 275 keV H^+ forward scattered from a 5.4 $\mu g/cm^2$ carbon foil. The charge deposited during each analysis was 12 μC.

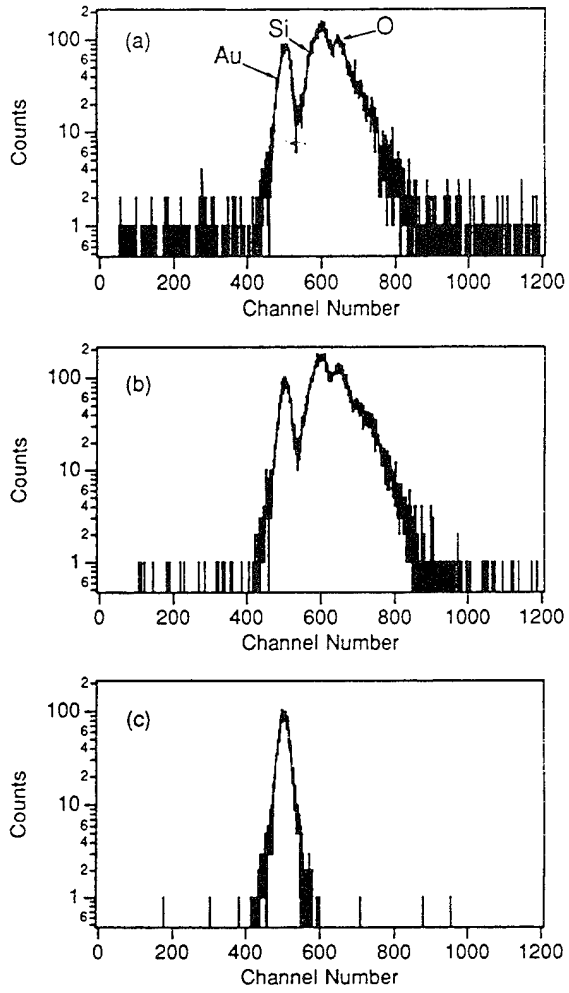

FIG. 4. TOF spectra for 275 keV He^+ on a monolayer of gold on silicon subject to (a) no energy gating, (b) 20 keV, and (c) 215 keV upper level energy thresholds. The charge deposited during each analysis was 18 μC.

functions were computed at 250 keV (the approximate scattered energy of the ions) using the Lenz–Jensen scattering cross section. The angular distributions were numerically integrated over the solid angle subtended by a 0.5° cone to give the fraction of multiply scattered ions falling within the acceptance half-angle of the stop detector. According to these theoretical estimates, 65% of the He and almost 90% of the H should reach the detector. We attribute the remaining discrepancy to misalignments of the detector and start foil with the point where the beam strikes the target. The H efficiency, as measured in the forward scattering geometry, is particularly sensitive to any such misalignment.

The ungated TOF backscattering spectrum for 275 keV He on gold-covered silicon is shown in Fig. 4(a). A logarithmic display is chosen to better demonstrate the subsequent effects of gating on the background. Spectral features attributable to gold, the silicon substrate, and oxygen, presumably from the native silicon oxide layer, are identified. The estimated detection efficiency in TOF mode, again based on measurement of the gold coverage, is 36%±4%. This is an improvement in efficiency nearly twice that of our conventional TOF setup used under comparable conditions. The probability that a start event will be generated by secondary electrons from the foil largely accounts for the reduction in TOF spectrometer efficiency compared with that of the PIPS detector. The probability p that a pulse is recorded when one or more secondary electrons are emitted is simply $p=1-e^{-\lambda n}$, where n is the number of electrons and λ is the probability that a single electron will trigger an event. A value of $\lambda=0.3$, based upon the work of Fraser,[11] reflects the limitations of microchannel plate active area and quantum efficiency for electrons. The yield of secondary electrons is proportional to the electronic stopping cross section of the ion in carbon. A proportionality constant of 0.175 eV/10^{15} atom/cm^2 was derived from recent experimental data published by Rothard and co-workers.[12] Based on this estimate, the probability that a 250 keV He ion will generate a start pulse is approximately 80%.

The effects of two different levels of energy gating on the TOF spectra are shown in Figs. 4(b) and 4(c). In the first case, a minimum energy threshold of 20 keV was set to eliminate pulses which could be attributable to low energy scattered ions or detector noise. For the later case, an upper threshold consistent with an ion energy of 215 keV was set to reject all scatters from the substrate. The random coincidence background in each spectrum was integrated over the entire time range excluding the region containing real events. The total measured background was 516, 41, and 4 counts for the cases of no gating, 20 keV gating, and 215 keV gating, respectively. The total number of counts in the gold peak was unaffected by the gating to within the uncertainty set by counting statistics. The significant reduction in background with increased gate threshold implies improved sensitivity to low levels of metal contaminants. We define a minimally

detectable feature as one whose integrated yield must be three standard deviations above the estimated error in the measurement. A minimum gold coverage of approximately 2×10^{12} atoms/cm^2 should be measurable by the present system, based on the background for the case of 215 keV gating. This lower level could be substantially improved by taking measures to increase the detector solid angle, such as moving the spectrometer closer to the target and using a PIPS detector of larger active area. The later modification would also reduce losses due to multiple scattering.

TOF spectra for protons scattered from the self-supporting carbon foil are shown in Fig. 5. A gating threshold of 20 keV, as in Fig. 5(b) again results in a significant reduction in background over the ungated spectrum 5(a). The ratio of TOF to PIPS detector efficiencies for the forward scattered H off C at 250 keV is 47%±5%. While smaller than the value for He, it is also consistent with estimates based on secondary electron emission and should be insensitive to detector alignment. This is quantitatively understood as the number of secondary electrons emitted by the passage of a H ion will be, in general, less than are generated by a He ion due to the smaller electronic stopping cross section. In Fig. 5(c) upper and lower thresholds were set to pass only ions with an energy below 125 keV, effectively eliminating all proton scatters from the carbon, while continuing to reject low energy events. An additional peak, resolved after collecting with a larger deposited charge, was tentatively identified as representing protons scatters from hydrogen in the foil with a recoil (or scatter) energy of approximately 100 keV. The correct location of the peak was confirmed by scattering a 105 keV H beam off the carbon foil to give ions of the same energy, as shown in Fig. 5(d). The estimated hydrogen concentration in the foil is $(2.0\pm0.2)\times10^{16}$ atoms/cm^2.

The full width at half-maximum timing resolution, measured for the H and He scattering from carbon and gold, was 4.5±0.3 and 6.5±0.3 ns, respectively, and includes the contribution from the external electronics. In comparison, the nominal timing resolution for our two microchannel plate TOF detector is less than 1.0 ns. With the PIPS detector connected, significant time jitter occurs at the output of the detector preamplifier, causing a degradation in resolution. Radio frequency pickup by the detector from the accelerator high voltage source may have been a contributing factor and was due in part to insufficient ground isolation. This reduction in resolution could be compensated for by increasing the total flight distance. Such an improvement in timing resolution would probably be needed if identification of lower mass species by backscattering were attempted using the current setup.

We have demonstrated the application of particle telescope technology to the medium energy backscattering measurement of a gold monolayer on silicon and the forward scattering measurement of hydrogen in thin films. Comparisons of TOF to PIPS detector efficiency for H and He agree with theoretical estimates of the probability for generating a start event based on microchannel plate efficiency and secondary electron emission. Because of limitations in timing, the telescope is not particularly well suited for measurements requiring good depth resolution, such as the determination of

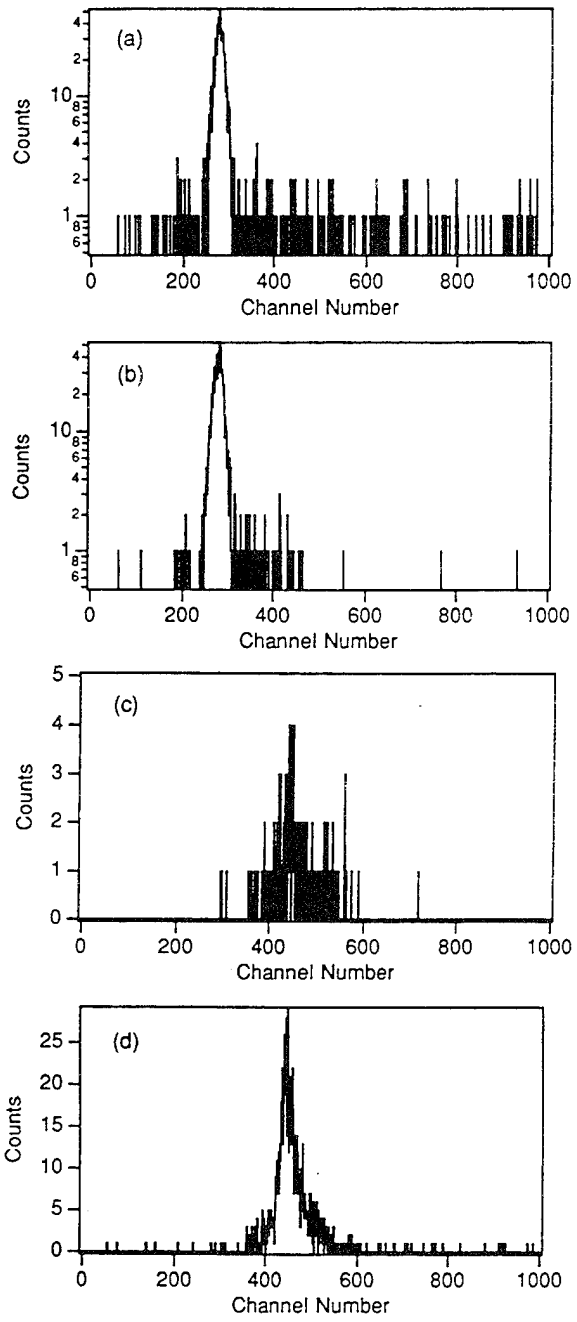

FIG. 5. TOF spectra for 275 keV H^+ on the self-supporting carbon foil subject to (a) no energy gating, (b) 20 keV upper level, and (c) 125 keV lower level energy thresholds. In (d) a 105 keV H^+ was used to produce scatters with the same energy as the ions in (c). The charge deposited was 6 μC for (a) and (b), 48 μC for (c), and 2 μC for (d).

film thickness. The advantage of this technique over TOF or energy measurements alone is in the sensitive detection of low levels of surface contaminants. Selective screening of TOF events by particle energy reduces random coincidence background by roughly two orders of magnitude compared with a two microchannel plate setup, while eliminating contributions from low energy noise and pulse pileup from the surface barrier detector. Further optimization of geometric solid angle, flight path, and PIPS detector active area will be

necessary to produce a design capable of competing with the current state of the art in trace element detection.

ACKNOWLEDGMENT

This work was supported by the U.S. Army Research Office under Contract No. DAAL 03-92-G-0037.

[1] F. S. Landolt and B. G. Harvey, Annu. Rev. Nucl. Sci. **25**, 167 (1975).
[2] J. Sokolov, M. H. Rafailovich, R. A. L. Jones, and E. J. Kramer, Appl. Phys. Lett. **54**, 590 (1989).
[3] H. J. Whitlow, A. B. Andersson, and C. S. Petersson, Nucl. Instrum. Methods B **36**, 53 (1989).
[4] R. Groleau, S. C. Gujrathi, and J. P. Martin, Nucl. Instrum. Methods **218**, 11 (1983).
[5] M. H. Mendenhall and R. A. Weller, Appl. Phys. Lett. **57**, 1712 (1991).
[6] J. A. Knapp and J. C. Banks, Nucl. Instrum. Methods B **79**, 457 (1993).
[7] J. H. Arps and R. A. Weller, Nucl. Instrum. Methods B **79**, 539 (1993).
[8] J. H. Arps and R. A. Weller, Nucl. Instrum. Methods B (in press).
[9] R. A. Weller, Nucl. Instrum. Methods B **79**, 817 (1993).
[10] H. A. Bethe, Phys. Rev. **89**, 1256 (1953).
[11] G. W. Fraser, Nucl. Instrum. Methods **206**, 445 (1983).
[12] H. Rothard *et al.*, Phys. Rev. A **41**, 2521 (1990).

8. Measurement of time-of-flight spectrometer efficiency

Nuclear Instruments and Methods in Physics Research B 90 (1994) 547–551
North-Holland

NIM B
Beam Interactions with Materials & Atoms

Measurement of time-of-flight spectrometer efficiency for light ions at medium energies

James H. Arps and Robert A. Weller *
Dept. of Physics and Astronomy, Vanderbilt University, Box 1807-B Nashville, TN 37235, USA

Medium energy time-of-flight spectrometry is an effective technique for helium backscattering as well as the elastic recoil detection of hydrogen and other light elements. However, the efficiency of a time-of-flight spectrometer, unlike that of a surface barrier detector, depends strongly on the energy and mass of the detected particle. A thorough understanding of this spectrometer quantum efficiency is necessary for quantitative measurements. We report initial measurements of the quantum efficiency of two similar time-of-flight spectrometers in forward and backscattering geometries for hydrogen, helium, and carbon projectiles over the energy range 50–275 keV. The results are compared with predictions of a model which incorporates multiple scattering and secondary electron emission at the carbon start foil along with an energy-independent microchannel plate response. When these processes are taken into account, the efficiency of a spectrometer as a function of projectile species and energy can be described to within experimental error by a single overall calibration constant.

1. Introduction

Carbon-foil-based time-of-flight spectrometry uses timed coincident detection of a projectile and the secondary electrons generated as this projectile passes through a foil placed along its path. Simultaneous acquisition of velocity and energy information is possible, depending on the method used. First applied in nuclear physics to measure recoil velocities of energetic heavy ions, these techniques have found new uses in surface and materials characterization. Employed in conjunction with ion beams with typical atomic numbers from 2 to 20 at energies from 2 to 50 MeV, organic layers [1], oxide layers [2], and materials implanted with low Z elements [3] have been profiled by the time-of-flight detection of elastic recoils. Our group has applied time-of-flight spectrometry at medium energies to both backscattering and elastic recoil detection [4,5].

In ion beam analyses employing a silicon surface barrier detector, the detector's quantum efficiency, the probability that a single-particle impact will generate a detectable event, is usually considered to be unity for particles with reasonable energies. This is in contrast to time-of-flight detection schemes, where the corresponding probability is often considerably less than one. Thus, to analyze quantitatively a material by time-of-flight spectrometry, it is necessary to understand the variation of the spectrometer's response with respect to the parameters of the particle which enters it. Previous studies have suggested that time-of-flight spectrometer efficiencies for hydrogen [6], oxygen, and silicon [7] are proportional to the electronic stopping powers of these ions. Additional experiments have shown that the efficiency differs substantially as a function of recoil mass [8]. Overall spectrometer efficiency also appears to depend sensitively upon experimental conditions. For example, reported values for hydrogen efficiency over similar energy ranges vary from 2 to 90% [6]. These results suggest that all of the physical processes governing spectrometer response have not been fully elucidated.

In this paper, we report the results of a comparative study of the efficiencies of two time-of-flight spectrometers used for backscattering and forward recoil analyses at medium energies. Efficiencies have been measured for hydrogen, helium, and carbon projectiles in the energy range 50–275 keV. Two processes which clearly contribute to the efficiency of a spectrometer are secondary electron emission and multiple scattering, both of which occur as ions pass through the carbon start foil. The number of secondary electrons controls the probability that a projectile generates a start event, while multiple scattering deflects some

* Corresponding author, tel. +1 615 343 7225, fax +1 615 343 7263, e-mail weller @ vuse.vanderbilt.edu.

SSDI 0168-583X(93)E0584-4

projectiles out of the acceptance angle of the stop detector.

Efficiency curves have been calculated using a simple model based upon secondary electron emission and multiple scattering which assumes, in addition, that the response of the microchannel plate which generates the stop pulse is independent of a projectile's velocity. Reasonable agreement between the data and the model calculations has been obtained in all cases, leading to the conclusion that, in the future, it will be possible to establish experimentally a single number characterizing a spectrometer's quantum efficiency. The variation of the efficiency with projectile species and energy will then be predictable using an appropriately detailed mathematical model based upon the detector's design.

2. Experimental

The time-of-flight spectrometer and scattering geometry are shown in Fig. 1. Many of the details of the spectrometer's operation are described elsewhere [9], but parameters which are necessary to understand the efficiency and to construct a theoretical model are identified here. Galileo ElectroOptics, Inc., FTD-2003 microchannel plate assemblies 2.5 cm in diameter are used for the start and stop detectors. The detectors, whose active areas are about 50% of their geometric areas, were operated at a bias of -2000 V. Both the forward recoil system (at 42°) and the backscattering system (at 150°) incorporate 2.5 ± 0.5 $\mu g/cm^2$ carbon start foils tilted at 30° with respect to the spectrometer axis for an effective multiple scattering thicknesses of approximately 3 $\mu g/cm^2$. The flight path from the start foil to the stop detector is 37 cm in each case. Under these conditions, the acceptance half angle of the stop detector for multiply scattered ions is approximately 2°. The geometric solid angles subtended by the spectrometers are fixed by entrance apertures at 1.5×10^{-4} and 7.7×10^{-4} sr for the 42° and 150° systems, respectively. Constant fraction discriminators with input sections specially engineered to be compatible with unamplified microchannel plate pulses were used in the spectrometer oriented at 150°. The spectrometer at 42° used conventional constant fraction discriminators which required amplified pulses.

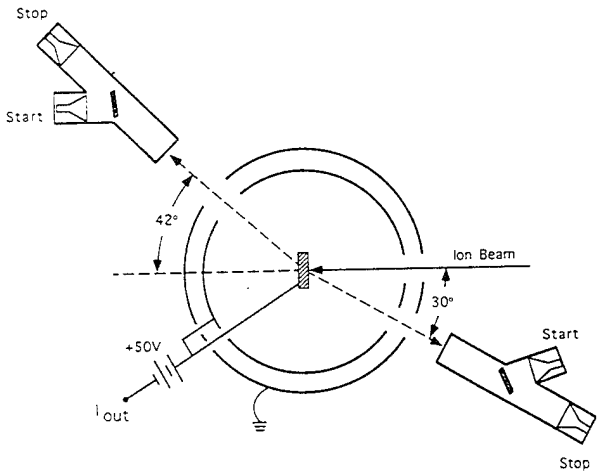

Fig. 1. Schematic of the spectrometer layout, including scattering geometry and biasing of the Faraday enclosure.

To calibrate the detectors, hydrogen and helium ions with energies from 50 to 275 keV and carbon ions from 100 to 400 keV were backscattered from a silicon sample having a nominal gold coverage of $(1.0 \pm 0.1) \times 10^{15}$ atoms/cm^2. Typical doses at each sampled energy were 1.25×10^{13} ions for H and He, and 6.25×10^{12} ions for C. The beam spot size was ~ 10 mm^2. The sample was reanalyzed after calibration runs by 275 keV He backscattering to check for any sputter removal of Au. As an additional control, 275 keV He backscattering spectra were obtained from a quartz sample lightly coated with colloidal carbon to reduce charging. The heights of the silicon edges in these spectra were compared to verify consistency throughout the experiment.

In the forward scattering experiments, a self-supporting carbon foil was mounted on a stainless steel support with a 6.4 mm diameter hole. A thickness of $3.6 \pm 0.5 \times 10^{17}$ atoms/cm^2 was derived from both aerial density and energy loss measurements by He backscattering. H and He ions from 50 to 275 keV were forward scattered at 42° using roughly the same doses as the backscattering experiments. Carbon recoils were generated by Ar ions with energies from 125 to 825 keV and doses of 6.25×10^{11} ions at each sampled energy. No measurable change in the foil thickness was observed by He backscattering as a result of the Ar irradiations.

A double-walled, stainless steel Faraday cylinder was used to obtain consistent beam current measurements under the variety of bombardment conditions used in the experiment. Current was summed and integrated from the target and the inner wall of the cylinder, which were electrically connected and biased at +50 V relative to the grounded outer wall. The outer wall shielded the target from stray electrons and ions generated by the ion pumps and vacuum gauge.

3. Results and discussion

Fig. 2 shows the spectrometer efficiency data, expressed as the ratio of effective solid angle to the geometric solid angle subtended by the detectors. The effective solid angle was derived for H, He, and C at each energy based on known values for the number of

gold or carbon scattering centers/cm^2, the Lenz–Jensen scattering or recoil cross section, the number of incident ions, and the measured number of counts in the forward or backscattering peak. The energies at which projectiles entered the detectors were computed using the appropriate kinematic factors with energy loss in the scattering foil taken into account in the forward scattering configuration.

Error estimates equal to $\pm 10\%$ of measured efficiencies reflect uncertainties in the number of scattering centers/cm^2 and counting statistics. The 42° and 150° spectrometer efficiencies differ by approximately a factor of 2 for each species, as is indicated by the use of differing scales on the left and right axes. We attribute this difference to varying discriminator thresholds and microchannel plate gains in the two systems. The important point to note is that in each case the data are brought into excellent agreement by a single overall normalization. The solid curves in Figs. 2 are the results of the model calculations described below.

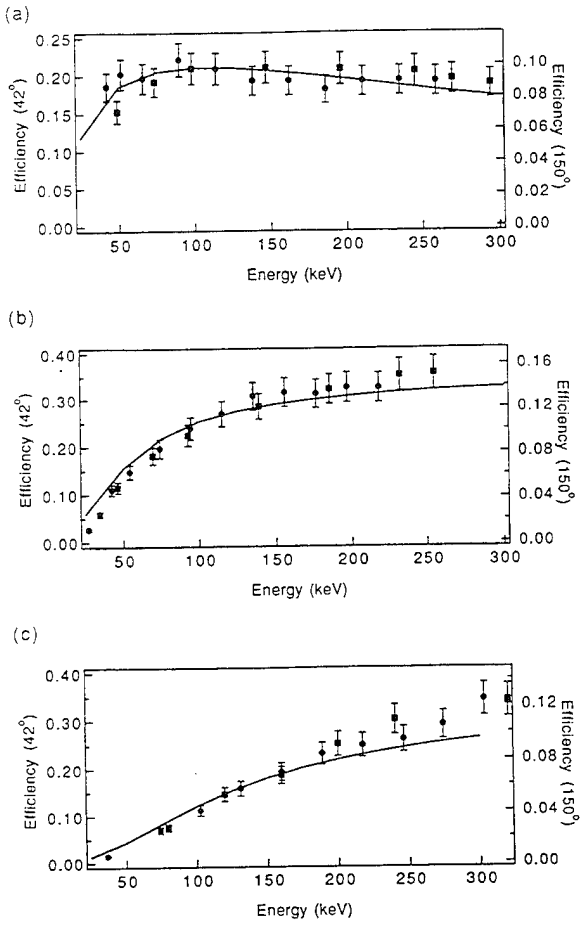

Fig. 2. Data for the 42° (circles) and 150° (squares) spectrometers and normalized theoretical efficiency curves, plotted as a function of energy for (a) hydrogen, (b) helium and (c) carbon.

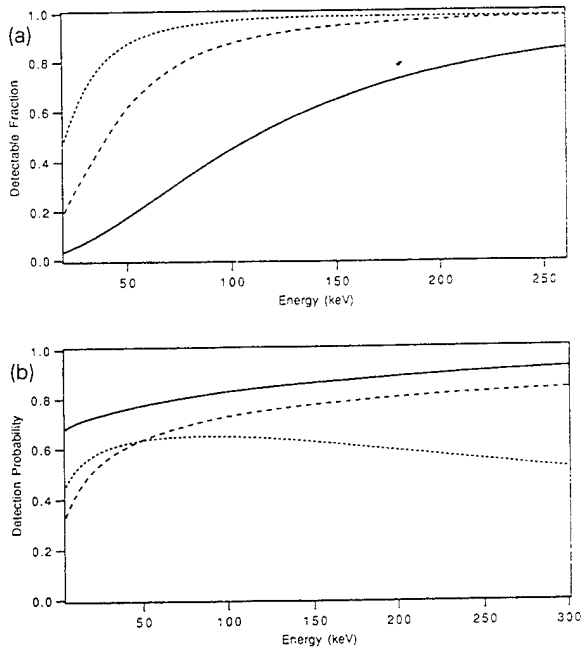

Fig. 3. Theoretical multiple scattering (a) and secondary electron emission (b) contributions to spectrometer efficiency for hydrogen (short dashed), helium (long dashed) and carbon (solid line).

Multiple scattering in the carbon start foil deflects some projectiles enough that they can no longer strike the stop detector. In order to estimate the number of projectiles which are thus lost, we have made ab initio calculations of the multiple scattering distribution functions for H, He and C ions passing through the start foils using the basic equations described in refs. [10,11]. Distribution functions were computed at increments of 25 keV in the energy range corresponding to the measurement using the Lenz-Jensen scattering cross section. These angular distributions were numerically integrated over the solid angle subtended by a 2° cone to give the fraction of multiply scattered ions falling within the acceptance half-angle of the stop detector. The results of the calculation are shown in Fig. 3a as the fraction of ions of each species expected to reach the stop detector as a function of energy.

In his pioneering work on secondary electron emission, Sternglass [12] demonstrated that the yield γ of secondary electrons per incident ion is proportional to the electronic stopping cross section of the ion s_e in the vicinity of the emitting surface ($\gamma = \Lambda s_e$). Constants of proportionality Λ appropriate to various ions exiting C foils have been reported by Rothard et al. [13]. When the stopping cross section is expressed in units

of 10^{-15} eV cm^2, the values of A are 0.25, 0.175, and 0.125 in units of 10^{15}/(eV cm^2) for H, He, and C, respectively. Since, in principle, only one secondary electron is needed to trigger the start microchannel plate, the probability p that a pulse is generated by the arrival of γ secondary electrons is $p = 1 - e^{-\lambda\gamma}$, where λ is the probability that a single electron will trigger an event. Fig. 3b shows this probability as a function of energy for each species. We have used a conservatively small estimate of $\lambda = 0.3$ based upon the work of Fraser [14] and the data which he cites. (Larger values of λ cause the curves in Fig. 3b to increase more rapidly.) The stopping cross sections were computed by the methods described in ref. [15].

The solid curves shown in Fig. 2 were computed by taking the product of the multiple scattering function from Fig. 3a and the secondary electron function from Fig. 3b appropriate to each species and computing a normalization for each detector system by a least squares fit to the data. Only those points with energies greater than 50 keV were used since, in this simple model, the response of the stop microchannel plate was ignored. The ratio of the normalization constants for the 42° and 150° spectrometers were used to set the range of the right-hand scales in Fig. 2. For the 42° detector, the normalization constants for H, He and C were respectively: 0.34 ± 0.03, 0.40 ± 0.03 and 0.32 ± 0.04. Similarly, for the 150° detector the values were: 0.16 ± 0.04,. 0.17 ± 0.04 and 0.12 ± 0.04. Note that for each spectrometer, there is a reasonable probability that the three constants are, in fact, equal. The probability that χ^2 would be larger for normally distributed statistical variations is 22% and 63% respectively.

In agreement with the previously cited experiments, our measured detection efficiency for hydrogen is smaller than for He and C. From Fig. 3b, this can be attributed to the secondary electron contribution to efficiency, even though for hydrogen this quantity reaches a maximum in the energy range studied. Note also that for small λ or γ, the efficiency is simply proportional to the stopping cross section. Multiple scattering, on the other hand, tends to dominate the behavior of the carbon efficiency curve, especially at lower energies where broadening of the angular distribution causes significant losses in the number of particles striking the stop detector.

The ability of this simple model to properly and consistently predict the spectrometer response for the various masses and energies is persuasive evidence that multiple scattering and secondary electron emission are the primary physical processes governing spectrometer performance. A more complete theory will necessarily include a mass and energy dependent stop detector response. Let us emphasize again, however, that to within statistical uncertainty, only one normalization factor is needed for each spectrometer in order to bring the theoretical curves into reasonable agreement with the data for all of the projectile species which were studied.

4. Conclusion

The efficiencies of two similar carbon-foil-based time-of-flight spectrometers have been studied as a function of energy from 50 to 275 keV for H, He, and C at 42° and 150° scattering angles. Within the experimental uncertainties, the efficiency of each detector can be characterized by a single measured number with the variation in efficiency with energy and mass of the analyzed particle being given by a model based upon secondary electron emission and multiple scattering. This result indicates that efficiencies may be estimated for a variety of time-of-flight spectrometer configurations over a wide range of masses and energies by considering parameters such as foil thickness, flight path length, and individual microchannel plate quantum efficiencies. A detailed discussion of the mathematical model of the spectrometer and its range of application, including the effects of variation of parameters such as λ and of additional assumptions about the response of the stop detector, will be the subject of a forthcoming paper.

Acknowledgements

This work was supported in part by the U.S. Army Research Office under contract DAAL 03-92-G-0037. We are grateful to J.M. Anthony and J.A. Keenan, Texas Instruments Inc., for their assistance in the design and manufacture of our Faraday cylinder and to Martha Riherd Weller for helpful comments on the manuscript.

References

[1] J. Sokolov, M.H. Rafailovich, R.A.L. Jones and E.J. Kramer, Appl. Phys. Lett. 54 (1989) 590.
[2] H.J. Whitlow, A.B. Andersson and C.S. Petersson, Nucl. Instr. and Meth. B 36 (1989) 53.
[3] R. Groleau, S.C. Gujrathi and J.P. Martin, Nucl. Instr. and Meth. 218 (1983) 11.
[4] M.H. Mendenhall and R.A. Weller, Nucl. Instr. and Meth. B 47 (1990) 193.
[5] J.H. Arps and R.A. Weller, Nucl. Instr. and Meth. B 79 (1993) 539.
[6] S.C. Gujrathi and S. Bultena, Nucl. Instr. and Meth. B 64 (1992) 789.
[7] H.J. Whitlow, G. Possnert and C.S. Petersson, Nucl. Instr. and Meth. B 37 (1987) 448.

[8] E. Arai, H. Funaki, M. Katayama, Y. Oguri and K. Shimizu, Nucl. Instr. and Meth. B 64 (1992) 296.
[9] M.H. Mendenhall and R.A. Weller, Nucl. Instr. and Meth. B 40/41 (1989) 1239.
[10] H.A. Bethe, Phys. Rev. 89 (1953) 1256.
[11] P. Sigmund and K.B. Winterbon, Nucl. Instr. and Meth. 119 (1974) 541.
[12] E.J. Sternglass, Phys. Rev. 108 (1957) 1.
[13] H. Rothard et al., Phys. Rev. A 41 (1990) 2521.
[14] G.W. Fraser, Nucl. Instr. and Meth. 206 (1983) 445.
[15] J.F. Ziegler, J.P. Biersack and U. Littmark, The Stopping and Range of Ions in Solids (Pergamon, New York, 1985) p. 202.

9. Ion beam analysis of Langmuir-Blodgett films

Nuclear Instruments and Methods in Physics Research B 99 (1995) 623–626

NIM B
Beam Interactions with Materials & Atoms

ELSEVIER

Medium energy ion beam analysis and modification of Langmuir–Blodgett thin films

J.H. Arps [a], R.A. Weller [a,*], Y.S. Tung [b], D.O. Henderson [b]

[a] *Vanderbilt University, Box 1687, Station B, Nashville, TN 37235, USA*
[b] *Fisk University, Nashville, TN 37208, USA*

Abstract

The erosion behavior of cadmium arachidate Langmuir–Blodgett films is studied under 270 keV He and Ar ion irradiation. Initial characterization by medium energy time-of-flight backscattering yields a thickness and stoichiometry consistent with an unmodified film. In addition, time-of-flight elastic recoil detection is used to monitor the hydrogen evolution from the films as a function of the cumulative dose. After a dose of 5×10^{14} Ar ions/cm^2, the film is reduced to less than 50% of its initial thickness and depleted in hydrogen. Smaller losses are measured for He at a dose of nearly 1×10^{15} ions/cm^2. Dramatic changes are observed in the interference color of 50-layer films under ion erosion. Measurements by ellipsometry yield thicknesses which are consistent with the backscattering estimates and indicate an increase in the refractive index of the film. The response of cadmium arachidate to energetic ions is compared with the cadmium salt of ω-tricosenoic acid, which can polymerize due to the presence of a C=C double bond.

1. Introduction

Langmuir–Blodgett (LB) film deposition is a simple method for preparing uniform organic or metallorganic layers of well-defined thickness. Films of these highly oriented molecular chains are built up a monolayer at a time from a wide range of feed materials, many of which exhibit optical or electrical properties of practical interest [1]. LB films of ω-tricosenoic acid, for example, have been considered for use as an electron beam resist [2]. Recently, ion beam and thermal modification of LB films have been investigated for the purpose of generating other useful thin film materials and structures. Schoch et al. implanted 150 keV Ar ions to modify the conductivity of films formed from the octadecylamine salt of a polymeric acid [3]. Thin layers of SiC have also been produced by vacuum pyrolysis of polyimide LB films on silicon [4]. Laursen et al. used a thermal treatment to make thin metal oxide layers from Y-, La-, and Er-arachidate films [5]. In this last case, Rutherford backscattering was applied in the analysis of both modified and pristine LB films. While reasonable estimates of the thickness may be derived from the carbon and incorporated metal ion signals, the authors note the likelihood of beam effects precipitating a loss of hydrogen and destruction of the optical quality of the film.

Medium energy time-of-flight backscattering and forward recoil spectrometry are two complementary techniques well suited for the study of radiation sensitive organic thin films. Simultaneous measurement of hydrogen and carbon concentrations is possible in the forward geometry while the film thickness and distribution of incorporated heavy elements may be determined by backscattering. Both methods take advantage of the improved sensitivity gained from larger cross sections at lower energies to limit the charge deposited on the sample. The total energy deposited in the film by each ion is also reduced, further minimizing beam-induced damage. Thin films of nitrocellulose and aluminized mylar have been successfully analyzed by these methods [6,7].

Langmuir–Blodgett films not only present a challenge for nondestructive evaluation by ion beam analytical techniques, but are also uniquely suited for the study of hydrocarbon bond breaking processes by energetic ions because of their highly ordered, repeating structure. In this paper, we report on the initial characterization of two different 50-layer LB films and their subsequent modification under ion beam irradiation. Cadmium salts of arachidic and ω-tricosenoic acid were exposed to 270 keV He and Ar ions. While both materials are composed of extended CH_2 groups, ω-tricosenoic acid is distinguished by a single C=C double bond in each molecular chain. The presence of this bond appears to influence the removal rate under ion erosion. The interference color of the film is altered by He and Ar irradiation without significant degra-

* Corresponding author.

SSDI 0168-583X(94)00662-8

dation in optical quality. Measurements by ellipsometry indicate not only a reduction in thickness but an increase in refractive index.

2. Experiment

Clean 1-in. silicon wafers were immersed in a 5% HF solution for 2 min and rinsed in deionized water to remove the native oxide and produce a hydrophobic surface. A solution of 5×10^{-4} M $CdCl_2$ in deionized water was prepared in a standard LB deposition trough. Arachidic acid (CH_3–$(CH_2)_{18}$–CO_2H) dissolved in chloroform was spread onto the surface and the film deposited a layer at a time by repeated immersion and withdrawal of the sample. The deposition pressure and speed were fixed at 42 mN/m and 15 mm/min, respectively. The pH of the subphase was 5.5, with the films expected to be composed of roughly equal amounts of the cadmium salt and unterminated acid. Similar deposition conditions were maintained for ω-tricosenoic acid (CH_2=CH–$(CH_2)_{20}$–CO_2H). A lower Cd concentration was used, however, in order to generate a more stable, better flowing film. The estimated thicknesses of the 50-layer arachidate and ω-tricosenoate films were 124 nm and 138 nm, respectively, based on known values for the thickness of single layers.

The samples were placed in a vacuum chamber with a nominal base pressure of 10^{-8} Torr. He^+ and Ar^+ ions accelerated to 270 keV were directed at normal incidence to the samples at a total fluence of 1×10^{15} and 5×10^{14} ions/cm^2, respectively. The beams were rastered over an area of approximately 0.5 cm^2 with current densities in the range 0.02–0.07 μA/cm^2. Uniform deposition of energy throughout the films was expected since the mean projected ranges of the ions greatly exceeded the thicknesses. At predetermined intervals, the exposures were interrupted and time-of-flight elastic recoil detection was used to measure the hydrogen and carbon composition of the film. A beam of 810 keV Ar^{3+} ions was directed at an angle of 21° to the sample surface. Light element recoils from the film, Si atoms from the substrate, and the scattered beam were detected at a 42° forward scattering angle relative to the initial beam direction. The total number of ions needed to obtain each measurement was 1×10^{11}. A 270 keV He^+ beam was also used to characterize the samples by time-of-flight backscattering before and after the irradiations to determine the change in thickness. Scattered particles were detected at 150° with a charge of 3×10^{12} ions applied in the initial analysis and scanned over the same area. An unrastered beam was used on the irradiated areas to limit contributions due to edge effects. Complete descriptions of the medium energy time-of-flight forward recoil and backscattering techniques are given elsewhere [8,9].

After the samples were removed from vacuum, the thickness and refractive index of the pristine and irradiated LB films were determined by optical ellipsometry. A light source was filtered to isolate the 546.1 nm line and directed at a 70° angle of incidence. A Rudolf Type 436 null ellipsometer was used to measure the Δ and Ψ ellipsometry angles. The thickness and refractive index were then determined using an iterative computer program based on algorithms developed by McCrackin [10]. An absorption coefficient of zero was assumed for the calculations [11].

3. Results and discussion

Time-of-flight forward recoil spectra for pristine, He-, and Ar-eroded cadmium arachidate thin films are shown in Fig. 1. Although the recoil energies determined by collision kinematics are usually larger for high-mass recoils, light-atom recoils have the greater velocity and are well separated from events attributable to the scattered beam in the time-of-flight spectrum. Recoil H and C are clearly distinguished, as well as scattered Ar from Cd in the film and the Si substrate. Initially, the film is too thick for recoils or scatters from the substrate to escape, hence the appearance of such features is an obvious indication of film erosion.

The concentration ratio of the hydrogen to carbon is determined from the recoil step heights transformed from the time to energy domain

$$H/C = \frac{Y_H}{Y_C}\frac{\sigma_C}{\sigma_H}\frac{\eta_C}{\eta_H}\frac{S_H}{S_C}, \qquad (1)$$

where $Y_{H,C}$ are the yields at the respective surface energies, $\sigma_{H,C}$ the Lenz–Jensen recoil cross sections, and $\eta_{H,C}$ are the calibrated detection efficiencies for H and C. The final terms $S_{H,C}$ are the energy loss factors for H and C in the film, the ratio of which is generally insensitive to changes in composition. Figs. 2a and 2b show the change in the H/C ratio with dose for He and Ar irradiation of the two materials. Error bars (±10%) reflect uncertainties in

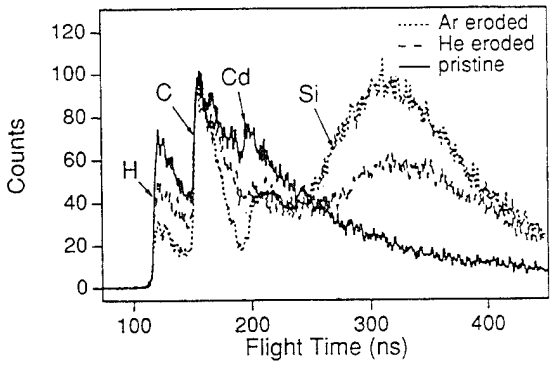

Fig. 1. TOF spectra for 810 keV Ar^{3+} on pristine, He and Ar eroded cadmium arachidate film. A total dose of 1×10^{11} ions was deposited during the analysis.

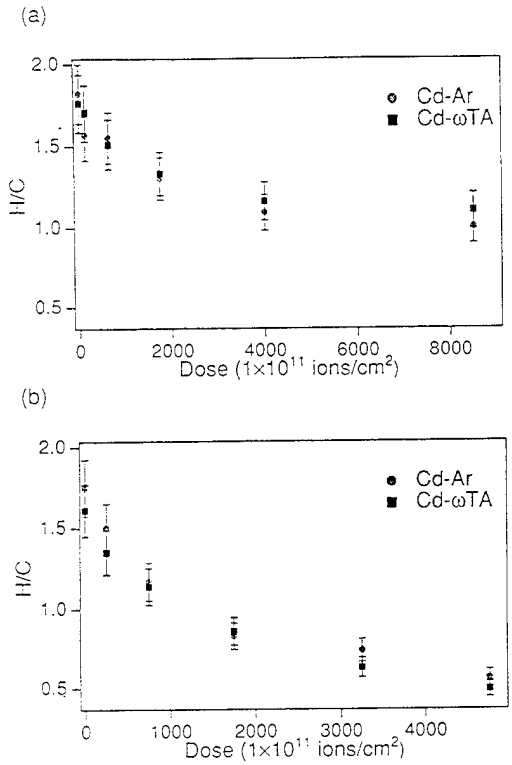

Fig. 2. Change in the ratio of hydrogen to carbon concentration with dose for cadmium arachidate and ω-tricosenoate films for (a) 270 keV He^+ and (b) 270 keV Ar^+ irradiation.

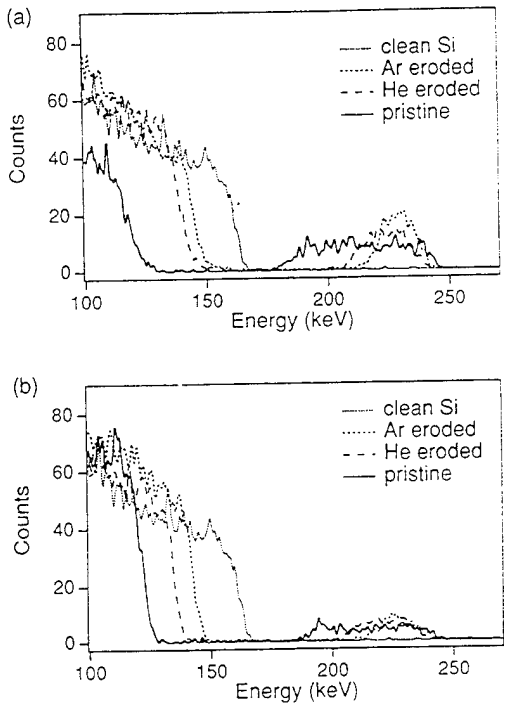

Fig. 3. Transformed energy spectra for 270 keV He backscattering for pristine, He and Ar eroded (a) cadmium arachidate and (b) cadmium ω-tricosenoate films normalized to a charge of 6×10^{12} ions. A spectrum for a clean Si wafer is shown for reference.

the detection efficiency and Poisson statistics in the measurement of the step height. Initial ratios are generally consistent with unmodified films. No significant differences are observed in the evolution of the stoichiometry for Cd-arachidate or ω-tricosenoate. As can be seen, hydrogen is rapidly depleted from the films under Ar exposure, with a measurable decrease under He irradiation. Estimates of the energy loss suggest that the density of deposited energy in the materials is a factor of 3 greater for Ar than He. An attempt to identify either the electronic or nuclear energy loss as the primary factor contributing to dehydrogenation is unrealistic within the limited set of data presented.

Medium energy backscattering spectra, transformed from time-of-flight to energy, are shown for the pristine and altered films in Figs. 3a and 3b. The film thickness was determined from the buried silicon edge position or the width of the cadmium feature fitted to error functions. Integration of the reciprocal energy loss along the inward and outward paths yields

$$x = \cos\,\theta_1 \int_{E_1}^{E_0} S(E)^{-1}\,\mathrm{d}E = \cos\,\theta_2 \int_{E_2}^{KE_1} S(E)^{-1}\,\mathrm{d}E, \tag{2}$$

where E_0 and E_2 are the incident and exit energies, $S(E)$ the stopping cross section, and θ_1 and θ_2 the incident and exit angles measured from the target normal. A numerical

Table 1
Results of forward recoil, backscattering, and ellipsometry measurements

Sample	Backscattering thickness [nm]	Ellipsometry thickness [nm]	H/C ratio	Refractive index
Cd-arachidate	123 ± 2	129 ± 4	1.8 ± 0.2	1.51 ± 0.05
He eroded	62 ± 1	71 ± 2	1.0 ± 0.1	1.66 ± 0.05
Ar eroded	46 ± 1	47 ± 1	0.56 ± 0.06	1.81 ± 0.05
Cd-tricosenoate	110 ± 2	117 ± 4	1.7 ± 0.2	1.52 ± 0.05
He eroded	71 ± 1	78 ± 2	1.1 ± 0.1	1.71 ± 0.05
Ar eroded	54 ± 1	51 ± 1	0.49 ± 0.05	1.88 ± 0.06

integration and root finding procedure was used to find the energy before scattering E_1 and the thickness x in atoms/cm^2. Based on the arachidate stoichiometry, an areal density of 5.2×10^{14} molecules/cm^2/layer was calculated for the pristine 50-layer film, in excellent agreement with previous measurements of 1.8×10^{-15} cm^2 for the molecular area [12]. It is important to note that a 10% reduction in the hydrogen content would generate a measurable 2 keV shift in the position of the silicon edge. An areal density for Cd of $(7.0 \pm 0.7) \times 10^{15}$ atoms/cm^2 was derived from the integrated yield and is consistent with a prediction of 6.9×10^{15} atoms/cm^2 for a 50/50 acid/salt film.

Comparison of spectra for the pristine and exposed areas clearly indicates shrinkage of the films under ion irradiation. The residue thicknesses were estimated from Eq. (2) by approximating the film composition as CH_x with the relative hydrogen content determined by forward recoil spectrometry. A fixed value of 1.1 g/cm^3 was assumed for the film density. Only the Si edges were used because of the smaller statistical uncertainty in fitting the positions. The results, including estimates for the pristine films by this method, are compiled in Table 1. The quoted errors are derived from uncertainties in fitting the Si edge positions. The smaller initial thickness for the ω-tricosenoate film is difficult to explain, though this must clearly be the case as the Si edge is higher in energy and the Cd width narrower relative to the arachidate features. A difference in the number of layers transferred during deposition or a slight thinning during the initial analysis may be responsible. However, the thickness of the residues is 15–20% larger for the ω-tricosenoate samples. A reasonable explanation might be that ω-tricosenoate, due to the presence of the C=C double bond, polymerizes under ion exposure to form radiation-hard structures.

Visual inspection of the pristine and exposed areas of the samples reveals a striking change in the color of the reflected light. Both types of 50-layer samples ($n = 1.5$) appear blue initially but turn a dark blue or magenta under He irradiation and yellow after Ar irradiation with no qualitative reduction in the optical integrity. Ellipsometry measurements, also given in Table 1, allow for determination of the refractive index and provide a check of the backscattering thickness. Comparison of the two methods yields an agreement of better than 10%, implying that the accuracy of stopping power data used in the backscattering calculations is fairly reliable over the energy range considered. Predictions of the interference colors based on ellipsometer values of n and t are consistent with the observed hues. A similar scaling of refractive index with hydrogen content has been observed for plasma-deposited hydrocarbon films [13]. We expect to describe in a future report results from Raman and FTIR spectroscopic studies which demonstrate that the films rapidly become disordered under ion irradiation.

4. Conclusion

Medium energy time-of-flight spectrometry has been successfully applied to the study of cadmium arachidate and ω-tricosenoate Langmuir–Blodgett thin films under ion beam irradiation. Backscattering measurements have correctly determined the thickness of a 50-layer cadmium arachidate film with negligible hydrogen loss. The favorable depth resolution of the technique may ultimately permit us to separate the individual metal domains of a multilayer film by use of lead salts to gain higher sensitivity. Forward recoil spectrometry has been used to measure H/C concentration ratios as a function of ion dose and could be applied to the direct determination of H, C, and O areal densities, if the films are less than a few hundred ångströms. Ion beam modification of the thickness and refractive index has produced a uniform change in the interference color that might, with further study, be shown to have potential use as a composite structure for optical wave guides or interference gratings.

Acknowledgements

The authors are very grateful to Dr. Frank Grunfeld of NIMA Technology Ltd. for preparation of the LB films. This work was supported in part by the U.S. Army Research Office under contract DAAL 03-92-G-0037.

References

[1] A. Ulman, An Introduction to Organic Films, (Plenum, New York, 1990).
[2] A. Barraud, C. Rosilio and A. Ruadel-Trixier, Solid State Technol. 22 (1979) 120.
[3] K.F. Schoch, W.F.A. Su and J. Bartko, 4th Int. SAMPE Electronics Conf. 4 (1990) 334.
[4] B. Yang et al., Appl. Phys. Lett. 64 (1994) 1445.
[5] T. Laursen, G.R. Palmer, D.T. Amm and D. Johnson, Nucl. Instr. and Meth. B 82 (1993) 125.
[6] J.H. Arps and R.A. Weller, in: Nondestructive Characterization of Materials VI, eds. R.E. Green et al., (Plenum, New York, 1994) p. 781.
[7] J.H. Arps and R.A. Weller, Nucl. Instr. and Meth. B (1995) in press.
[8] J.H. Arps and R.A. Weller, Nucl. Instr. Meth. B 79 (1993) 539.
[9] M.H. Mendenhall and R.A. Weller, Nucl. Instr. and Meth. B 47 (1990) 193.
[10] F.L. McCrackin, NBS Technical Note #479 (1969).
[11] R.W. Collins and Y.T. Kim, Anal. Chem. 62 (1990) 887A.
[12] S. Garoff, H.W. Deckman, J.H. Dunsmuir and M.S. Alvarez, J. Phys. (Paris) 47 (1986) 701.
[13] P. Reinke, W. Jacob and W. Moller, J. Appl. Phys. 74 (1993) 1354.

10. Sensitivity of medium energy backscattering

Nuclear Instruments and Methods in Physics Research B 99 (1995) 491–494

NIM B
Beam Interactions with Materials & Atoms

ELSEVIER

The impact of spectrometer efficiency on the trace-element sensitivity of time-of-flight medium energy backscattering

Robert A. Weller *

Vanderbilt University, Nashville, Tennessee 37235, USA

Abstract

The intrinsic efficiency of a time-of-flight spectrometer which derives timing information from the passage of an ion through a carbon foil is governed primarily by secondary electron emission and multiple scattering in the foil and by the intrinsic responses of the detectors which generate the time markers. For all ions except hydrogen, the efficiency is a monotonically increasing function of energy in the range up to a few hundred keV used for medium energy backscattering. Combining expressions for spectrometer efficiency and trace element sensitivity obtained previously, we show that for a given ion the product of scattering cross section and spectrometer efficiency determines an optimum energy for trace element analysis by backscattering. The optimum choice of ion is a function of the mass of the trace element under investigation. If the limit of sensitivity is determined by sputtering, then light elements such as He appear to be unconditionally superior to heavy projectiles such as C or N. However, the numerical value of the limiting sensitivity for a given trace element is strongly influenced by the details of the sputtering and the degree of beam induced mixing at the surface. For elements in the region of Fe to Cu reasonable assumptions about sputtering lead to the conclusion that sensitivities of about 3×10^{10} cm^{-2} are achievable using 100 keV He^+ projectiles and a spectrometer which subtends a solid angle of 1 msr.

1. Introduction

One of the most promising applications of medium energy backscattering is in the detection of trace elements particularly on silicon where minute amounts of transition metal contaminants can cause device failure. The general trend of the scattering cross section, typified by the Rutherford case where $\sigma \propto z_1^2/E^2$, where z_1 is the atomic number of the projectile and E its energy, seems to indicate that heavy ions at low energies should provide the greatest sensitivity for trace element detection [1]. However, this assumes that the detector of backscattered particles is equally sensitive to ions of all masses and energies. When a surface barrier detector is being used, this is a reasonably accurate assumption, provided the energies are high enough. For time-of-flight spectrometers, however, there is a species and velocity dependent efficiency which cannot be ignored.

In this paper, we will consider the behavior of time-of-flight spectrometers which derive their timing information from the interval between the detection of secondary electrons emitted as a particle passes through a thin carbon foil, and the particle's subsequent impact on a microchannel plate [2]. The efficiency of such a spectrometer is determined primarily by secondary electron emission and multiple scattering in the foil and by the intrinsic efficiencies of microchannel plates for detecting electrons and heavy particles [3]. In the expression for the yield of backscattered particles, the spectrometer's efficiency and scattering cross section may be grouped together to form a single, energy dependent effective cross section which, for most ions which are candidates to use in backscattering, has a maximum in the range of a few hundred keV.

In this publication, we will explore the behavior of the effective cross section and its implications for the minimum measurable areal densities of various elements. Before presenting the results of these computations, we will briefly describe the spectrometer efficiency model and sputtering-limited sensitivity model which have been used to obtain them.

2. Computational method

The backscattering yield Y from a dispersed layer of atoms with areal density ρ is given in terms of the differential scattering cross section σ, and number N of incident particles by

$$Y = N\rho\sigma\Omega\eta, \tag{1}$$

* Tel. +1 615 343 7225, fax +1 615 343 7263, e-mail weller@vuse.vanderbilt.edu.

SSDI 0168-583X(94)00578-8

where Ω is the solid angle subtended by the detector and η is the intrinsic efficiency for detecting a backscattered particle. Since for a time-of-flight spectrometer both σ and η are dependent upon energy, it is reasonable to group them together into a single effective cross section $\sigma(E)\eta(KE)$, where E is the beam energy and K the kinematic factor associated with the collision. The quantity $\sigma\eta$ is a figure of merit for trace element sensitivity since, when it is large, a relatively lower density ρ of target atoms will produce a statistically significant backscattering yield.

The intrinsic efficiency of time-of-flight spectrometers has recently been the subject of both experiments and mathematical modeling in our laboratory [3,4]. We have found good agreement with measurements using the following expression:

$$\eta = ATf\left(1 - e^{-\lambda \Lambda S_c}\right)\left(1 - e^{-\gamma\left(1 - e^{-\gamma_s\left(1 - e^{-\gamma_s(\cdots)}\right)}\right)}\right), \qquad (2)$$

where γ is the secondary electron yield of ions striking the stop detector, γ_s is the mean secondary electron yield of electrons in the channels of the stop detector, and g is defined by:

$$\gamma\left(1 - e^{-\gamma_s(\cdots)}\right) \equiv g\Lambda_n S_{MCP}. \qquad (3)$$

Here A is the open area of a microchannel plate; T is the transmission of all meshes along the trajectory of an ion in the spectrometer; f is the energy dependent fraction of particles which fall within the active area of the stop detector after being multiply scattered by the carbon start foil [5]; ΛS_c is the secondary electron yield of the start foil; λ is the probability that a secondary electron will trigger the start detector; and finally, $g\Lambda_n \cdot S_{MCP}$ is a term representing the response of the stop detector to ions. Each of the terms S_c, S_{MCP}, and f, representing (respectively) the stopping power of the ion in the start foil, the stopping power in the stop microchannel plate surface, and multiple scattering in the start foil, are strongly energy dependent for ions in the range up to a few hundred keV. As a result, the efficiency is small for low energy ions and, at a given energy, decreases with increasing atomic number because of the dominant effect of the multiple scattering term. In the curves presented below, η has been computed with parameter values described in Ref. [3], with the only exception being that a value of Λ was used for heavy ions which matches most closely the observed performance of our backscattering spectrometer rather than a compromise between our backscattering and forward scattering spectrometers.

In order to estimate the minimum measurable areal density of a surface layer, it is necessary to place some limits on the experimental conditions. From a practical point of view, time must certainly play a role as do other considerations such as background in the region of interest, multiple scattering in the target and the sputter removal of the layer by the beam being used to analyze it. In Ref. [2] we established an expression for the minimum areal density which can be measured with fractional uncertainty ε in the presence of background B from all sources including multiple scattering in the substrate and random coincidences associated with count rate. The criterion used was that the fractional statistical uncertainty of the measurement equals the fraction of material removed by sputtering. The resulting expression is:

$$\rho = \frac{1 + \sqrt{1 + 4\varepsilon^2 B}}{2\varepsilon^3} \frac{Y_s}{\rho_s A_s \Omega(\sigma\eta)}. \qquad (4)$$

Here A_s is the area of the target which is irradiated by the beam. This expression is based upon the assumption that the probability P that a beam ion removes a target atom is related to the sputtering yield of the substrate Y_s through the relation,

$$P \approx Y_s \frac{\rho}{\rho_s}, \qquad (5)$$

where ρ_s is interpreted as the areal density of substrate atoms in the region from which sputtered particles are drawn. Eq. (5) expresses the assumption that trace elements are sputtered randomly from the surface with a probability equal to their fractional representation in the volume from which sputtered particles can emerge. As described below, this assumption is probably too conservative.

Expression (4) describes a more general limit than simple detectability which without specific definition is not a precise concept. In the computations presented below, a minimally detectable ρ_{min} will be taken to be one for which $\varepsilon = 0.3$, which may be viewed as a non-zero signal with a confidence level of approximately three standard deviations. It is also assumed that $B = 0$. The result for $B \neq 0$ (or a different ε) can be obtained by scaling the graphs below by the leading factor in Eq. (4).

3. Results

Figs. 1 and 2 show, as a function of energy, the effective cross section for a number of ions incident on Cu

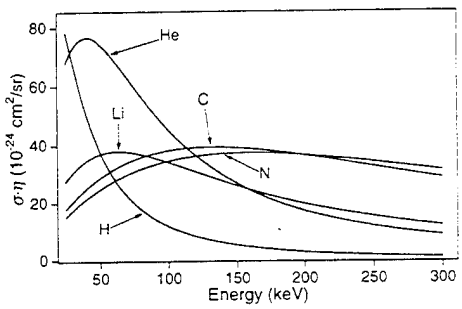

Fig. 1. The effective cross section for various ions scattering from Cu as a function of incident projectile energy. The scattering angle is 150°.

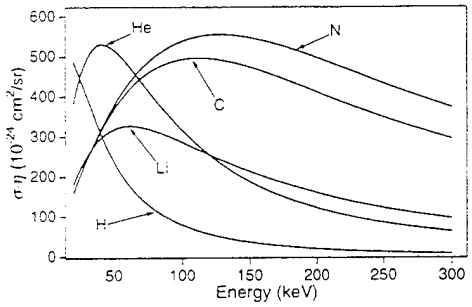

Fig. 2. The effective cross section for various ions scattering from Au as a function of incident projectile energy. The scattering angle is 150°.

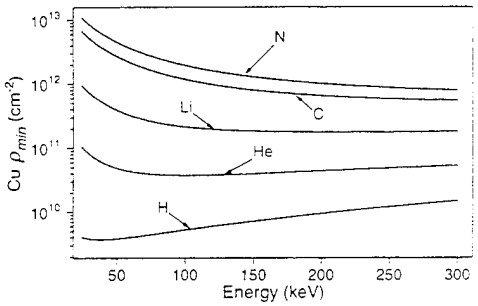

Fig. 4. The sputtering-limited minimum detectable areal density ρ_{min} of Cu on Si as a function of beam energy for various projectiles. The geometric solid angle subtended by the spectrometer is assumed to be 0.8 msr.

and Au. The cross section σ is taken to be the Lenz–Jensen [6] screened cross section and is computed without approximation using methods similar to those described in Ref. [7]. The efficiency η is computed as described above. For all ions except H, the combination of screening and spectrometer efficiency is adequate to produce a maximum in the effective cross section. Perhaps most surprisingly, for detecting Cu, helium achieves greater sensitivity than heavy ions up to an energy somewhat larger than 100 keV. It is important to note that this is on a projectile-for-projectile basis and does not yet take account of the greater sputtering of the heavy ions. For Au, on the other hand, a nitrogen beam in the range of 125 keV would be preferred according to Fig. 2. These figures indicate that lithium offers no particular advantage in either case, at least so far as effective cross section is concerned.

Fig. 3 shows the energy at which $\sigma\eta$ is maximum for He and N beams as a function of the atomic number z_2 of the target element. For He this energy is remarkably constant and near 40 keV for most elements in the periodic table. For N it varies more strongly at lower masses where the backscattered energy (and therefore the efficiency) is low but remains near 130 keV for a wide range of elements.

Taken together, Figs. 1–3 offer a surprising insight. Picking a convenient energy of, say, 100 keV we see that effective cross section is simply not a very important criterion to use in selecting a beam for maximum sensitivity trace element analysis by time-of-flight backscattering. For beams from He through N, the effective cross section varies by only about 50% thoughout the periodic table. Thus, we must look to other effects such as desired mass resolution or the limitations imposed by sputtering when selecting a beam.

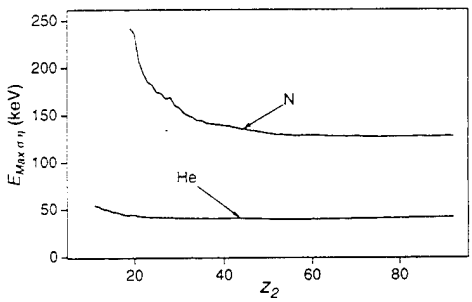

Fig. 3. The energy at which the effective cross section is maximum for He and N projectiles scattering at 150° as a function of the atomic number of the target particle.

In Fig. 4 we add the effects of sputtering and show ρ_{min} from Eq. (4) for Cu on Si as a function of beam energy for various beams from H to N. The estimate is based upon the solid angle subtended by our spectrometer, 0.8 msr, and assumes a beam area on target of 0.03 cm^2. The sputtering yield of Si was computed using the expression of Matsunami et al. [8] and ρ_s was taken to be 4×10^{15} cm^{-2}, corresponding to about 3 atomic layers of Si. When sputtering is taken as the limiting process, light ions are seen to have dramatically greater potential for high sensitivity than heavy ions. However, the choice may not be as straightforward as Fig. 4 would seem to imply. Two issues must be considered, run time and the appropriateness of the sputtering model described by eq. (5). Of the former, one predicts that it should take approximately an order of magnitude (about 10^{16} versus about 10^{15}) more He than N ions to make the measurement. Since it is not possible to compensate by running larger currents without incurring much increased background [2], the measurement with He must be assumed to take ten times longer. The issue of the correctness of the sputtering model is much more subtle.

Initially, if the trace element layer is dispersed and truly surface correlated, then the assumption described above is reasonable, except possibly in cases where a large mismatch in atomic mass between the substrate and trace constituents leads to poor transfer of energy between the two. However, as the analysis proceeds, the target atoms are not only sputtered but also mixed relatively deeply into the substrate where a significant number may be effectively eliminated as candidates to sputter but not to backscatter. Since heavy ions are expected to mix the surface more efficiently than lighter ones, the apparent

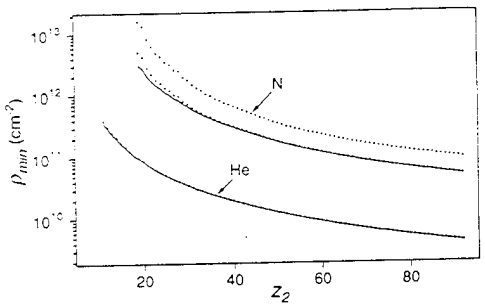

Fig. 5. Minimum detectable areal densities of trace elements using He and N beams as a function of the atomic number of the trace constituent. Solid curves represent measurement with the best beam energy. Dotted curves are for fixed beam energies of 100 keV (upper dotted curve) and 300 keV (lower dotted curve) for N, and 100 keV for He. The spectrometer solid angle is 0.8 msr.

advantage of light atoms derived by their lower sputtering rate may be diminished, at least for runs of constant duration. However, as the effective cross section graph shows, at least for the case of 100 keV He and N being used to measure Cu, it is never completely eliminated on an atom-for-atom basis. We conclude that, because of these considerations, the estimates given here should be regarded as conservative and that lower values of ρ_{min} may be achieved if sputtering of the trace layer proceeds (for any reason) more slowly than estimated by Eq. (5).

Fig. 5 summarizes ρ_{min} as a function of the atomic number of the target for analyses using N (upper group of curves) and He (lower curve) projectiles. The solid curves are obtained by using the best energy for each ion–target system, determined to be that energy for which the absolute minimum ρ_{min} is obtained. For the analysis of copper, these correspond to the minima of the curves in Fig. 4. Also shown are three dotted curves. The upper dotted curve is for analysis with N at a fixed beam energy of 100 keV. Fixed-energy analysis is almost indistinguishable from best-energy analysis for He and N at 100 keV and 300 keV, respectively, as shown by the remaining dotted curves.

4. Conclusion

Using a newly derived expression for time-of-flight spectrometer efficiency which has been shown to be in good agreement with experimental observations, we have revisited the problem of estimating the ultimate sensitivity of trace element analysis by medium energy backscattering with the objective of gaining insights which might be useful in selecting effective experimental conditions. We find that the apparent advantage of heavy ions at low energies is less dramatic or even absent when screening of collisions and spectrometer efficiency are considered, and that the dominant roles of sputtering and spectral background, such as that caused by multiple scattering in the target, are clearly evident. For general trace element analysis, beams of 100 keV He or of 300 keV N are close to optimum with He being preferred for greatest sensitivity for elements near Cu in the periodic table. Using a spectrometer with characteristics similar to ours, one would expect, in the absence of background, to achieve a ρ_{min} for Cu on Si of about 3×10^{10} cm^{-2} with 1 msr of geometric solid angle. With large-solid-angle detectors, values of ρ_{min} of $< 10^{9}$ cm^{-2} appear possible under optimum conditions. Lower ρ_{min} values for heavy ions than those computed here may result from the use of a sputtering model which properly incorporates the effects of ion beam mixing. Ultimately, the per-incident-ion rate of removal of trace elements on a surface must be settled by experiment. Only then can the sputtering-limited ρ_{min} be established with confidence. In all likelihood, however, below areal densities of 10^{9} cm^{-2}, considerations of background will dominate.

Acknowledgements

This work was supported in part by the U.S. Army Research Office under contract DAAL 03-92-G-0037 and by Sandia National Laboratories under contract AH-3292.

References

[1] J.A. Knapp and J.C. Banks, Nucl. Instr. and Meth. B 79 (1993) 457.
[2] R.A. Weller, Nucl. Instr. and Meth. B 79 (1993) 817.
[3] R.A. Weller, J.H. Arps, D. Pedersen and M.H. Mendenhall, Nucl. Instr. and Meth. A 353 (1994) 579.
[4] J.H. Arps and R.A. Weller, Nucl. Instr. and Meth. B 90 (1994) 547.
[5] M.H. Mendenhall and R.A. Weller, Nucl. Instr. and Meth. B 93 (1994) 5.
[6] P. Loftager, F. Besenbacher, O.S. Jensen and V.S. Sorensen, Phys. Rev. A 20 (1979) 1443.
[7] M.H. Mendenhall and R.A. Weller, Nucl. Instr. and Meth. B 58 (1991) 11.
[8] N. Matsunami, Y. Yamamura, Y. Itikawa, N. Itoh, Y. Kazumata, S. Miyagawa, K. Morita, R. Shimizu and H. Tawara, Atom. Data Nucl. Data Tables 31 (1984) 1.

11. Ion beam analysis of irradiated nitrocellulose films

Nuclear Instruments and Methods in Physics Research B 100 (1995) 331–335

NIM B
Beam Interactions with Materials & Atoms

ELSEVIER

Time-of-flight elastic recoil analysis of ion beam modified nitrocellulose thin films

James H. Arps, Robert A. Weller *

Vanderbilt University, Nashville, Tennessee 37235-1807, USA

Abstract

The erosion properties of nitrocellulose ($C_6H_7N_3O_{11}$) thin films on Si have been studied under exposure to 270 keV H, He, C, and Ar ions. Time-of-flight elastic recoil spectrometry has been applied to determine the atomic composition of the films as a function of deposited charge. All exposed films exhibit an initial removal of N and O consistent with RO–NO_2 bond breaking, proceeding at a rate that appears to depend on the density of electronic excitation. A non-volatile, carbon-rich residue remains after prolonged exposure to H, He, and C ions, while the film is effectively removed under Ar irradiation. Experimental evidence supports the proposition that binary collisions are an important mechanism affecting desorption of the H and C components. The results are consistent with a suggestion that complete volatilization of the film is determined by the nuclear stopping power of the incident ion.

1. Introduction

The response of nitrocellulose to energetic ions is quite unusual. The material volatilizes completely under certain irradiation conditions, otherwise forming a radiation-hard residue. This property, frequently referred to as "self-development", can be practically applied in lithography as a positive resist, or as a negative resist using the residue, to produce structures with lateral dimensions less than 100 nm [1]. Previous workers have attempted to identify the parameters affecting the nitrocellulose etch rate and the conditions under which a residue is formed. Kaneko et al., have reported that both the ion mass and energy play a role in the observed erosion behavior, suggesting a mechanism dependent on the electronic and nuclear energy losses of the ion in the material [2,3]. Mühle and Götz observed an initial etch rate independent of ion mass and found no correlation between the removed thickness and the total deposited ion energy [4]. Moliton et al., report etch rates dependent on the total energy loss with no effects tied to the individual nuclear and electronic losses [5].

A common method for measuring nitrocellulose film evolution has been surface profilometry. Unfortunately, the technique is insensitive to any changes in chemical composition during exposure. The use of a profilometer may also restrict the minimum thickness of films that may be studied. Perhaps because of this, many previous experiments have used films with an initial thickness greater than the projected range of the irradiating ions. Attempts to identify the individual contributions due to electronic or nuclear energy loss are complicated by significant variation in these values along the ion trajectory. Infrared spectroscopy has also been applied to study the evolution of the nitrocellulose chemical structure, and a number of reaction pathways have been suggested [6]. However, it may not be possible to identify the dominant reactions without quantitative information on the film stoichiometry.

In an attempt to further understand the erosion behavior of nitrocellulose, we have applied medium energy time-of-flight elastic recoil detection to the analysis of 270 keV H, He, C, and Ar ion irradiated thin films on silicon. This technique can simultaneously measure in situ the evolution of the individual atomic components in the film as a function of the accumulated dose. Thicknesses less than 20 nm were studied to minimize the variation in the nuclear and electronic energy loss as ions penetrate the film. The initial loss of nitrogen and oxygen for all exposures is generally compatible with desorption of NO_2. Further, the change in N and O content appears to scale with the total deposited electronic energy density. These results provide at least circumstantial evidence that RO–NO_2 bond breaking is one of the dominant processes. For the cases of H, He and C exposure, a carbonaceous layer persists after prolonged exposure. The complete removal of the film by Ar irradiation suggests that binary collisions associated with nuclear energy loss are an important factor in determining the onset of volatilization.

* Corresponding author. Tel. +1 615 343 7225, fax +1 615 343 7263, e-mail weller@vuse.vanderbilt.edu.

SSDI 0168-583X(95)00381-9

2. Experiment

A stock solution of nitrocellulose $(C_6H_7N_3O_{11})_n$ in amyl acetate was diluted to a concentration of 1.5%. Using a syringe and a #18 needle, a single drop of liquid was cast on the surface of a deionized water bath. After allowing the solvent to partially evaporate, the film was drawn onto a clean 1-inch silicon wafer (Virginia Semiconductor). Each sample was dried in air for 30 minutes, then heated in a N_2 ambient at 80°C for another 30 minutes to remove any remaining solvent. A thickness of 17 nm was estimated based on the weight of a drop of solution, the area of the cast film, and a density of 1.2 g/cm^3 for nitrocellulose.

The samples were placed in a vacuum chamber with a nominal base pressure of 10^{-8} Torr. H^+, He^+, C^+ and Ar^+ ions were accelerated to 270 keV and directed at normal incidence to the samples. During each irradiation, the ions were rastered over a 0.6 ± 0.1 cm^2 area with a current density of approximately 0.02 μA/cm^2. At predetermined intervals, the exposures were interrupted and time-of-flight elastic recoil detection was used to measure the atomic composition of the film.

Complete descriptions of the time-of-flight detection scheme and its application to the detection of light elements are given elsewhere [7,8]. Briefly, a beam of 810 keV Ar^{3+} ions is directed at an angle of 21° to the sample surface. Light element recoils from the film, Si atoms from the substrate, and the scattered beam are detected at a 42° forward scattering angle relative to the initial beam direction. The particles pass through a thin carbon foil and generate one or more secondary electrons that, when detected by a microchannel plate, trigger a start pulse. The particles themselves generate a stop signal at a second microchannel plate after traversing a 37 cm flight path. Although the recoil energies determined by collision kinematics are usually larger for high-mass recoils, light atom recoils have the greater velocity and are well separated from Si and Ar events in the time-of-flight spectrum. The total number of ions needed to obtain each measurement was 1×10^{11}. By working at beam energies lower than for conventional elastic recoil detection, the total energy deposited in the sample is reduced and sensitivity to light elements is enhanced, due to the larger recoil cross sections. Hence, the damage to radiation sensitive material is minimized during analysis.

3. Results and discussion

A representative time-of-flight spectrum for a pristine nitrocellulose film is shown in Fig. 1a. Recoil H is easily identified, while overlap of the recoil C, N, and O features is observed due to straggling and energy loss in the film from both the incident Ar and recoil species. In short, the film is of sufficient thickness to cause a light element

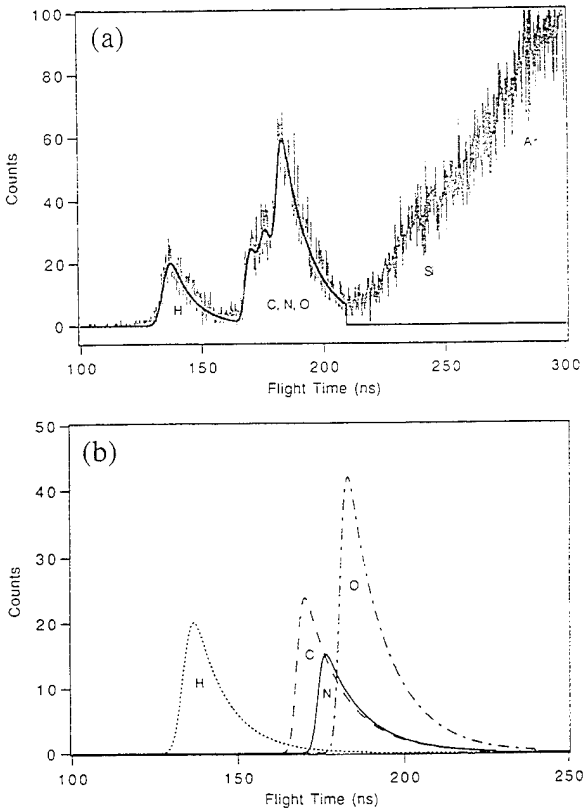

Fig. 1. (a) 810 keV Ar^{3+} time-of-flight spectrum and least-squares fit for a nitrocellulose thin film on Si. 1×10^{11} ions were deposited in the analysis. (b) Individual contributions of recoil H, C, N and O from the fit in (a).

recoil emerging from some depth within the film to have the same velocity as a heavier recoil near the surface. Though the profiling of much thinner layers could have reduced or eliminated this overlap, the erosion of the film then progresses too rapidly for a detailed series of measurements to be made. In order to extract the atomic concentrations of H, C, N, and O for each analysis, a peak fitting algorithm was employed. The time-of-flight distribution $f(z)$ of a particular recoil species from a thin uniform layer, modified by energy loss and straggling, can be described empirically by a function that is the convolution of a Gaussian with a decaying exponential.

$$f(z) = \frac{Ak}{2} \exp\left[\frac{k\left(k\sigma^2 - 2(z - z_0)\right)}{2}\right] \times \left(1 - \operatorname{erf}\left[\frac{\sigma}{\sqrt{2}}\left(k - \frac{z - z_0}{\sigma^2}\right)\right]\right), \quad (1)$$

where $f(z)$ has been normalized so that A gives the total yield, k is the decay constant, σ the Gaussian standard deviation, and z_0 is the calculated flight time corresponding to recoils from the surface. The complete fitting function is the sum of the contributions in the form given in

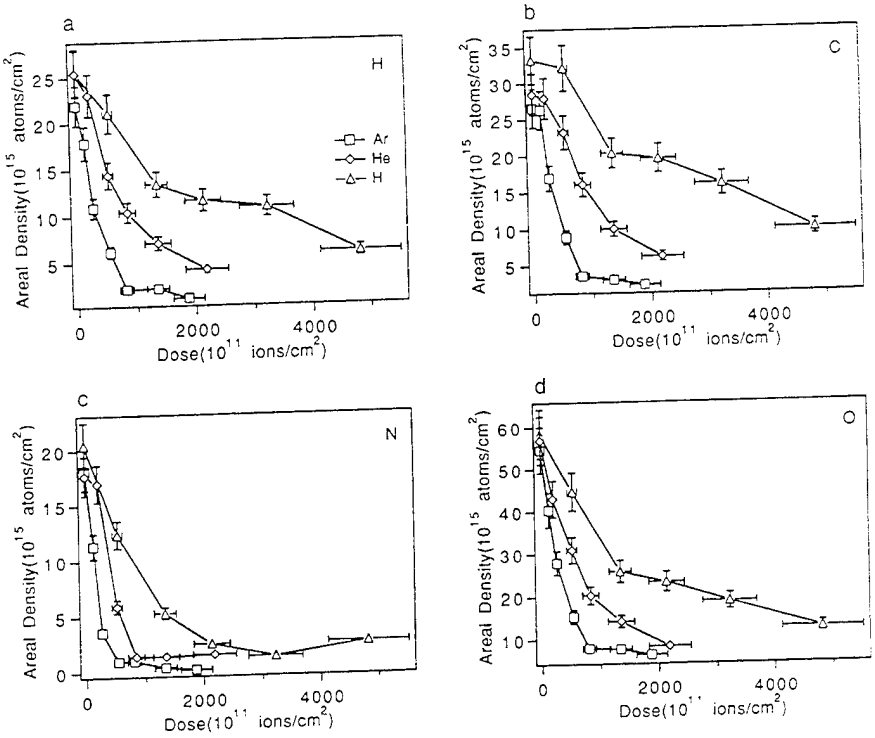

Fig. 2. (a)–(d) Change in the components H, C, N and O as a function of dose for Ar (□), He (◇), and H (△) irradiation. The points are connected to aid the eye.

Eq. (1) for each component of the film. A total of eight parameters were used, including a yield for each of the four elements and a decay constant and width for H. A single decay constant and width were assumed in describing C, N, and O, since the recoil velocities and energy loss characteristics are similar. The result of this general, non-

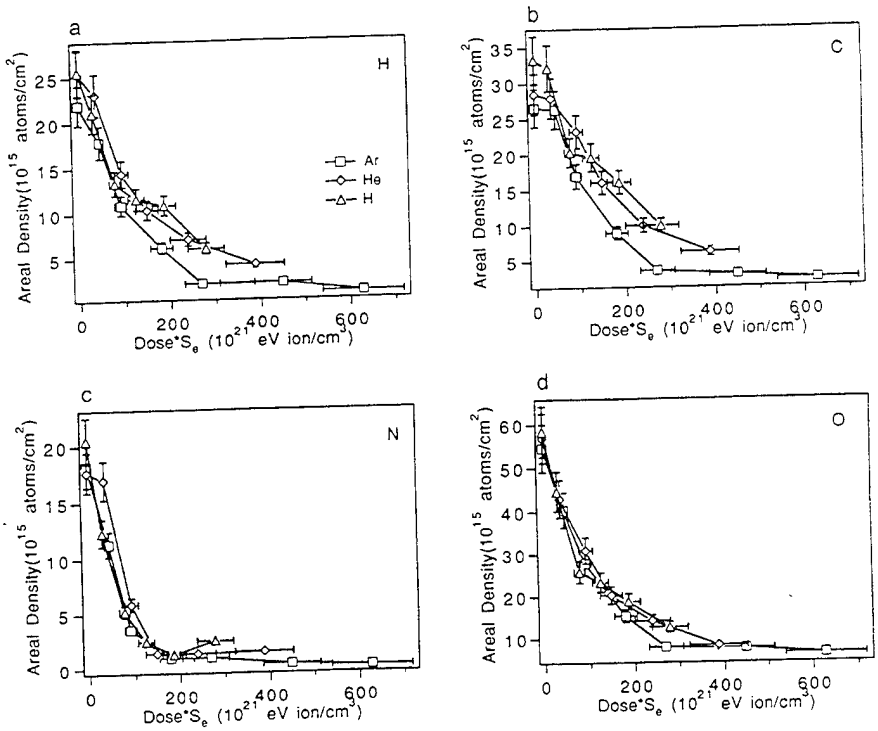

Fig. 3. (a)–(d) Change in the components H, C, N and O with the electronic energy density for Ar (□), He (◇), and H (△) irradiation.

linear least squares fit to the data, with uncertainties determined by counting statistics, is also shown in Fig. 1a. The observed value of χ^2 for this fit, 376.2 for 368 degrees of freedom, was typical of the results obtained for all analyses. Fig. 1b shows the individual contributions of each species to the time-of-flight spectrum in Fig. 1a. For each computed yield, the areal density was calculated based on measured values for the detector efficiency, the Lenz–Jensen recoil cross section, and the number of incident ions. The initial stoichiometry and thickness generally agree with predicted values to within the $\pm 10\%$ estimated uncertainty.

The evolution of the atomic components of the nitrocellulose film, subject to H, He, and Ar irradiation, is shown in Fig. 2 as a function of the dose. The data for C exhibits a rate of removal between those for He and Ar but are omitted from the graphs in order to simplify presentation and because of a smaller initial sample thickness. Not unexpectedly, the removal rate increases with the mass of the incident ion. It is important to note that the ions used in erosion differ greatly in both their relative and absolute values of the electronic and nuclear energy loss, S_e and S_n. Using an implementation of the TRIM algorithm [9], the electronic stopping power in nitrocellulose has been calculated to be 57.9, 177, 305, and 335 eV/nm for 270 keV H, He, C, and Ar ions while the nuclear stopping is 0.055, 0.735, 13.7 and 198 eV/nm, respectively. Studies of the ion beam modification of polymers other than nitrocellulose have suggested that electronic excitations alter the chemical structure creating ionized molecules, collective excitations, and highly excited species [10]. Fig 3 shows the variation of H, C, N, and O with the product of dose and electronic energy loss. While a scaling with the total deposited energy may not be ruled out completely, the overlap of the N and O curves suggests that the density of electronic energy deposition is a key parameter influencing the desorption of these components. From the basic structure of the nitrocellulose repeat unit, shown in Fig. 4, a

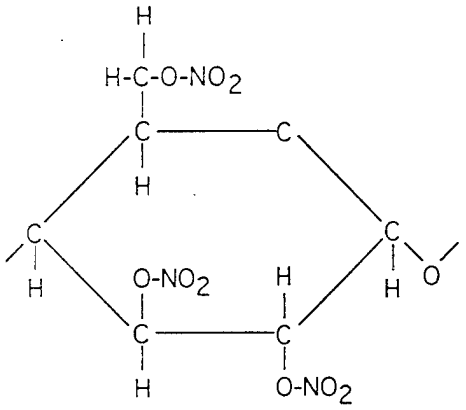

Fig. 4. Chemical structural formula of the nitrocellulose.

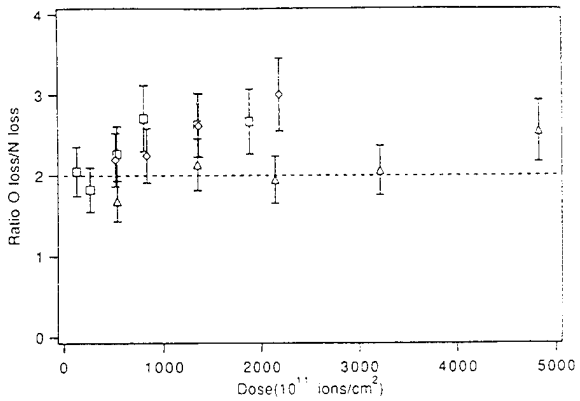

Fig. 5. Ratio of oxygen to nitrogen loss as a function of dose for Ar (□), He (◇), and H (△) irradiation. The dashed line indicates the ratio consistent with the stoichiometry of NO_2.

likely path for the removal of N and O is the breaking of radical O–NO_2 bonds. It has been previously suggested that under thermal annealing, RO–NO_2 bond breaking acts as a trigger for the total decomposition of the molecule [11]. Additional evidence for this mechanism can be seen in the stoichiometry of the removal of N and O. The ratio of removed oxygen to removed nitrogen is plotted as a function of the accumulated dose in Fig. 5. For each of the incident ions, the initial ratio is consistent with the selective excision of NO_2 fragments. For H irradiation, this ratio is effectively maintained throughout the exposure and may indicate the formation of a residue.

Examination of the erosion curves in Figs. 2a and 2b shows essentially complete removal of H and C under Ar irradiation. The remaining coverage of light elements is approximately the same as that found on a clean Si wafer. This result is not inconsistent with an earlier suggestion of a threshold based on a total energy loss of 350 eV/nm for volatilization of the residue [4]. For H, He and C irradiation, a carbon-rich, oxygen-depleted layer remains, suggesting that highly cross-linked, carbon networks could be formed by the reaction between adjacent radicals. The remaining residue is nearly twice as thick after H exposure compared with similar data for He while no statistically significant difference in stoichiometry is noted. For H and He irradiation, the overlap of the plots of removed H and C in Figs. 3a and 3b may point to a common bond breaking mechanism also based on electronic excitation. The H and C curves for Ar irradiation appear to overlap initially but decrease quickly as the film is removed. An additional mechanism is needed to explain the removal of the residue by Ar. As evidenced by the large difference in nuclear stopping between Ar and H or He, binary collisions could likely play a key role. Using the empirical formula of Matsunami et al. [12], comparative estimates of sputtering yields for carbon by 270 keV Ar, He, and H are 0.72, 0.002, and 9.7×10^{-5} atoms/ion, respectively.

Given that roughly 5×10^{15} atoms/cm^2 of carbon remain after He erosion, an exposure equal to the accumulated Ar dose, $\sim 2 \times 10^{14}$ ions/cm^2, could not remove this residue. Hence, simple differences in physical sputtering appear inadequate to explain complete removal of the film by Ar given the residue left by He. It appears more likely that a desorption mechanism incorporating collisional sputtering would proceed in conjunction with the bond breaking generated by electronic excitations rather than after the formation of a residue.

4. Conclusion

Medium energy time-of-flight elastic recoil detection has been applied in the study of the real-time evolution of the atomic composition of nitrocellulose under H, He, C, and Ar ion irradiation. The technique has been shown to be a useful tool for the study of these radiation sensitive materials. The initial stoichiometry of desorbed N and O is consistent with a reaction involving the breakage of RO–NO_2 bonds. Good correlation is obtained between the removal of N and O and the electronic energy loss under all irradiation conditions. Removal of H and C show a similar scaling for H and He ions but differs for Ar because of the complete removal of the residue. The larger number of binary collisions experienced by Ar ions, as indicated by the higher nuclear stopping power and sputtering yield, is probably responsible for this observed behavior.

Acknowledgments

This work was supported in part by the U.S. Army Research Office under contract DAAL 03-92-G-0037.

References

[1] M.W. Geis, J.N. Randall, T.F Deutsh, N.N. Efremow, J.P. Donnelly and J.D. Woodhouse, J. Vac. Sci. Technol. 3 (1985) 343.
[2] H. Kaneko, Y. Yasuoka, K. Gamo and S. Namba, Jpn. J. Appl. Phys. 28 (1989) 716.
[3] H. Kaneko, Y. Yasuoka, K. Gamo and S. Namba, Jpn. J. Appl. Phys. 28 (1989) 1113.
[4] R. Mühle and G. Götz, Nucl. Instr. and Meth. B 46 (1990) 347.
[5] J.P. Moliton, T. Triguad and A. Moliton, Nucl. Instr. and Meth. B 65 (1992) 428.
[6] L. Merhari, J.P. Moliton, and C. Belorgeot, J. Appl. Phys. 68 (1990) 4837.
[7] M.H. Mendenhall and R.A. Weller, Nucl. Instr. and Meth. B 40/41 (1989) 1239.
[8] J.H. Arps and R.A. Weller, Nucl. Instr. and Meth. B 79 (1993) 539.
[9] J.P. Biersack and L.G. Haggmark, Nucl. Instr. and Meth. 147 (1980) 257.
[10] G. Marletta, Nucl. Instr. and Meth. B 46 (1990) 295.
[11] H. Kaneko, Y. Yasuoka, K. Gamo and S. Namba, J. Vac. Sci. Technol B 1 (1989) 1778.
[12] N. Matsunami et al., Atom. Data Nucl. Data Tables 31 (1984) 1.

12. Low-energy sputtering of liquid Ga-In

Nuclear Instruments and Methods in Physics Research B 100 (1995) 444–449

NIM B
Beam Interactions with Materials & Atoms

ELSEVIER

Loss of material from Ga–In liquid surface during bombardment by hyperthermal Ta, Pt and Au atoms

Martha Riherd Weller [a,*], Robert A. Weller [b]

[a] *Middle Tennessee State University, P.O. Box 403, Murfreesboro TN 37132, USA*
[b] *Vanderbilt University, Nashville, TN 37235, USA*

Abstract

We have investigated the loss of incident atoms and of substrate atoms from the surface of the liquid Ga–In eutectic alloy during bombardment of the surface with hyperthermal Ta, Pt and Au atoms. Hyperthermal atoms were produced by sputtering solid metallic targets positioned directly above the liquid Ga–In surface. By analyzing material deposited on graphite collector surfaces which surrounded the liquid alloy during bombardment, angular distributions were determined for atoms leaving the liquid surface as a result of the bombardment. For all three species of incident atoms, we detected Ga and In as well as the primary sputtered species on the collectors. The angular distributions for the primary sputtered species were strongly peaked in a near-normal direction consistent with direct reflection from the liquid surface. In all cases, we observed angular distributions for the Ga which included a broad peak, centered near the surface normal, although not at the same angle as the maximum for the incident species. Such a broad distribution is consistent with secondary sputtering of the liquid surface by the incoming atoms. The distribution of indium atoms is also suggestive of sputtering. However, we observed significant asymmetry in the In distributions which may be correlated with the angular distributions for the incident species. Our results support previous data indicating that surface sputtering (or re-sputtering) and direct reflection of primary sputtered atoms are significant mechanisms for the loss of material from surfaces during hyperthermal processes such as sputter deposition.

1. Introduction

Sputter deposition of thin films has been of interest for many years from both a technical and a scientific viewpoint. Sputter-deposited films have a number of practical applications such as the fabrication of semiconductor devices [1], and have long been used as a method of investigating the sputtering process itself [2,3]. Understanding the mechanisms responsible for the loss of material from sputter-deposited films is important for all of these studies since the properties of the final film depend both on the deposition rate and on the loss rate. Re-sputtering by backscattered beam ions has long been recognized as a likely process [4], but other mechanisms [5,6], involving the interaction of sputtered atoms with the sputter-deposited surface, have also been proposed.

The dynamics of the interaction of an energetic atom with a surface are influenced by several parameters including the energy, E, of the incident atom as well as the masses of all the atoms involved. Atoms with very low energies (< 1 eV) interact with the surface as a whole, or at least with several atoms simultaneously, while atoms with significantly higher energies (> 10 eV) interact through binary collisions involving only one target atom at a time. Sputtered atoms have an energy distribution of the form $E/(E+E_B)^3$ [7] where E_B is the surface binding energy, typically a few eV, for the sputtered material. Consequently these atoms have energies which span the transition region between whole surface interactions and binary collisions; the binding energy of the sputtered species determines the fraction of sputtered atoms with low energy relative to those with high energy.

The significance of the high energy portion of the sputtered particle spectrum is evident in studies [5] which show that resputtering of previously deposited atoms by these particles dominates resputtering by backscattered beam ions in some cases. However, resputtering has been ruled out as a loss mechanism for at least one system [8]. Although direct reflection of sputtered atoms from surfaces has been rejected as a loss mechanism based on the kinematics of binary collisions [5], low energy sputtered particles should interact with several atoms simultaneously so that reflection is feasible. In the absence of chemical effects, the relative importance of these two types of

* Corresponding author, tel. +1 615 898 2792, fax +1 615 898 5182, E-mail: mrw@physics.mtsu.edu.

SSDI 0168-583X(94)00817-5

interactions should vary systematically with the binding energy of the sputtered species in the original target.

We have measured angular distributions for material ejected or reflected from the liquid surface of the Ga–In eutectic alloy during exposure to the sputtered Ta, Pt and Au atoms. The three species selected for sputtering have similar masses (ranging from 181 u to 197 u), but substantially different binding energies (7.9 eV for Ta, 4.9 eV for Pt and 3.6 eV for Au) and thus different energy distributions. Our results suggest that both resputtering and direct reflection are mechanisms for the loss of material from surfaces exposed to sputtered atoms.

2. Experiment

Thick, high purity (> 99.99% for metal constituents in all cases) foils of Ta, Au and Pt were selected for sources of sputtered atoms in this experiment. The Ga–In eutectic alloy was chosen as the deposition surface because it is liquid at room temperature, an important property which eliminates consideration of surface structure or roughness in this experiment. This alloy has a bulk composition of 17 at.% In, 83 at.% Ga, but In segregates at the surface when the alloy is clean [3]. Thus, the alloy surface is nearly 100% indium. High-purity graphite foils were chosen for the secondary collector foils in this investigation because of the minimal interference this substrate presents during backscattering analysis of surface thin films.

The liquid alloy was loaded into a horizontal boat which was initially located in an auxiliary chamber, isolated from the target chamber. Immediately prior to the sputtering stage of the experiment, the surface of the alloy was sputter cleaned until Auger analysis showed no oxygen or carbon contamination of the alloy surface. After cleaning was completed, the liquid alloy was transferred in vacuo into the main target chamber.

Fig. 1 shows the geometry for the sputtering phase of the experiment. We mounted the sputter targets (Au, Pt, Ta) at an angle of 30° from the horizontal, facing downward. Narrow strips of graphite foil were clamped into place on a half-cylindrical holder which had an inner diameter of 2.54 cm. Each collector foil had a small circular hole at its center, directly below the center of the target foil, permitting sputtered atoms to impinge upon the liquid metal surface directly below the target. Ambient pressure in the target chamber was approximately 1×10^{-9} Torr.

Sputtering was performed using 150 keV Ar^+ ions. During the sputtering process, the beam passed through a 0.6 cm diameter hole and struck the target at an incidence angle of 60°. Sputtered atoms were ejected from the target in all directions. Atoms exiting through the small hole directly beneath the target impinged upon the surface of the liquid metal collector where they were either reflected from the surface or absorbed within the metal. During this process, In and Ga atoms were also ejected from the liquid metal surface. Reflected sputtered atoms and ejected alloy atoms were collected on the graphite collector surrounding the liquid metal pool.

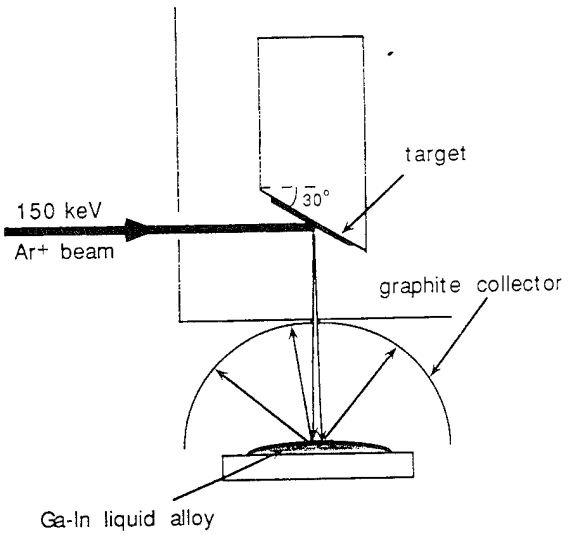

Fig. 1. Experimental geometry for collection of material lost from Ga–In alloy surface during sputter deposition onto liquid surface.

The metal targets were sputtered for Ar^+ doses ranging from 0.7 C for Ta to 1.0 C for Pt. The beam dose was determined by experimental operating conditions. Using the procedure of Matsunami et al. [9], we estimate total exposures for the liquid metal to the primary sputtered species of 1×10^{16} Ta atoms, 4×10^{16} Pt atoms, and 6×10^{16} Au atoms. In making these estimates, we have assumed an angular dependence of cos θ for the primary sputtered particle yields where the ejection angle for sputtered atoms as measured from the surface normal is $\theta = 30°$ for this geometry.

When sputtering was completed, the liquid metal alloy was immediately returned in vacuo to the auxiliary chamber and re-analyzed by Auger spectroscopy. This analysis revealed a very small level of oxygen contamination and no evidence of the primary sputtered species, indicating that these atoms did not remain on the alloy surface after incidence. Since the equivalent of several monolayers of each primary sputtered species was incident on the alloy surface, we would expect to observe the deposited atoms had they remained near the surface.

The final stage of the experiment consisted of analysis of the graphite collector foil by medium energy backscattering spectrometry [10]. 270 keV $^4He^+$ ions were used for the analysis. Compositions of the material collected on the surface of the graphite were determined at several positions on the collector, yielding angular distributions for the collected species. Data were taken at positions corresponding to approximately 5° intervals along the collectors.

3. Results and discussion

Figs. 2–4 show the angular distributions obtained for material deposited on the graphite collector surfaces during bombardment of the Ga–In liquid metal surfaces with Ta, Pt and Au sputtered atoms. Fig. 2 shows the distribution for the primary sputtered species. Fig. 3 consists of angular distributions for Ga atoms ejected from the liquid metal during bombardment while Fig. 4 shows the angular distributions for In in each case. For Figs. 3 and 4, each plot represents the actual accumulated counts during analysis normalized to correspond to equivalent analysis doses and equivalent sputter exposures. In addition, to facilitate direct comparisons of yields for the primary sputtered species, the plots in Fig. 2 have been scaled by the backscattering cross section for the species of interest relative to the cross section for gold (Lenz–Jensen for 270 keV He^+ scattered at 150°). Except for Fig. 3, the solid lines should be regarded simply as lines to guide the eye.

There are a number of sources of experimental uncertainty associated with this experiment. Statistical uncertainties in the backscattering peak areas varied with location on the target. These ranged from above 10% in some cases to only 1% in others and are shown explicitly in the figures. There was also an uncertainty associated with the analysis position on the collector foil which was at most 2°. In comparing yields between different sets of data, there is a significant uncertainty in the estimate for the number of sputtered particles incident on the liquid metal in each case due to uncertainties in the estimated sputtering yield, the current integration during sputtering, and the position of the sputtered metal relative to the liquid metal surface. The detector efficiency is energy dependent, but the uncertainty in its value may be neglected when com-

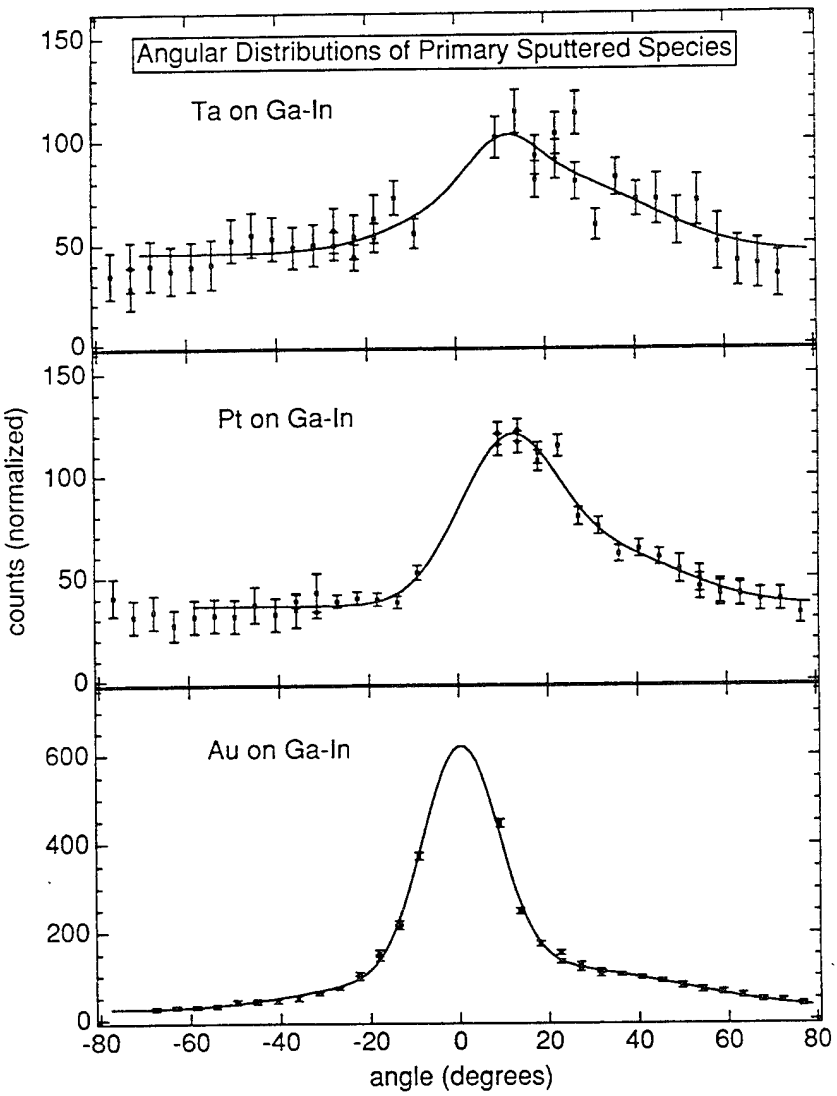

Fig. 2. Angular distribution on secondary collector foil for the primary sputtered species incident on Ga–In alloy surface.

paring backscattering yields from targets having similar masses. Thus, we expect to find essentially the same efficiencies for the data shown in Fig. 2 and can compare these results directly. Similarly, all the data in Fig. 3 correspond to the same detector efficiency (but different from Fig. 2) as do the data in Fig. 4. The solid angle of the detector is the same for all measurements and its uncertainty need not be considered for relative measurements.

Examining all the angular distributions, we note the lack of symmetry about 0° which may be attributed to several factors. The experimental apparatus itself is not symmetric. Even for a uniform, perfectly centered, but finite diameter, Ar^+ beam, backscattered beam particles and sputtered particles originating above the beam center strike the liquid metal at smaller incident angles (measured relative to the surface normal) and over a smaller surface area than do those originating below the beam center. This leads to an asymmetric angular distribution for particles reflected from the liquid metal surface and could reasonably be expected to result in asymmetries in the distribution of atoms ejected from the liquid metal. Lack of uniformity in the beam or a small offset of the beam from the target center can either enhance or diminish the asymmetry, depending on the direction of the variation. In addition, an alloy surface which is slightly asymmetric about the center of the meniscus will result in asymmetric measured distributions for atoms ejected from the metal surface and for reflected atoms.

Looking more closely at the angular distributions for the primary sputtered species (Fig. 2), we note that, in every case, these distributions are more sharply peaked than the corresponding distributions for the alloy constituents. Since the primary sputtered species was not observed on the liquid metal surface after completion of

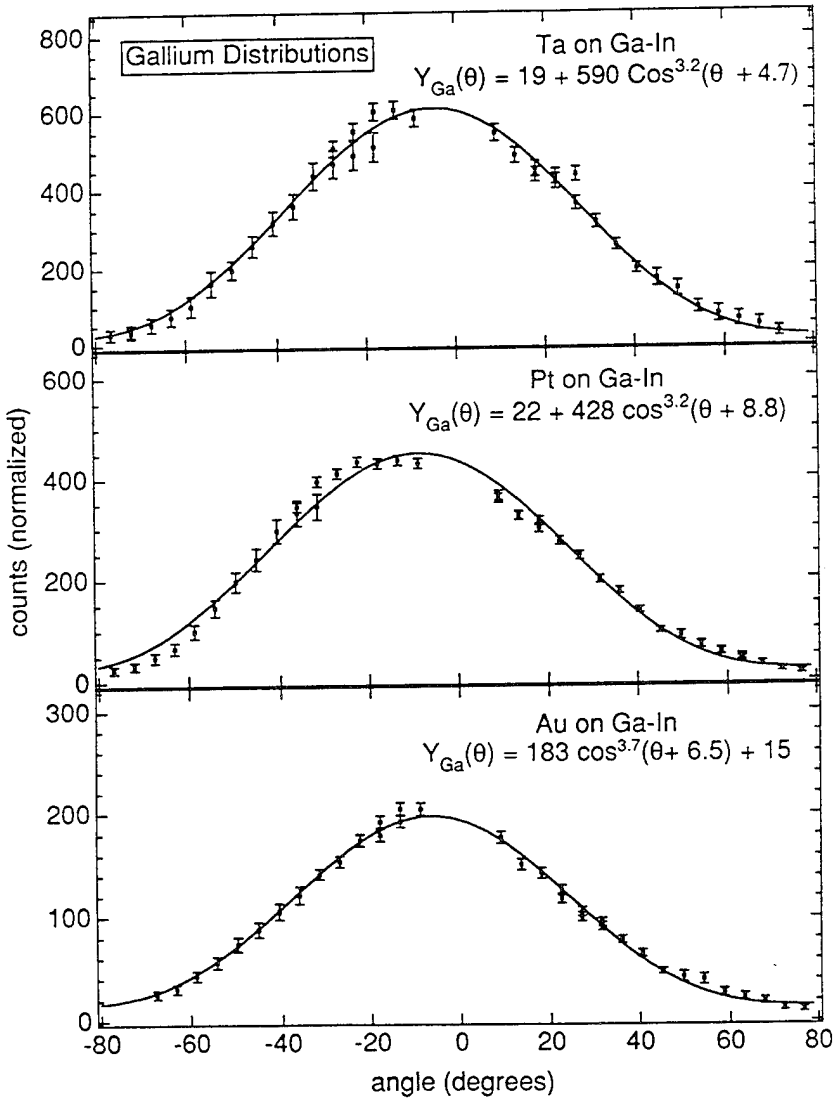

Fig. 3. Angular distribution on secondary collector foil for Ga removed from Ga–In alloy surface.

sputtering, these distributions are unlikely to result from resputtering of atoms deposited on the alloy surface. The relative yields for the three species are consistent, however, with direct reflection from the alloy surface. Low-energy atoms are more likely to be reflected from the surface since they interact simultaneously with several atoms rather than with a single atom. (Winters et al. [11] found that Xe and Ar atoms colliding with Pt behaved as if they had struck an effective mass of 1.5 Pt atoms for incident energies of 10 eV while, for incident energies below 1 eV, the effective mass was 5 Pt atoms.) Since the average energy of sputtered atoms scales with surface binding energy, we observe that Au atoms are reflected more efficiently than Pt atoms while Ta atoms bounce back less efficiently. This explanation is consistent with studies by Libbrecht et al. [8] showing that low energy sputtered uranium atoms were more likely to be lost from collector surfaces than their higher energy counterparts. (This particular study also ruled out resputtering as a loss mechanism for sputter-deposited uranium atoms.)

The overall shapes of our angular distributions for the primary sputtered species are similar to angular distributions obtained by Rettner et al. [12] for scattering of low-energy Xe from Pt. (Although Xe is lighter than Pt, this comparison is reasonable since heavy atoms having energy below 10 eV scatter from an effective mass larger than that of a single substrate atom.) For non-normal incidence, the peak in the distribution occurs at an angle significantly beyond the specular result due to incomplete momentum reversal perpendicular to the surface. The extent to which this occurs determines the width of the peak with lower energies resulting in narrow peaks since the

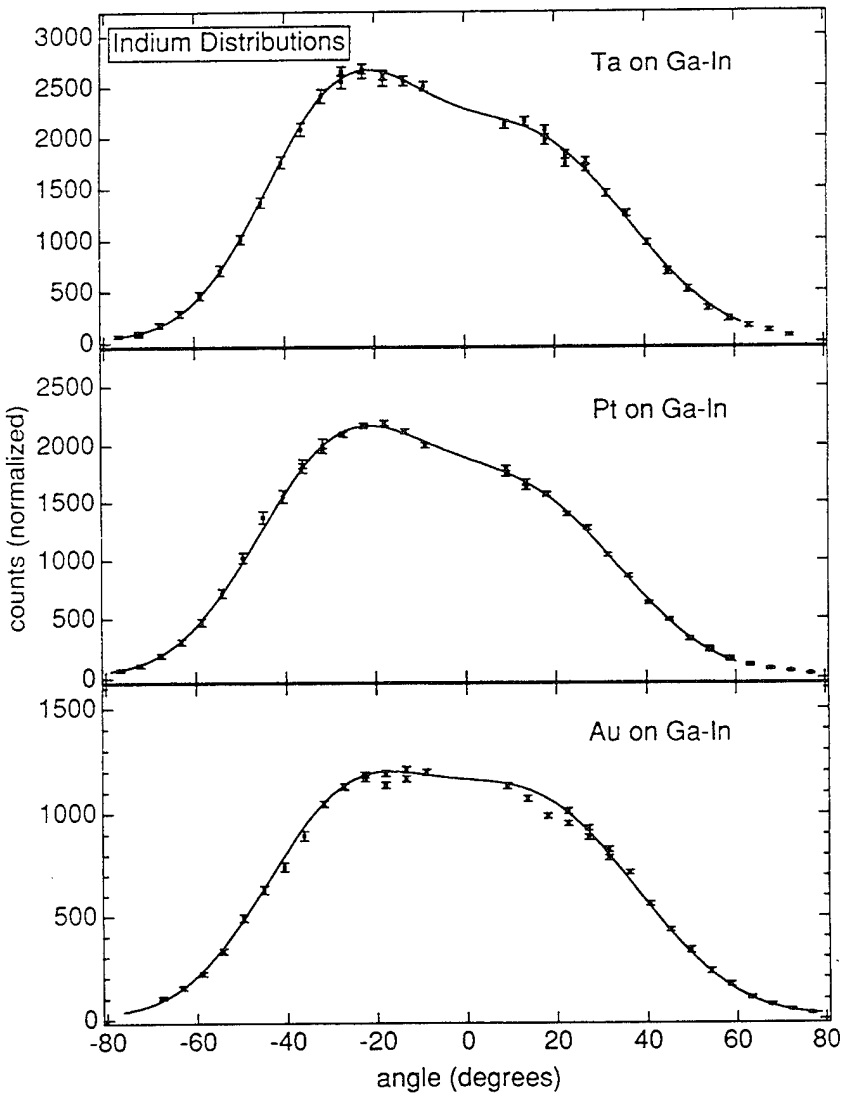

Fig. 4. Angular distribution on secondary collector foil for In removed from Ga–In alloy surface.

normal component of momentum is more effectively reversed. The long tails to the distributions presumably result from particles backscattered via multiple collisions.

The angular distributions for gallium atoms (Fig. 3) were broad and much more symmetric than those for any other species. Anticipating a sputtering-type distribution, we fit these data to the form

$$Y(\theta) = A_1 \cos^p(\theta - \theta_1) + B. \quad (1)$$

The solid lines in Fig. 3 indicate excellent fits for tantalum and gold incoming atoms. These distributions are similar to the sputtered Ga distributions obtained by both Dumke et al. [3] and Hubbard et al. [13] under more typical sputtering conditions. For incoming particle energies between 3 and 50 keV, they found that the exponent p in Eq. (1) ranged between 2.0 and 4.9, with most values between 3 and 4. While we are not inclined to give any significance to this particular functional form for the Ga distributions, the close resemblance of our data to sputtering distributions obtained for the same material indicates that sputtering of Ga occurs in our system as well. This sputtering may be caused by primary sputtered atoms or by backscattered beam ions.

The angular distributions for indium atoms (Fig. 4) were all relatively broad, qualitatively similar to those found by other groups during sputtering of the Ga–In alloy. Both Dumke et al. [3] and Hubbard et al. [13] obtained symmetric angular distributions for sputtered In which were relatively flat within 30° of the normal direction, falling off sharply at larger angles. For all three indium distributions, we observed a similar rapid decrease in indium concentrations at large angles. For Au incidence, the distribution is symmetric and approximately flat in the central region. For Ta and Pt incidence, we observed asymmetric central distributions with inflections which occurred at the same angles as inflections in the Au spectrum. Comparing the indium angular distributions to those for the corresponding incident species, there appears to be a correlation between the asymmetries in the two sets of angular distributions. We attribute the angular distributions for indium to sputtering by both backscattered beam ions and primary sputtered atoms. We suspect that the asymmetries in the In angular distributions result from asymmetries in the direction and location of impact for the primary sputtered atoms.

4. Conclusions

Measured angular distributions of material lost from a liquid Ga–In alloy during exposure to primary sputtered particles indicate that both Ga and In atoms are sputtered from the alloy, probably by both the primary sputtered species (Ta, Pt, or Au) and backscattered Ar^- beam ions. In addition, angular distributions of the incident sputtered species demonstrate that some of incoming sputtered atoms are reflected from the surface. In a typical sputter deposition on a solid substrate, the relative importance of these processes will be determined both by chemistry and kinematics. Atoms with low binding energies in their original targets will be more easily reflected from the substrate surface, but reflection may also be the dominant loss process for materials such as uranium which are not easily resputtered.

Acknowledgements

We gratefully acknowledge the assistance of Mr. Jeff Ward, Mr. Mark Moser, Mr. David King and Mr. James Arps who assisted with data taking for this project. This project was supported by a Schering–Plough Grant of the Research Corporation. Additional support was provided by the United States Army Research Office under contract DAAL-03092-G-0037.

References

[1] R. Bruce, S. Eicher and W.D. Westwood, J. Vac. Sci. Tech. A 6 (1988) 1642.
[2] H.H. Andersen and H.L. Bay, in: Sputtering by Particle Bombardment I: Topics in Appl. Phys., vol. 47, ed. R. Behrisch (Springer, Berlin, 1981) 145.
[3] M.F. Dumke, T.A. Tombrello, R.A. Weller, R.M. Housley and E.H. Cirlin, Surf. Sci. 124 (1983) 407.
[4] W. Krüger, K. Rödelsperger and A. Scharmann, Z. Phys. 262 (1973) 315.
[5] R. Buckard, D. Hasselkamp, A. Scharmann, K.-H. Schartner and H.-W. Seibel, Radiat. Eff. 109 (1989) 301.
[6] M.R. Weller, M.H. Mendenhall and R.A. Weller, Nucl. Instr. and Meth. B 59/60 (1991) 102.
[7] M.W. Thompson, Philos. Mag. 18 (1968) 377.
[8] K.G. Libbrecht, J.E. Griffith, R.A. Weller and T.A. Tombrello, Radiat. Eff. 49 (1980) 195.
[9] N. Matsunami, Y. Yamamura, Y. Itikawa, N. Itoh, Y. Kazumata, S. Miyagawa, K. Morita, R. Shimizu and H. Tawara, At. Data Nucl. Data Tables 31 (1984) 1.
[10] M.H. Mendenhall and R.A. Weller, Nucl. Instr. and Meth. B 47 (1990) 193.
[11] H.F. Winters, H. Coufal, C.T. Rettner and D.S. Bethune, Phys. Rev. B 41 (1990) 6240.
[12] C.T. Rettner, J.A. Barker and D.S. Bethune, Phys. Rev. Lett. 67 (1991) 2183.
[13] K.M. Hubbard, R.A. Weller, D.L. Weathers and T.A. Tombrello, Nucl. Instr. and Meth. B 40/41 (1989) 278.

13. Depth profiling of ultra-thin silicon oxynitride films

Analysis of a thin, silicon-oxide, silicon-nitride multilayer target by time-of-flight medium energy backscattering

Robert A. Weller, Kyle McDonald, and Diane Pedersen

Vanderbilt University, Nashville, TN 37235, USA.

and

Joseph A. Keenan

Texas Instruments, Inc., Dallas, TX 75265, USA.

Abstract

Initial results of a program to optimize the resolution of a time-of-flight medium energy backscattering system for analyses of thin oxide and oxynitride films on silicon are reported. Through a redesign of the time-of-flight spectrometer, it has been possible not only to reduce the timing uncertainty attributable to differing path lengths but also, by deliberately introducing small path length differences correlated with scattering angle, to significantly reduce the kinematic dispersion resulting from the finite solid angle of the instrument. Straggling and the energy distribution of the secondary electrons which generate the start signal remain as the primary contributors to system timing uncertainty. Initial measurements of SiO_2 and Si_3N_4 multilayer films in the 10 nm thickness range have been made using channeling in the <110> direction of the Si substrate to suppress background. The depth resolution of the measurements appears to be $\approx$ 1.7 nm.

Introduction

Time-of-flight spectrometers designed to analyze ions in the energy range from a few tens to a few hundreds of keV have opened a new window for backscattering and elastic recoil analyses of surfaces. The resulting spectrometry achieves its full potential when applied to films with thicknesses up to a few tens of nanometers. Most recent work has focused upon establishing the efficiency of spectrometers for use in quantitative thin film analysis [1] and upon optimizing their performance for ultra-high sensitivity trace element analysis [2]. In this paper, we revisit the issue of spectrometer resolution with the objective of optimizing a system for the measurement of SiO_2, TiN, Si_3N_4, and similar films which have applications in modern field-effect transistors. The thickness range of interest is from the threshold of detectability up to perhaps 30-40 nm.

The system which we shall consider uses a spectrometer which derives a start signal from secondary electrons emitted by the passage of a backscattered particle through a carbon foil (nominally 1.7 $\mu g/cm^2$) and a stop signal from the particle's subsequent impact on a microchannel plate. The basic elements which contribute to the finite timing resolution of such a spectrometer have been outlined in ref. [3]. They include kinematic dispersion from the finite acceptance solid angle, ion path length uncertainties, electronic timing resolution, straggling in the start foil, non-uniformity in the start foil thickness, and the intrinsic energy spectrum of secondary electrons. Charge exchange in the start foil, which is biased at -400 V, also produces a broadening of spectral features. In addition, backscattering spectra are subject to uncertainties produced by instability of the primary beam, straggling in the target, and several other processes [4]. The objective of this work has been to improve the system resolution until it approaches the limits established by the fundamental physical processes, such as straggling and secondary electron emission, which occur within the spectrometer.

Experimental Procedure

The basic configuration of the time-of-flight spectrometer is shown in fig. 1. In our original design, the stop microchannel plate was mounted normal to the spectrometer axis. Although it was

clearly recognized that this introduced path-length variability, the degree of this variability was judged to be acceptable. In the present context, however, estimates indicated that this less than optimum configuration was the largest single source of instrumental uncertainty in measurements. Of course, for particles entering the spectrometer parallel to the axis, the tilt angles of the foil and stop detector should be the same. However, for particles radiating from a point source, such as the one approximated by the beam spot on the target, there is a distribution of scattering angles and a corresponding distribution of flight paths between the planes of the start foil and the stop detector. A simple geometric construction shows that the width of this distribution of flight paths can be minimized by properly selecting the angle of rotation of the stop detector about an axis which is perpendicular to the plane formed by the incident beam and the axis of the spectrometer. Furthermore, since the velocity of backscattered particles is correlated with scattering angle through the kinematic factor, it is possible to minimize the width of the distribution of flight times by systematically lengthening the flight paths of particles with smaller scattering angles. This optimization is accomplished by a small additional adjustment to the stop-detector angle.

In the system shown in fig. 1, where the tilt of the start foil is 30°, the distance from the target to the foil is 38 cm, and the flight path is 56 cm, the geometric argument implies that the angle of the stop detector should be 12.2°. For α particles backscattered from Si, the optimum value of the tilt of the stop detector has been found to be 15.5°. The angle, as shown in fig. 1, was chosen to be 15° for ease of manufacturability.

In order to assess the distribution of flight times, as well as to compare various alternative designs, we wrote a Monte Carlo code to simulate the effects of 1) beam spot size on the target; 2) all relevant apertures; 3) energy loss, straggling, and multiple scattering in the carbon start foil; and 4) the angles of the start foil and stop detector. Fig. 2 shows the results of the simulation of a time-of-flight spectrum of 270 keV α particles backscattered from a single layer of Si atoms. The three curves on the left are for stop detector angles of 0°, 12.2°, and 15° and omit the effects of energy loss and straggling in the carbon start foil. The curves on the right include stopping and straggling and are for detector angles of 0°, 15° and 30°. It is clear from an examination of these

curves that, with the 15° tilt, the geometrical effects are greatly reduced and that straggling and foil uniformity dominate uncertainty. The suppression of the kinematic dispersion is also seen to be quite significant. It is interesting to note that orienting the stop detector and carbon foil parallel to each other leads to results as poor as those obtained when no attempt is made to optimize the geometry. The 15° curve on the right is well fit by a Gaussian with standard deviation $\sigma \approx$ 0.43 ns. This will be taken to be the contribution to timing uncertainty from geometric factors, straggling, and foil non-uniformity for α particles backscattering from surface Si. Similar curves have been computed for scattering from other species.

To estimate the magnitude of the effects of electronic timing uncertainty and the secondary electron energy spread, which were not included in the simulation, we measured a thin Au layer on Si by proton backscattering at 270 keV. The observed peak was Gaussian in shape with a standard deviation $\sigma \approx 0.45$ ns. Since the standard deviation of the Monte Carlo simulation of this peak was 0.08 ns, we can infer that an upper limit to the combined effects of electron-flight-time dispersion and electronic-timing uncertainty is ≈ 1.04 ns, fwhm. Here and subsequently we will define "resolution" to be the full width at half maximum of an equivalent isolated peak assuming normally distributed data. The fwhm value is 2.35σ for a peak and equal to the 12-88% transition for an edge, which assumes the mathematical form of an error function.

The samples used in this work consisted of three dielectric layers, SiO_2, Si_3N_4 and SiO_x on crystalline Si. The buried oxide layer, whose stoichiometry was not known precisely, was nominally 1.5 nm thick. The SiO_2 layer at the surface was nominally 2.0 nm. The nominal thickness of the nitride layers was 7-8 nm.

In order to increase energy loss and thereby to improve depth resolution, the target normal was oriented at 45° with respect to the beam (and 75° with respect to the spectrometer). Together with a scattering angle of 150°, this resulted in an exit angle for backscattered α particles of 15° above the plane of the target. At 45° it was also (usually) possible by carefully mounting the target to adjust it so that a significant amount of the beam entering the Si substrate was captured in the <110> channel. This greatly reduced the background in the region of the spectrum containing the oxygen

and nitrogen features. In all cases, the incident α particle beam was 270 keV so that the critical angle for channeling was approximately 1°. Beam currents were typically 30-40 nA, while beam spot sizes were approximately 5 mm^2. Total beam exposures of approximately $1\text{-}1.5\times10^{15}$ α particles were used in order to avoid producing significant radiation damage to the targets.

Auger depth profiles were measured for comparison with the backscattering data. The Auger data were acquired by sequential accumulation of spectra and sputtering by a 3 kV Ar^+ ion gun. The double-pass cylindrical mirror analyzer was operated in pulse counting mode. The sample was sputtered for a measured ion dose rather than for a constant time. This is particularly important since the system is automated and runs unattended for long periods during which Ar pressure may vary. The resulting profile of Auger strengths versus accumulated Ar^+ charge were normalized to the same total thickness as observed in the backscattering data.

Results and Discussion

The solid curve in fig. 3 is typical of the spectra which were measured under optimum channeling conditions at a target angle of 45°. The sample has a Si_3N_4 layer which is nominally 7 nm thick. Also shown in fig. 3 is a spectrum obtained from the same target at a target angle of 49°, but with half as much total beam. The data have been mathematically rebinned from time-of-flight to energy spectra, but have not been corrected for spectrometer efficiency or otherwise manipulated. Fig. 4a shows the oxygen-nitrogen region of the spectrum in fig. 3 with background subtracted using a cubic polynomial. Fig. 4b was obtained similarly from another target with nominal nitride thickness of 8 nm. It is clear from comparing these spectra that significant structural information is present. However, to assess the quality of this information we must estimate the instrumental resolution in this energy range. This is an especially difficult task because of the difficulty of obtaining a target and verifying that a target is truly thin. Normally useful candidates such as evaporated Au on Si,which are adequate for proton backscattering, are not useful for α backscattering because of the non-uniformity, both latterally and in depth, of the Au. (In fact, for this particular case, Au can be observed migrating in the substrate under prolonged irradiation.)

Using the standard deviation of the time of flight for α particles backscattered from Si obtained from the simulation described above, along with an estimate of the timing and secondary electron contributions to uncertainty of 0.44 ns obtained from the proton scattering data, and expressing this as an energy uncertainty, we conclude that the instrumental resolution in the region of the Si edge is $\approx$ 2.3 keV. This is substantially smaller than the 4 keV observed by fitting the data of fig. 3 to a difference of error functions, but this comparison is inappropriate because of the complicated structure of this target. Other samples of device-grade Si have yielded edges as sharp as 2.8 ± 0.7 keV suggesting that the model is in reasonable agreement with the data.

For oxygen, the proton data indicate a timing resolution of 0.9 ns. Together with the standard deviation from the simulation this predicts an energy resolution of 1.7 keV. This estimate suggests that the oxygen peaks in fig. 4 are wide enough to contain structural information. The broad smooth curves superimposed on the oxygen feature near 100 keV in figs. 4a and 4b represent a fit to the difference of two error functions. The energy spread in the transition from 12-88% of peak height indicates 2.8 ± 0.7 keV resolution. Less complex samples lead to values as small as 1.8 ± 0.3 keV. Therefore, we adopt the modeled resolution of 1.7 keV to estimate the system's resolution for oxygen in the SiO_2 layer. This energy resolution translates to a depth resolution for oxygen in SiO_2 of 1.7 nm at the incident and scattering angles used in this experiment. Therefore, we conclude that figs. 4a and 4b do indeed have information about the target structure near the surface.

The degradation in resolution with depth has been examined in detail by Williams and Möller [4]. Our resolution is approximately comparable to that which they obtained using a magnetic spectrometer. Although their work suggests that it should be possible to reach this level of resolution near the surface using conventional backscattering with a surface barrier detector, to do so would require a very steep target angle at which the advantage of background suppression afforded by the <110> channel would not be present.

Fig. 5a shows a depth profile derived from the data of fig. 3 using the same procedure which we have used successfully for a number of years to profile thicker semiconductor device structures

from conventional backscattering data [5]. It is, of course, necessary to make some assumptions about target density in order to return a true depth profile. We assume that the bulk density of SiO_2, 2.22 g/cm^3, applies when the oxygen concentration exceeds that of nitrogen and, conversely, that the bulk Si_3N_4 density, 3.44 g/cm^3, applies when nitrogen exceeds oxygen. In light of the resolution inferred above, we conclude that the boundaries of the layers of this target are not abrupt, but that there are measurable transition regions of intermediate composition. This conclusion is supported by the Auger depth profile shown in fig. 5b. Note especially that the nitrogen signal begins to rise almost immediately after the erosion of the surface has begun. This is accompanied by a similarly rapid decrease in the oxygen signal. The similarity of the profiles in fig. 5a and 5b is striking given the difference in the techniques used to produce them. These data suggest that depth resolutions < 2 nm can be achieved routinely in targets such as these. Differences between the spectra of figs. 5a and 5b such as the relative concentrations at depths greater than ≈ 9 nm will be the subject of future research.

Conclusion

An improved time-of-flight spectrometer design has significantly reduced the contribution to measurement uncertainty from path length variability and kinematic dispersion. By using favorable target orientation to maximize ion path lengths and suppress background, depth profiles of silicon-oxide/silicon-nitride multilayers with approximately 1.7 nm depth resolution have been measured. The technique appears to be well suited for studying both the structure and composition of gate oxides and diffusion barriers as thin as 10 nm or even less.

Acknowledgments

This work was supported by a grant from Texas Instruments, Inc., by the U.S. Army Research Office under contract DAAL 03-92-G-0037 and by Sandia National Laboratories under contract AH-3292.

References

1. R. A. Weller, J. H. Arps, D. Pedersen, and M. H. Mendenhall, Nucl. Instr. and Meth. **A353** (1994) 579.
2. J. A. Knapp and J. C. Banks, Nucl. Instr. and Meth. **B79** (1993) 457.

3 . M. H. Mendenhall and R. A. Weller, Nucl. Instr. and Meth. **B40/41** (1989) 1239.
4 . J. S. Williams and W. Möller, Nucl. Instr. and Meth. **157** (1978) 213.
5 . J. A. Keenan, unpublished.

Figure Captions

Fig. 1. Schematic of the time-of-flight spectrometer and associated electronics. The drift length is 56 cm. The angles of the carbon start foil and the plane of the stop detector with respect to the spectrometer axis are 30° and 15° respectively.

Fig. 2. Monte Carlo simulation of spectrometer resolution including effects of finite beam spot size, target angle, spectrometer apertures, and stop detector angle. The carbon foil angle is 30°. The curves centered near 202.5 ns are for detector angles of 0° (normal to the axis), 12.2° and 15° and include only geometrical factors, including the backscattering kinematic factor. The curves centered near 204.8 ns, for stop detector angles of 0°, 15°, and 30°, also include straggling and energy loss in the start foil and a foil non-uniformity of 10%.

Fig. 3. Backscattering energy spectra of 270 keV α particles incident on a target with nominal composition of SiO_2, 2 nm; Si_3N_4, 7 nm; SiO_x, 1.5 nm; Si (crystalline). At an orientation of 45°, the beam channels in the Si substrate. The 45° spectrum used 0.24 mC of charge while the 49° spectrum used 0.12 mC.

Fig. 4. a) An expanded view of the region of fig. 3 containing the oxygen and nitrogen features. Background has been subtracted using a cubic polynomial. The heavy solid line on the surface oxygen feature near 104 keV is the result of a fit of the data to the difference of two error functions. b) The nitrogen-oxygen region of a second sample showing what appears to be a narrower Si_3N_4 layer. This measurement used only 3/4 the charge of the one shown in part a. The fit to the surface oxygen peak is shown by a heavy solid line.

Fig. 5. a) Depth profile obtained from the data shown in fig. 3. b) Auger depth profile of the same sample. Curves are relative and not normalized to concentrations. The depth scale is normalized using the backscattering data.

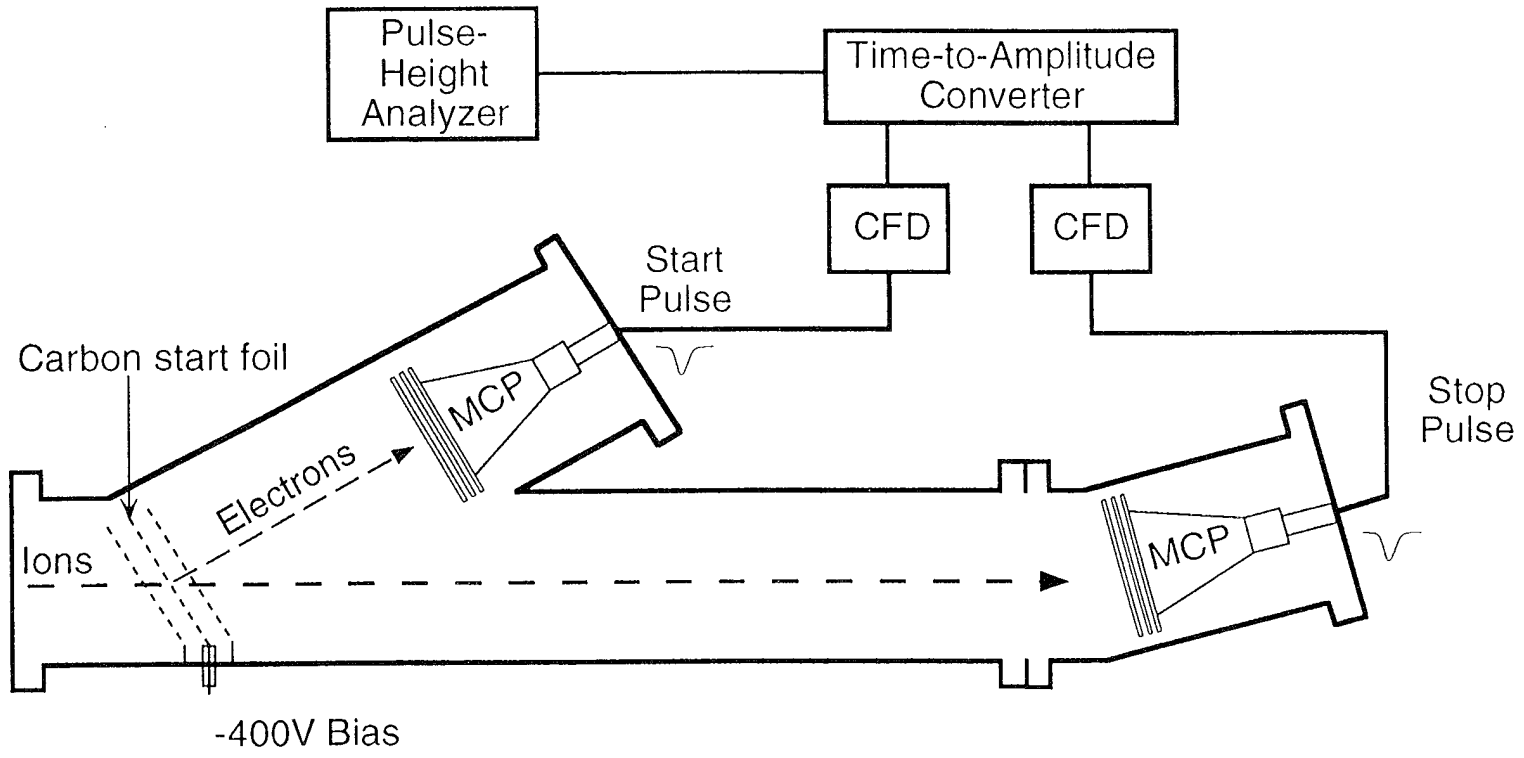
Pulse-
Height
Analyzer
Time-to-Amplitude
Converter
CFD
CFD
Start
Pulse
Stop
Pulse
Carbon start foil
MCP
Electrons
Ions
MCP
-400V Bias

Fig. 1

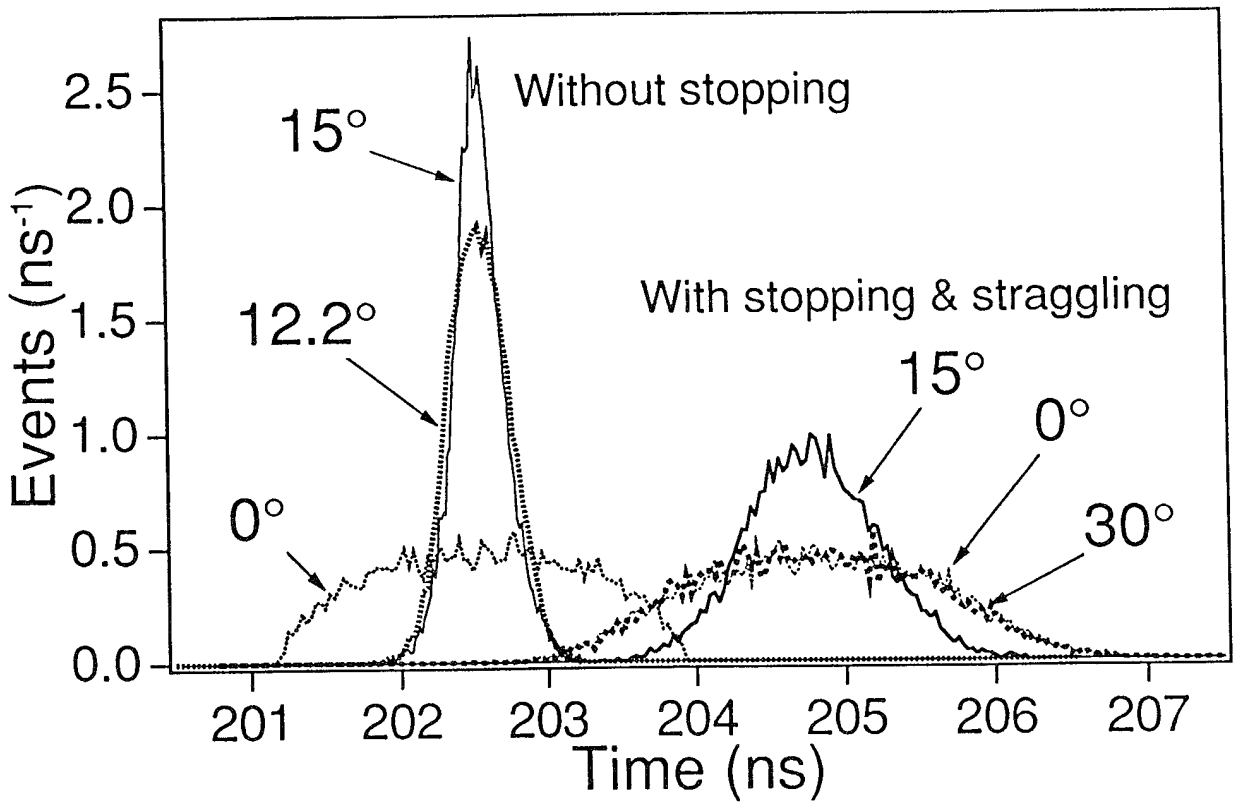
Without stopping
15°
12.2°
0°
With stopping & straggling
15°
0°
30°
Events (ns^{-1})
2.5
2.0
1.5
1.0
0.5
0.0
201
202
203
204
205
206
207
Time (ns)

Fig. 2

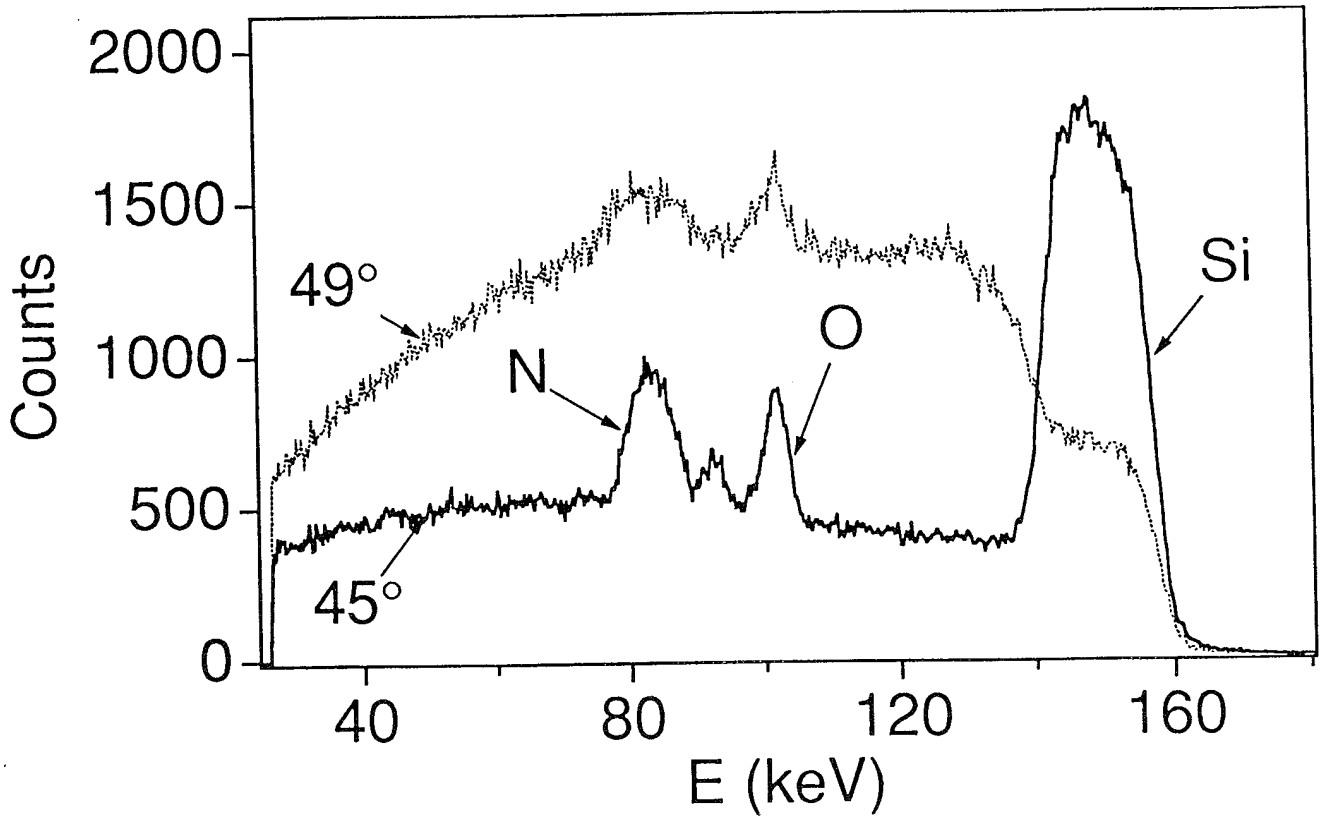

Fig. 3

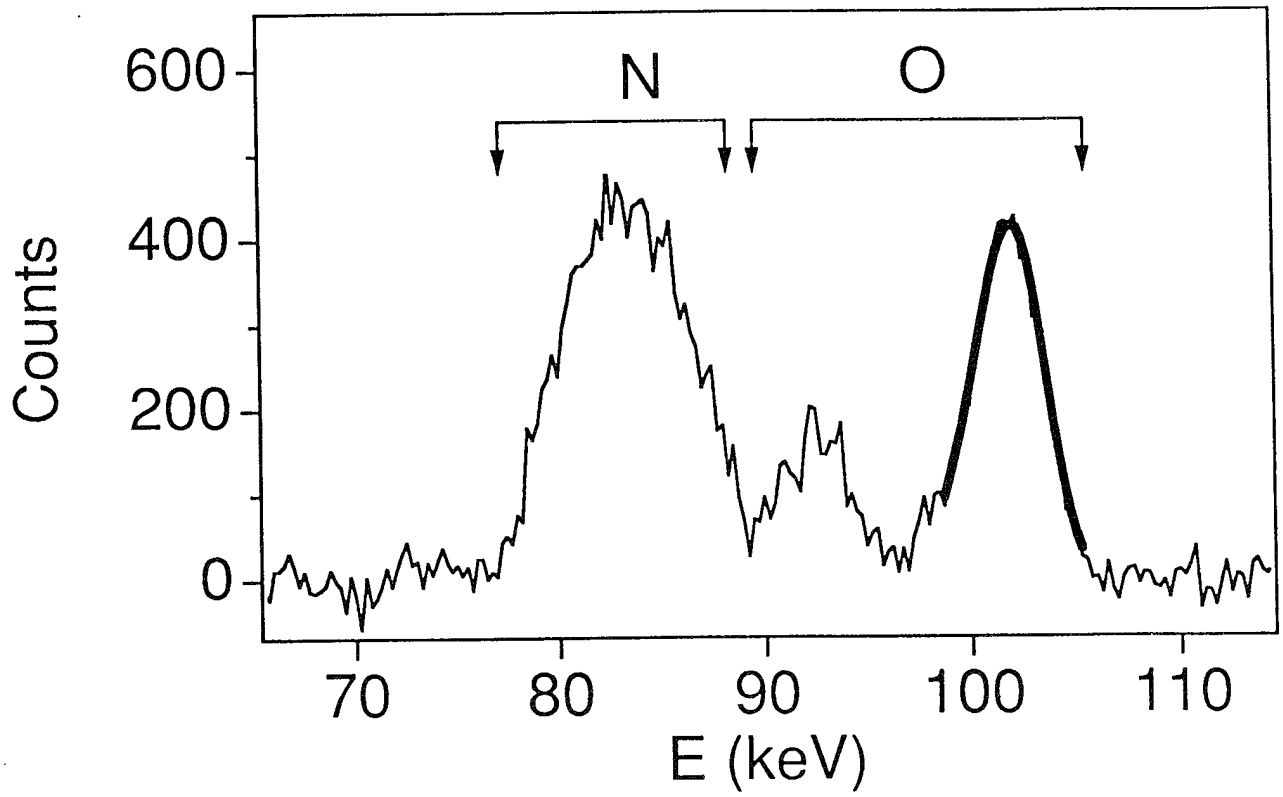

Fig. 4a

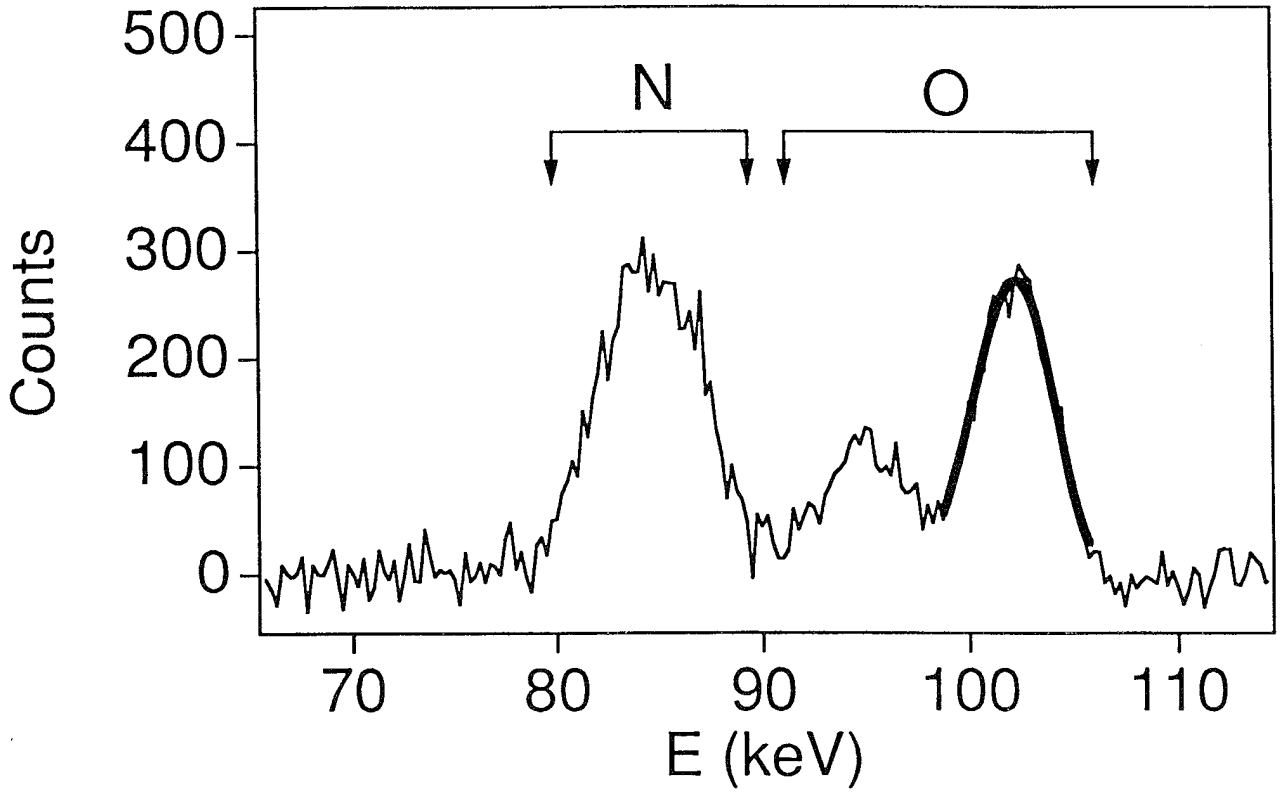

Fig. 4b

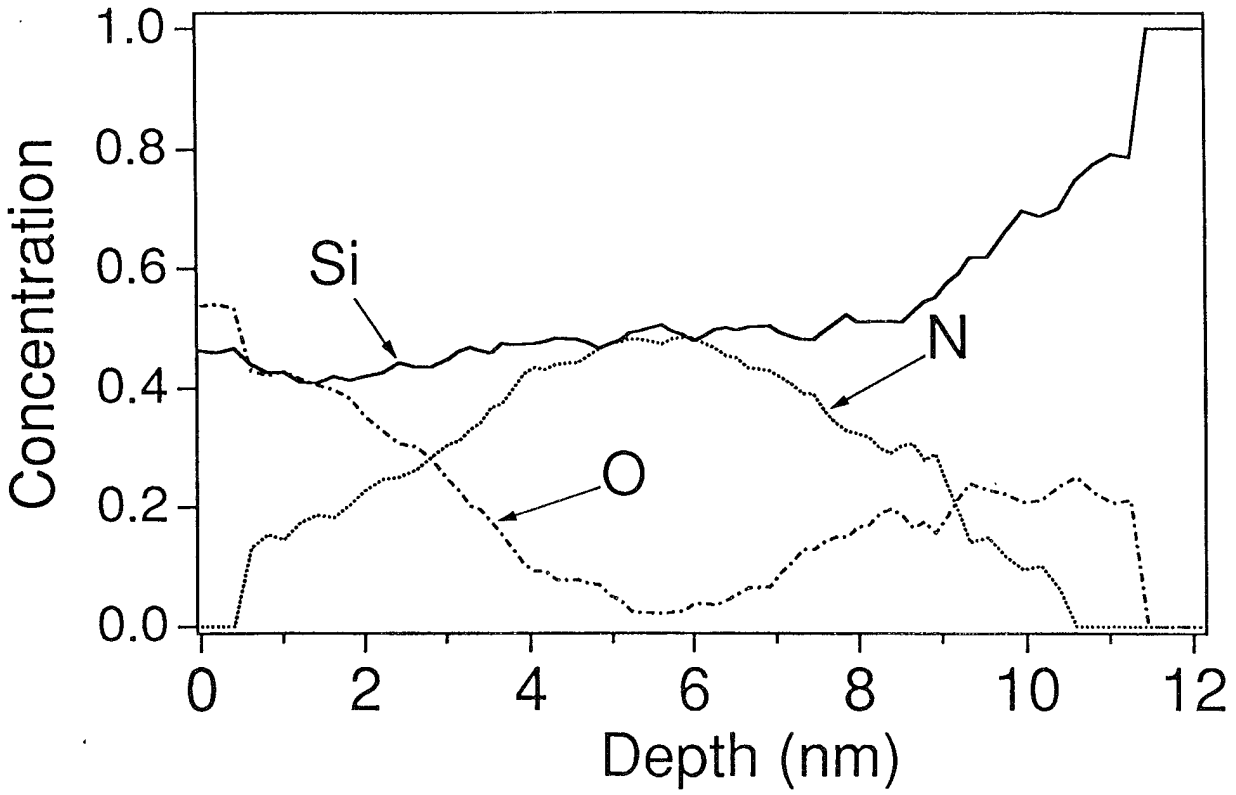

Fig. 5a

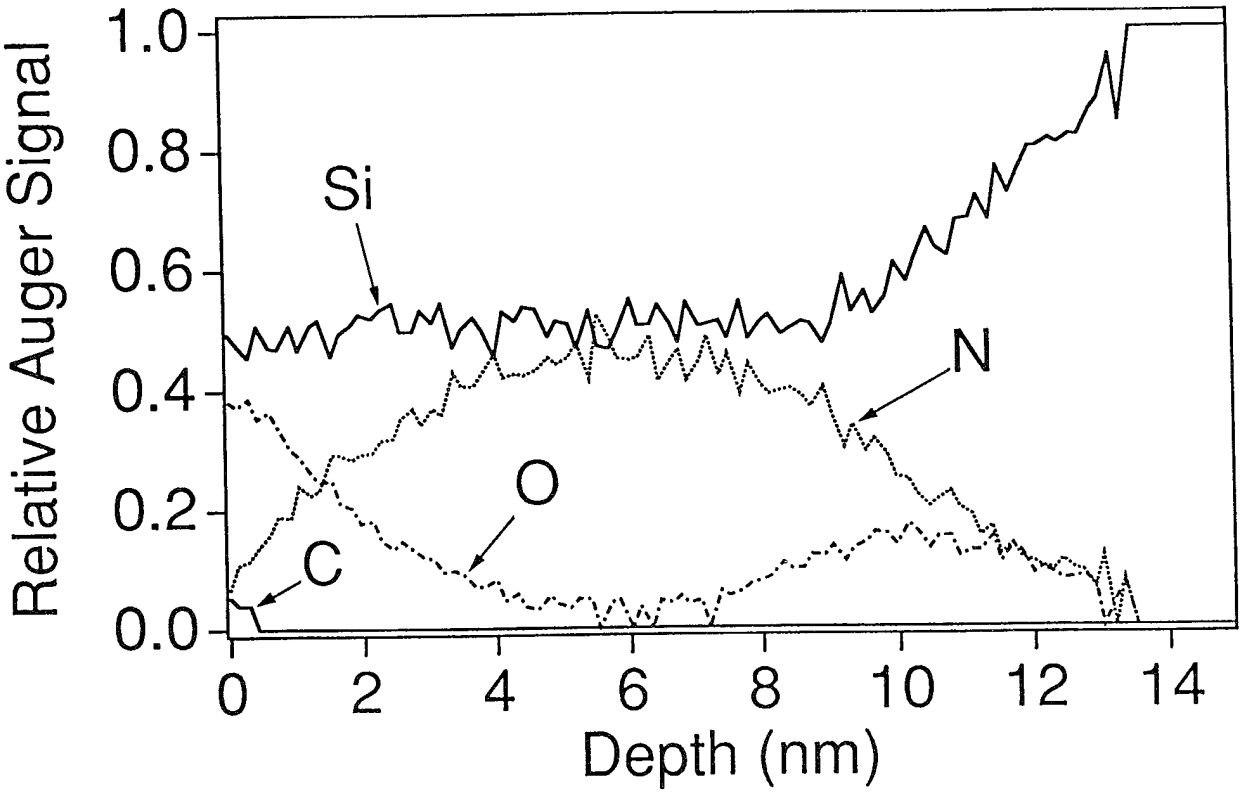
Relative Auger Signal
1.0
0.8
0.6
0.4
0.2
0.0
Si
N
O
C
0
2
4
6
8
10
12
14
Depth (nm)

Fig. 5b

14. Sputtering of trace elements on silicon surfaces

Sputtering and migration of trace quantities of transition metal atoms on silicon

Diane Pedersen and Robert A. Weller

Vanderbilt University, Nashville, TN 37235

Martha Riherd Weller and Victor J. Montemayor

Middle Tennessee State University, Murfreesboro, TN 37132

J.C. Banks and J.A. Knapp

Sandia National Laboratories, Albuquerque, NM 87185

Abstract

We have investigated the behavior of low levels of transition metal atoms on silicon surfaces subject to nitrogen bombardment. Submonolayer coverages of gold, iron, copper, molybdenum, and tungsten were deposited on <100> silicon surfaces. Samples were analyzed using 270 keV He^+ time-of-flight backscattering before and after irradiation with 6 mC of 270 keV N^+ at current levels in the hundreds of nanoamps. The yield of sputtered metallic atoms ranged from 1.0×10^{-3} per incident nitrogen ion to 3.3×10^{-3} per incident ion. Lower yields were correlated with migration of the metallic species into the silicon. The implications for ultra-high sensitivity measurement of contamination on silicon wafers by time-of-flight heavy-ion backscattering spectrometry are discussed.

Introduction

Improving the sensitivity of surface analytical techniques to metallic contaminants is of vital importance to the semiconductor industry. Heavy-metal contamination present in materials and arising from processing and cleaning operations is detrimental to devices because it results in defects which limit wafer yields and compromise circuit operation. In the near future, new generations of semiconductor devices will require increasing efforts at detecting and eliminating such contamination. Areal densities of surface metallic impurities as low as 10^8 atoms/cm^2 may hinder circuitry performance [1,2], and the detection of levels below 1×10^9 atoms/cm^2 will probably be necessary by the year 2000 [3].

Extensive efforts have been made to develop or modify surface analytical techniques to enhance sensitivity to trace species. Researchers have been able to attain sensitivities of about 5×10^9 atoms/cm^2 for Fe using total reflection X-ray fluorescence spectrometry without using chemical techniques to concentrate the material to a small spot [3,4]. Also impressive are the improvements in sensitivity resulting from optimization of time-of-flight backscattering spectrometry [1]. To optimize sensitivity, the yield of real counts must be increased while background counts are reduced. The use of heavy ions at energies lower than those used in conventional Rutherford backscattering increases the yield since the scattering cross section is increased. Medium energy (a few hundred keV) time-of-flight backscattering with heavy ions can provide a sensitivity to trace elements which is improved by a factor of 10^3 relative to that which is possible with conventional Rutherford backscattering [1].

As the sensitivity of surface analytical techniques is improved, other factors which limit sensitivity to surface species come into play. For techniques which rely on backscattering of incident ions, the ultimate limit to sensitivity may be imposed by the sputter removal of the material of interest [3,5,6]. The same physical processes that enhance sensitivity for medium energy backscattering also govern sputtering yields. In particular, the increase in scattering cross section which occurs at low incident beam energies and for higher Z incident ions yields more

backscattered particles, but also results in greater damage to the target near the surface and larger sputtering yields.

Many expressions and definitions for detection limits in experiments involving Poisson counting statistics have been proposed [7]. We prefer to estimate the optimum sensitivity in the presence of sputtering by requiring that the fractional statistical uncertainty, ε, of the measurement be equal to the fraction of surface material that is sputtered away [6]. We can write the fractional statistical uncertainty as

$$\varepsilon \equiv \frac{\sqrt{C+2B}}{C} = \frac{\Delta\rho}{\rho} \tag{1}$$

where ρ is the areal density of the surface species, C is the yield of backscattered particles, and B is the background in the region of interest. The yield of backscattered particles is given by

$$C = N\sigma\rho\Omega\eta \tag{2}$$

where N is the number of incident projectiles, σ is the differential scattering cross section, Ω is the solid angle of detection, and η is the efficiency of the detector. The number of sputtered surface atoms within the area A irradiated by the beam is $NP(\rho)$, where $P(\rho)$ is the number of sputtered atoms per incident ion as a function of surface coverage. Applying the requirement that ε must equal the fraction of surface material which is sputtered away, we have

$$\varepsilon = \frac{NP(\rho)}{\rho A} \tag{3}$$

The resulting equation for the minimum concentration, ρ_{min}, detectable in a backscattering measurement is

$$\rho_{min}^2 = \frac{1+\sqrt{1+8\varepsilon^2 B}}{2\varepsilon^3} \cdot \frac{P(\rho_{min})}{A\sigma\Omega\eta} \tag{4}$$

The function $P(\rho)$ is not known *a priori*. The simplest assumption for $P(\rho)$, where ρ is substantially less than a monolayer, is that it varies linearly with coverage, where

$$P(\rho) = k\rho \tag{5}$$

defines the constant of proportionality. We can estimate k by making the further assumption that trace atoms are removed randomly via collision cascades dominated by substrate atoms, and that

the number of trace atoms removed is proportional to their percentage representation in the affected volume of material [6]. This gives

$$P_{stoch}(\rho) \approx \frac{Y_s}{\rho_s} \cdot \rho \qquad (6)$$

where Y_s is the sputtering yield of the substrate, and ρ_s is the areal density of substrate atoms in the region from which sputtered atoms originate (typically the top 3 atomic layers).

In this experiment, we observed the behavior of dispersed metallic atoms on silicon substrates under bombardment by heavy ions with energies typical of those used for time-of-flight heavy ion backscattering spectrometry. By studying the behavior of several species of metallic atoms and determining experimental values for P, where

$$P_{exp} = P(\rho_{exp}) = \frac{A(\Delta\rho)_{exp}}{N} \qquad (7)$$

limitations to detection sensitivity arising from the sputter removal of the measured species can be estimated for a variety of trace elements.

Experimental Procedure

Two sets of samples were used in the measurements. One set was prepared by sputter deposition of submonolayer amounts of gold, copper, iron, molybdenum, or tungsten onto the entire surface of device grade, 1 inch, <100> silicon wafers. Prior to deposition, the wafers were ultrasonically cleaned first with acetone, then methanol, and finally rinsed with DI water. A 270 keV Ar^+ beam at 10 μA was used to sputter from thin metal foils onto the targets. The resulting metallic atom coverages ranged from 2.3×10^{14} atoms/cm^2 for Au to 6.9×10^{14} atoms/cm^2 for Mo. To check for uniformity of coverage, three spots on each sample were analyzed by backscattering with 270 keV He^+ normally incident on the target, at a scattering angle of 150° and with a beam spot size of 0.03 cm^2. A total deposited charge of 20 μC was used in the analysis of the gold, molybdenum, and tungsten deposits, and 54 μC was used in the analysis of the iron and copper deposits. Measured variations in initial coverage were less than 10% from spot to spot on an individual sample. The samples were then scanned with 6 mC of 270 keV N^+ at currents

ranging from 100 nA to 800 nA over an area encompassing approximately 0.4 cm^2. Thus, the number of incident N^+ ions was $(1 \pm 0.1)\times10^{17}$ ions/cm^2. (The uncertainty in this value is due primarily to uncertainties in determining the area of the scanned spot.) The purpose of scanning the nitrogen was to insure uniform irradiation and to minimize edge effects when reanalyzing the irradiated area. Following scanning, the samples were reanalyzed with He^+ in the same three locations that had been analyzed previously. In all cases, at least one of the analyzed spots was outside the scanned region and served as a control for the measurements.

The other set of samples was prepared by evaporating the same five metals onto 150 Å films of silicon which had previously been evaporated onto a graphite substrate. This sample structure was designed to allow us to measure the rate of sputter removal for both the silicon and the metal atoms. Areal densities for the metallic species ranged from 6.7×10^{14} atoms/cm^2 for gold to 2.3×10^{15} atoms/cm^2 for iron and tungsten. The samples were analyzed for uniformity by backscattering with a total analysis charge of 20 μC of 270 keV He^+. The samples were then scanned with 200 μC of 270 keV He^+ in an effort to prevent blistering of the silicon film by subsequent N^+ irradiation. The three spots were reanalyzed to verify that this scan did not erode the sample. Next the samples were scanned with 6 mC of 270 keV N^+. Beam currents and scan areas were both comparable to those used for the first set of samples. Finally, these samples were reanalyzed with He^+ after the N^+ irradiation.

For all backscattering analyses and for the nitrogen irradiation, the ambient pressure in the target chamber was in the high 10^{-8} Torr range and was due primarily to helium from the ion source and helium desorption from the ion pumps. Ambient pressure during the sputter deposition of samples was in the 10^{-9} Torr range. To prevent cross-contamination of samples due to sputtering or overlaying of the metallic species with sputtered silicon, samples were analyzed individually with only one sample in the vacuum chamber at a time.

Aside from a slightly discolored region corresponding to the area scanned by the nitrogen beam, there was little visible difference in the sputter-deposited samples before and after irradiation and analysis. Damage to the samples, again in the area scanned by the nitrogen beam, was much

more obvious on the evaporated samples. Scanning electron micrographs of these samples showed that the silicon film had blistered or flaked away in some areas. Thus, we were able to obtain only qualitative results from the evaporated Si film samples. Nevertheless, backscattering analyses from these samples support more quantitative results obtained from the sputter-deposited samples.

Results and Discussion

Figures 1-3 show the trace element features in the backscattering energy spectra for the sputter deposited samples before and after nitrogen irradiation. Areal densities of the materials before and after irradiation are given for each species in Table 1. The table also contains P_{exp} which is the experimentally determined value for the number of metal ions lost per incoming nitrogen ion, $P_{stoch}(\rho_{exp})$ which is the corresponding calculated quantity obtained from Eq. (6) and, for comparison purposes, Y_{bulk} which is the sputtering yield for the corresponding bulk metallic target subject to 270 keV N^+ irradiation. P_{exp} is obtained using Eq. (7). To obtain $P_{stoch}(\rho_{exp})$, we have used 2×10^{15} atoms/cm^2 as ρ_s for silicon, based upon an areal density of 0.68×10^{15} atoms/cm^2 for a Si (100) surface. Y_{bulk} is calculated using the expression of Matsunami *et al.* [8]. Estimated uncertainties in the table reflect statistical uncertainties in the data. Uncertainties due to current integration are much smaller than the statistical uncertainties while uncertainties in solid angle and detector efficiency have not been considered because they cancel in the calculation of P_{exp}.

There are several features of note in the figures. In all cases, there is a significant decrease in peak height for the metallic species after irradiation compared with the corresponding height before irradiation. With the exception of the Mo data (Fig. 3), there is also a noticeable shift of the peak centroid towards lower energies, consistent with migration of metallic atoms into the silicon. This shift is particularly noticeable for Cu, where it corresponds to approximately 90 Å in the substrate, and for Au, where it represents about 50 Å (see Fig. 1). Significant peak broadening is also evident for Cu and Au. The centroid shifts for W and Fe are both equivalent to about 20 Å. The statistical error in determining these centroid shifts is insignificant. However, from an analysis of the

unirradiated control spots we conclude that the uncertainties in these values are approximately 10 Å. Similar centroid movements were observed in the corresponding spectra obtained from the evaporated Si film samples.

Examining the data presented in the table, we note that values for P_{exp} seem to fall into three groups. Au and Cu have the lowest values while Mo has the highest value for P_{exp}. Values for Fe and W are intermediate. Considering this trend in light of the spectra in Figs. 1-3, we note that smaller values of P_{exp} seem to be correlated with the extent to which the deposited material has migrated away from the surface. Molybdenum shows the greatest loss due to sputtering and is the only element which has remained on the surface (Fig. 3). In contrast, Au and Cu have the smallest losses due to sputtering and the most significant migration into the silicon. In cases where we were able to estimate a sputter-removal rate for the evaporated Si film samples, we observed a similar correlation between migration and sputter removal.

An analysis of the data shows that the probability of removing an ion, P_{exp}, was lower than suggested by the stochastic argument of Eq. (6). However, for both sets of samples the relative ordering of the elements by amount of material lost was the same. P_{exp} was smaller than $P_{stoch}(\rho_{exp})$ by factors ranging from 0.08 to 0.14.

One potential ambiguity in our determination of P_{exp} arises from the fact that it depends upon the rate of diffusion of metallic atoms into the bulk during irradiation. The total number of nitrogen atoms incident on the target during an irradiation ($\approx 10^{17}$ ions/cm^2) is much larger than the number necessary for heavy-ion backscattering analysis of samples of this type. It is possible that most of the erosion occurs almost immediately, before significant diffusion occurs. If so, there would not be a simple correlation between deposited charge and erosion rates. Actual initial sputter yields for those materials which exhibit diffusion into the bulk would be higher than our results indicate. If this is the case, our estimates for sensitivity would be optimistic.

There are also several factors not included in the approximation for $P_{stoch}(\rho_{exp})$ which are expected to influence the yield of removed particles [5]. One is the mass difference between the surface materials and the substrate. Sputtering occurs when a collision cascade, generated by

energy deposited in the solid through nuclear collisions, intersects the surface and provides surface atoms with enough energy to escape. Energy transfer is most efficient in collisions between atoms of like mass, and therefore we may expect large mass differences between atoms of the substrate and those of the trace constituent to reduce the rate of sputter removal of the latter. Ion beam mixing of the surface and near surface layers of material will also reduce the rate of sputter removal by reducing the concentration of the trace species on the surface. Thus, the estimate of $P_{stoch}(\rho_{exp})$ from Eq. (6) is expected to be conservative. Surface binding energies also influence the rate of sputter removal. Depending on the binding energies of the trace species relative to the binding energies of Si atoms at the substrate surface, the rate of sputter removal could be either increased or decreased.

Using our results for P_{exp}, we can make some predictions about detection limits. We assume that Eq. (5) is applicable so that $P(\rho_{min}) = P_{exp}\ (\rho_{min}/\rho_{exp})$. The minimum detectable areal density for copper on silicon has been estimated previously [5] to be about 10^{12} atoms/cm^2 for nitrogen backscattering under conditions similar to those we have used. Our data suggest that in the absence of background sensitivities of about 1.5×10^{11} atoms/cm^2 should be attainable using a spectrometer with a solid angle of 0.8 msr and a beam spot size of 0.03 cm^2. This is with a detector efficiency of only about 4 percent for 270 keV N^+ backscattered from Cu. Eq. (4) indicates some modifications which can be made to improve upon this sensitivity. For example, the prototype HIBS machine at Sandia National Laboratories has a solid angle of 34 msr and an aperture defining a 1 mm diameter beam spot size. Under these conditions, our data suggest a sensitivity for Cu on Si of about 3.4×10^9 atoms/cm^2. A newer machine, developed by Sandia and Sematech, has 3 detectors, each with a solid angle of about 30 msr, and a beam spot size of 0.09 cm^2. Using this instrument, Knapp *et al.* [9] have recently reported sensitivities for Fe of 6×10^9 atoms/cm^2 for Fe on Si and 3×10^8 atoms/cm^2 for Au on Si, based on statistics which included background counts. Based on Vanderbilt detector efficiencies and assuming the optimum situation of no background, our data suggest that sensitivities would be limited by sputtering to 1×10^9 atoms/cm^2 for Fe and to 6×10^7 atoms/cm^2 for Au for the Sandia/SEMATECH instrument.

Conclusion

Measurements of the rate of sputter removal of several trace-elements on Si wafers have been conducted and yields have been found to be only about 12% as large as estimates based upon a simple stochastic estimate. At the observed levels, sputter removal of the trace elements under investigation is not a serious limitation to the sensitivity of time-of-flight backscattering spectrometry. Measurements indicate that beam-induced or enhanced diffusion plays a significant role in suppressing removal rates. Diffusion of trace atoms away from the surface, although very modest in extent, is nevertheless sufficient to move a large fraction of atoms out of the zone from which they may be sputtered.

With target sputtering now demonstrated not to be a significant limitation to the sensitivity of heavy ion backscattering, background produced by higher order scattering processes should be regarded as the determining factor limiting the ultimate trace-element sensitivity of the technique. Furthermore, theoretical models of trace-element sputtering must carefully take into account the location of the trace element atoms as well as their migration induced by exposure to radiation.

Acknowledgements

The authors wish to thank Marcus H. Mendenhall, James H. Arps and Kyle McDonald for assistance in the laboratory. This research was supported under a Department of Energy Contract DE-AC04-94AL85000 through Sandia National Laboratories and a Cooperative Research and Development Agreement (CRADA) with SEMATECH. Additional support was provided by the U.S. Army Research Office under contract DAAL 03-92-G-0037.

References

[1] J.A. Knapp and J.C. Banks, "Heavy Ion Backscattering Spectrometry for High Sensitivity", Nucl. Instr. and Meth. B79 (1993) 457-459.

[2] D. Deal, "Coming Clean: What's Ahead in Silicon Wafer Cleaning Technology", Precision Cleaning, Vol. II, No. 6, pp. 24-30 (1994).

[3] J.A. Knapp, J.C. Banks and B.L. Doyle, "Time-of-Flight Detector for Heavy Ion Backscattering Spectrometry", Sandia report SAND94-0391•UC-404, Sandia National Laboratories.

[4] U. Weisbrod, R. Gutschke, J. Knoth, and H. Schwenke, "Total Reflection X-Ray Fluorescence Spectrometry for Quantitative Surface and Layer Analysis", Applied Physics A53 (1991) 449-456.

[5] R.A. Weller, "The Impact of Spectrometer Efficiency on the Trace-Element Sensitivity of Time-of-Flight Medium Energy Backscattering", Nucl. Instr. and Meth. B99 (1995) 491-494.

[6] R.A. Weller, "Instrumental Effects on Time-of-Flight Spectra", Nucl. Instr. and Meth. B79 (1993) 817-820.

[7] L.A. Currie, "Limits for Qualitative Detection and Quantitative Determination", Analytical Chemistry 40, No. 3 (1968) 586-593.

[8] N. Matsunami, Y. Yamamura, Y. Itikawa, N. Itoh, Y. Kazumata, S. Miyagawa, K. Morita, R. Shimizu, and H. Tawara, Atomic Data and Nucl. Data Tables 31 (1984) 1.

[9] J.A. Knapp, D.K. Brice, and J.C. Banks, "Trace Element Sensitivity for Heavy Ion Backscattering Spectrometry", Proceedings of 12th International Conference on Ion Beam Analysis, Tempe, Arizona, 1995, Nucl. Instr. and Meth., submitted.

Figure Captions

Fig. 1 Au (a) and Cu (b), before and after irradiation with 6 mC of N^+. Charge used for the analysis (270 keV He^+ backscattering) was 20 μC for the Au and 54 μC for the Cu.

Fig. 2 Fe (a) and W (b), before and after irradiation with 6 mC of N^+. Charge used for the analysis (270 keV He^+) was 54 μC for the Fe and 20 μC for the W.

Fig. 3 Mo before and after irradiation with 6 mC of N^+. This spectrum was taken with 20 μC of 270 keV He^+.

metal species	ρ_{exp} (before) (10^{14} cm^{-2})	ρ_{exp} (after) (10^{14} cm^{-2})	P_{exp}	$P_{stoch}(\rho_{exp})$	Y_{bulk}
Au	2.3 ± 0.1	1.3 ± 0.1	0.0010±0.0003	0.0079	0.5
Cu	4.9 ± 0.2	3.6 ± 0.2	0.0013±0.0005	0.0169	0.33
Fe	5.7 ± 0.2	3.3 ± 0.2	0.0024±0.0006	0.0200	0.18
W	6.0 ± 0.1	3.6 ± 0.1	0.0024±0.0004	0.0207	0.11
Mo	6.9 ± 0.2	3.6 ± 0.2	0.0033±0.0007	0.0238	0.092

Table 1. Areal densities of surface metallics before and after irradiation with 6 mC of 270 keV N^+, experimental and stochastic (calculated from equation (6)) values of P, and bulk sputtering yields. Errors are statistical, and do not include other sources of error; such as solid angle, current integration, and detection efficiency.

a)

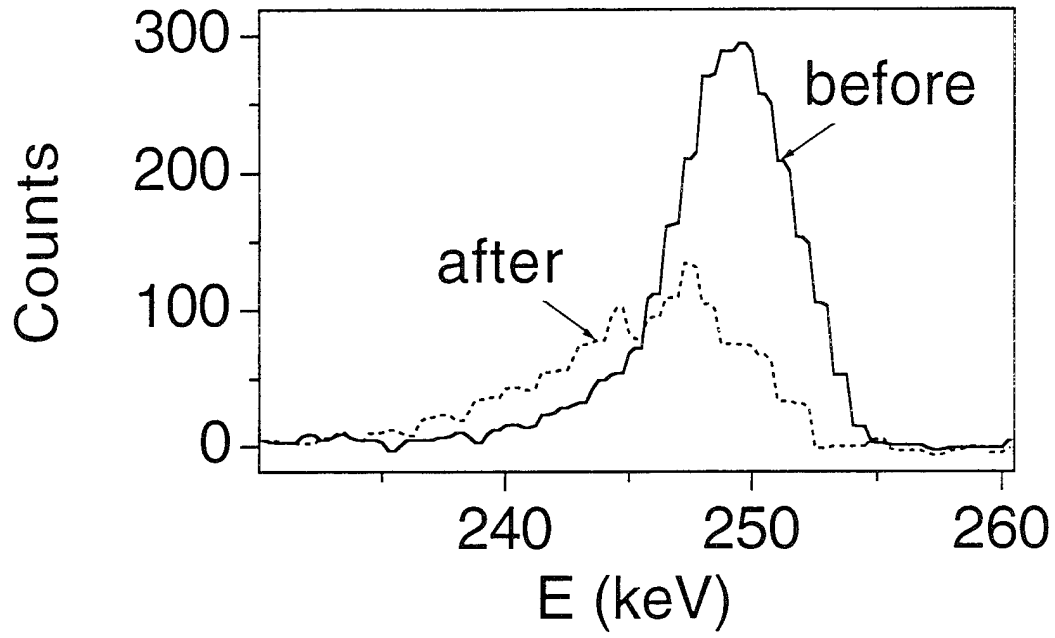
300
200
100
0
Counts
before
after
240
250
260
E (keV)

b)

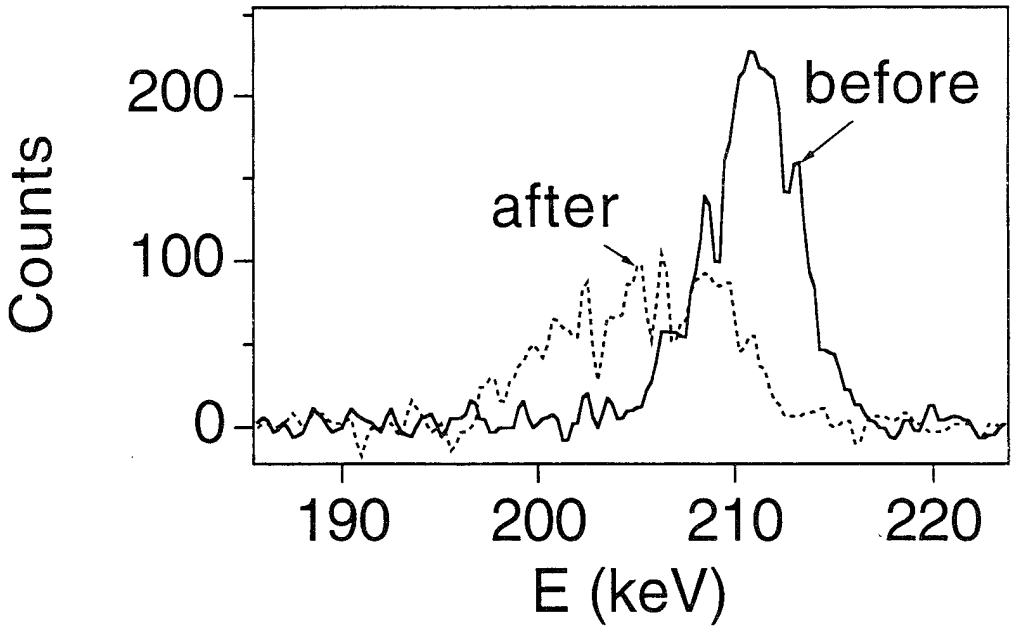
200
100
0
Counts
before
after
190
200
210
220
E (keV)

Fig.1

a)

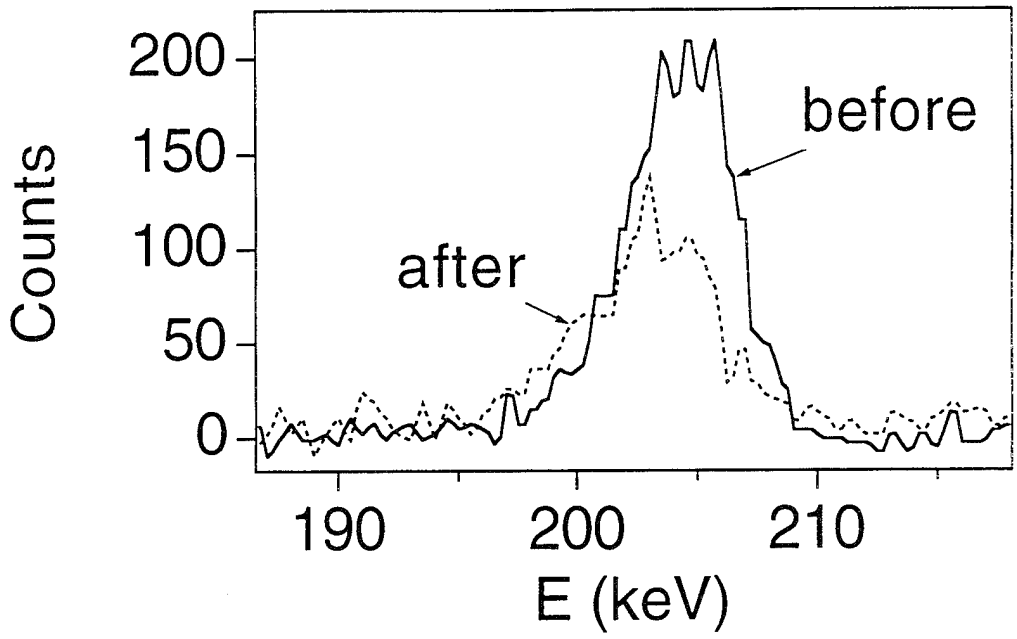
Counts
200
150
100
50
0
before
after
190
200
210
E (keV)

b)

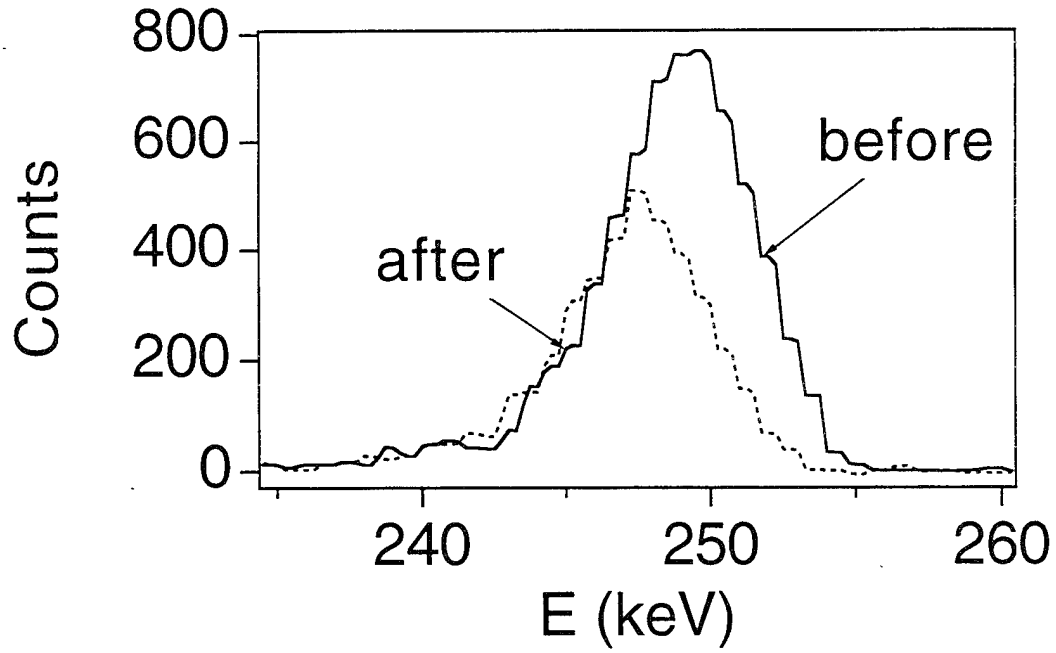
Counts
800
600
400
200
0
before
after
240
250
260
E (keV)

Fig. 2

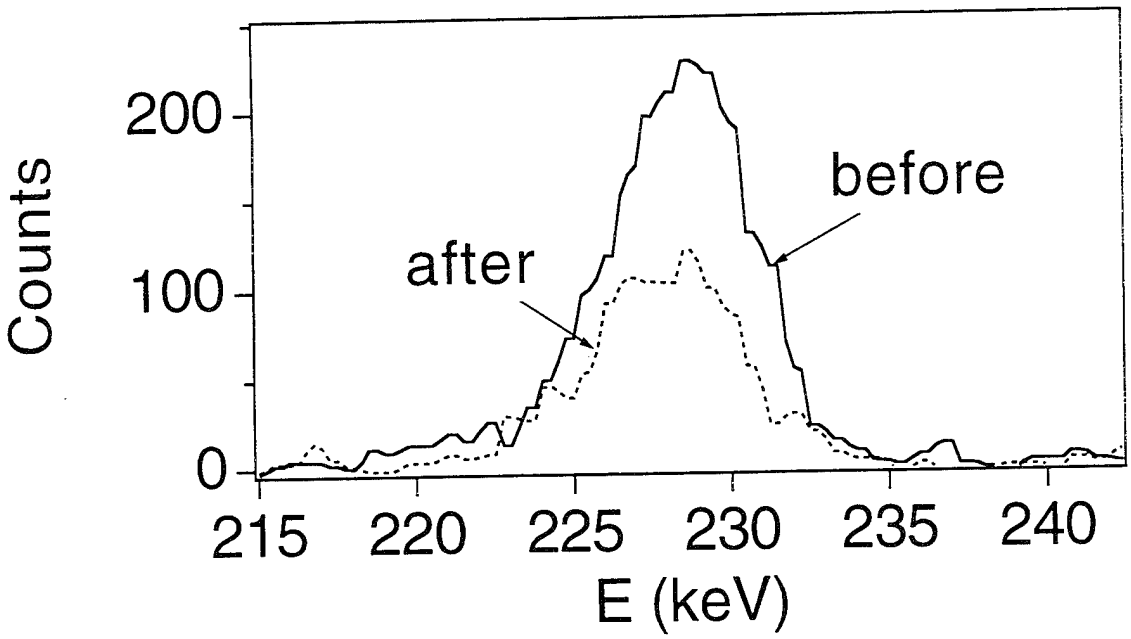

Fig. 3

15. Measurement of hydrogen in tokamak components

ELSEVIER

Journal of Nuclear Materials 220–222 (1995) 1130–1134

journal of nuclear materials

Effect of lithium wall conditioning on deuterium in-vessel retention in the TdeV tokamak

B. Terreault [a,b], H.Y. Guo [a,b], D. Kéroack [b], R.W. Paynter [a,b], W.W. Zuzak [a,b], G. Abel [a,b], M. Ennaceur [a,b], J.-L. Gauvreau [a,b], E. Haddad [a,c], L. Leblanc [a,b], G.G. Ross [a,b], H.H. Mai [a,b], N. Richard [a,c], B.L. Stansfield [a,b], TdeV Team [a], M. Caorlin [d], D.K. Owens [d], D. Mueller [d], S. Pitcher [e], P.H. La Marche [d], J.D. Strachan [d], J.H. Arps [f], R.A. Weller [f]

[a] *Centre canadien de fusion magnétique, 1804 Montée Ste-Julie, Varennes, Québec, Canada J3X 1S1*
[b] *INRS-Énergie & Matériaux, Université du Québec*
[c] *MPB Technologies, Inc.*
[d] *Princeton University, Plasma Physics Laboratory, Princeton, NJ 08543, USA*
[e] *CFFTP, Toronto, Canada*
[f] *Vanderbilt University, Nashville, TN 37235, USA*

Abstract

The effect of lithium wall conditioning in a boronized tokamak was investigated in ohmic discharges in the TdeV. In the course of 14 discharges, lithium was spread on the walls to a coverage of about 10^{21} atoms/m^2 by inserting a lithium-containing graphite crucible in the scrape-off-layer. Lithium caused an increase of some tens of percent in the wall pumping capacity during discharges, as seen from gas puffing and $H_\alpha + D_\alpha$ measurements. Post-shot wall outgassing also increased such that the short term in-vessel retention was only enhanced by about 20%. This increased retention level was confirmed by subsequent analysis of collector probe samples positioned in the SOL near the wall and was lower than one H or D atom per Li atom. Evidence of oxygen gettering by lithium was also found.

1. Introduction

Wall conditioning with lithium improved plasma performance and reduced edge density in TFTR [1]. The strong chemical affinity of lithium for hydrogen is a source of concern with respect to tritium inventory in tritium-fuelled tokamaks with a lithium-coated vessel. This experiment addressed that issue through a precise accounting of deuterium input and output and with the help of in-depth analysis of SOL collector samples. Lithium conditioning was performed by evaporation of Li from a graphite crucible heated by the plasma in the edge.

2. Experiment

Before this experiment, TdeV (Tokamak de Varennes) [2] had been fuelled with hydrogen and boronized with trimethylboron [3]. Thus, any deuterium detected in the present experiment was fresh gas rather than fuel implanted in the walls in previous experiments. This allowed a measurement of the short term D retention of the machine vessel, defined as the amount of fuel retained in the vessel at the end of the pumpdown between two shots. Two series of reproducible ohmic shots were used, with and without Li-conditioning. TdeV was operated with a double null

0022-3115/95/$09.50
SSDI 0022-3115(94)00488-9

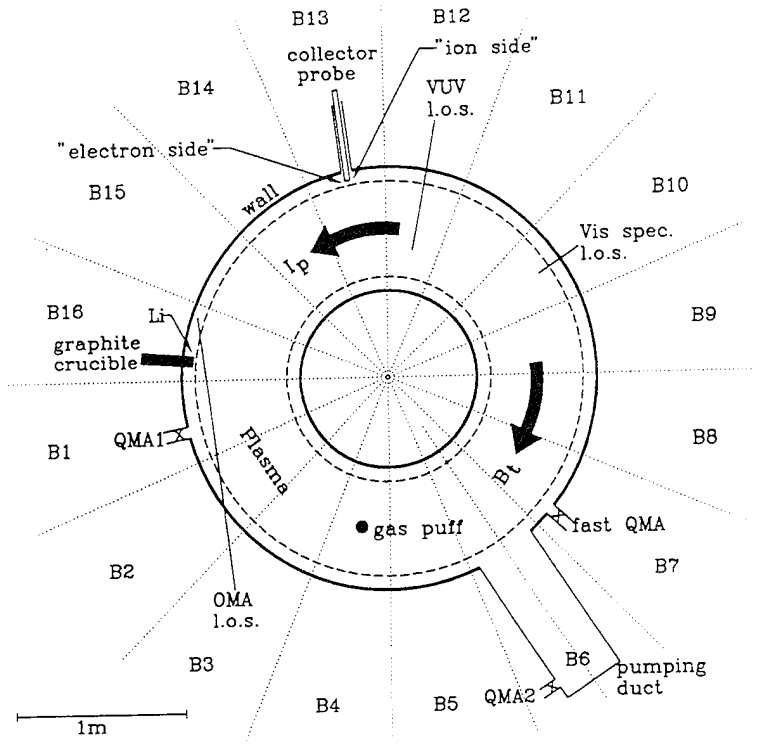

Fig. 1. Schematic top view of TdeV showing the location of the main components and diagnostics involved in the experiment and spectroscopy lines of sight (l.o.s).

divertor with $R = 0.875$ m, $a = 0.27$ m, $I_p = 210$ kA, $B_T = 1.5$ T, and $T_e(0) = 710 \pm 10$ eV. The experimental protocol consisted of the following steps:

(1) boronization, depositing a C + B layer ~ 100 nm thick, followed by 2 h of helium glow discharge, and with the SOL collector probe in edge;

(2) execution of 10 shots with H_2 fuelling, at $\bar{n}_e = 2.5 \times 10^{19}$ m^{-3} to remove helium from the walls and avoid confusion with D_2 in the mass analysers, with the SOL probe kept out of the vessel;

(3) execution of 10 shots with D_2 fuelling at the same $\bar{n}_e$, with the SOL probe out;

(4) execution of about 14 D_2-fuelled shots, with crucible and SOL probe inserted; to increase the ratio of valve fuelling to wall fuelling (higher D/H), $\bar{n}_e$ was increased to 3×10^{19} m^{-3};

(5) withdrawal of crucible and SOL probe, and sample transfer in argon to surface analysis.

The same procedure was repeated a month later except that the crucible carried no Li.

The experimental setup is schematically illustrated in Figs. 1 and 2. For the movable crucible and the SOL probe we define two sides: the ion side (i-side) facing the plasma current direction and the e-side. The crucible was located in Bay 16 on the midplane, while the SOL collector probe was in Bay 13, 5 cm below the midplane and 75° apart toroidally. On the crucible, a Li foil was held in front of a rectangular hole on the i-side; a trough was machined into the crucible, such that molten Li would flow into it by gravity but could

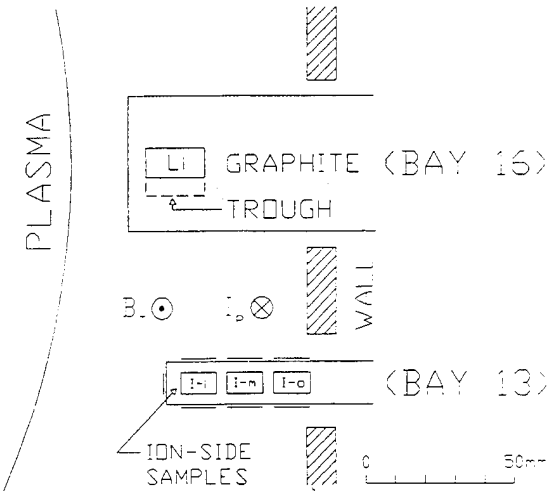

Fig. 2. Vertical sections in Bays 13 and 16, showing the crucible and the collector probe. The Li foil is exposed to the plasma through a hole in the cylindrical graphite crucible and is also heated by contact with the graphite. The Inconel sample holder has a square section.

escape if evaporated. The foil had been mounted and put under vacuum as quickly as possible after extraction from its container and removal of its protective mineral oil layer with hexane. There was a 1 m length along field lines between the SOL probe and the Li foil. The SOL probe temperature increase during the 1 s shots is 20–30° [4]. The probe was biased at −50 V and the ion saturation current monitored to check the shot-to-shot reproducibility of the edge ion flux, which was within ±1%. A biased probe also retains more of the incident flux [4]. The i- and e-sides of the probe each held three ATJ graphite samples, with additional silicon samples on top, bottom and tip (Fig. 2).

The presence of Li in the plasma was monitored by an optical multichannel analyser (OMA in Fig. 1) tuned to the LiII line at 5485 Å and viewing the plasma very near the crucible tip, and by one visible (5485 Å) and one VUV (1493 Å) spectrometer located far from the Li source. The amount of D_2 injected at each shot, I_D, was determined by PVT-measurements in the upstream reservoir and by a flow measurement in the piezo valve [5]. The error on I_D is ±3%. The H_2, HD and D_2 partial pressures were measured continuously during and between shots by one fast and two slow quadrupole mass analysers shown in Fig. 1. The fast QMA was differentially pumped and magnetically shielded and scanned one spectrum in 0.1 s, starting 1.5 s before and ending 23 s after the beginning of the shot. The QMA1 and QMA2 analysers acquired spectra at the rate of one scan in 2 s. All QMAs had been calibrated in the whole operating pressure range. The effective pumping speeds had been measured for H_2 and D_2 and were interpolated linearly for HD. Partial pressures and pumping speeds were combined to yield the amount of H and D atoms exhausted, E_H and E_D, by integration over the shot and pumpdown duration. The uncertainty on E_H and E_D is ±10%.

The amount of H and D retained by the graphite samples was measured by pulsed laser desorption (PLD) [6]. Li was quantitatively profiled by XPS combined with Ar ion beam etching. H, D, Li, C, B, O and metals were also profiled by AES, RBS, ERD [7,8] and SIMS.

3. Results

The data shown in Fig. 3 are averages on each shot between 0.3 s and 0.8 s, during the discharge flat-top. The crucible was inserted on the third shot shown, at a tip-to-separatrix distance of 13 mm. A very strong Li influx took place. Plasma-TV pictures indicated an excessive crucible temperature, with ejection of solid particles (but no plasma disruption). Spectroscopy, radiated power (P_{RAD}) and X-ray signals also showed an injection of carbon and heavier atoms (probably remaining from crucible machining). On the next two shots the crucible was retracted to 15 mm and 18 mm, where it remained thereafter. From the TV images, the tip temperature was much higher than the Li boiling temperature in vacuum (344°C at 1 mPa [9]). On shot 11 the Li spectroscopy signals showed a Li burst during the plasma current ramp-up. Thereafter, the Li signals decrease. After shot 16, the crucible was removed; inspection revealed no Li remaining in the holder.

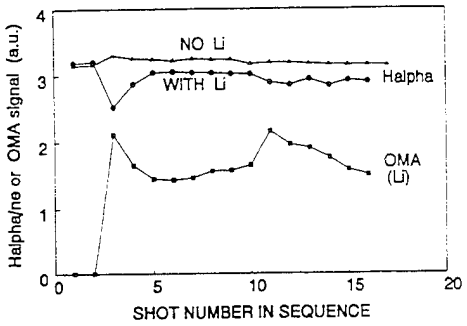

Fig. 3. Shot-by-shot evolution, during the experiments with and without lithium, of: (a) the LiII (5485 Å) line emission seen by an optical multichannel analyser (OMA), (b) $H_\alpha + D_\alpha$ emission.

Fig. 3 shows the $H_\alpha + D_\alpha$ signal from the most intense channel (upper X-point area); the data were normalized to $\bar{n}_e$ to account for small shot-to-shot variations in $\bar{n}_e$. The $H_\alpha + D_\alpha$ emission was 10 % lower with Li deposition, an effect already observed in TFTR [1]. This decrease was not caused by impurity influx, since it was accompanied by small drops in the loop voltage V_L (from 1.25 V to 1.20 V) and P_{RAD} (from 76 kW to 71 kW), and by an increase in gas puffing. The H_α emission shows the good reproducibility of TdeV plasma conditions in the first two shots in each series. This is confirmed by the V_L and P_{RAD} signals. The density and temperature profiles were not affected by Li deposition.

The amount of Li evaporated was 0.2 g or 1.8×10^{22} atoms. The ionization mean free path of Li atoms in the TdeV SOL is estimated to be 3 mm [10]; therefore, a large fraction of Li was likely transported as ions along field lines. If uniformly spread on all internal surfaces, it would correspond to $\sim 10^{21}$ atoms/m^2. However, a fraction was likely concentrated on the wall near the crucible and on the divertor plates. The XPS profiles of the middle samples on the i-side of the SOL probe (Fig. 4) show that the Li content in the sample after the experiment with Li-conditioning was ~15 at.%. An estimate of the Li-containing layer thickness by SIMS implies a total of $\sim 3 \times 10^{20}$ Li/m^2. The samples exposed to "no Li" shots (a month and 450 shots later) also contain 4 at.% Li in half as thick a deposit. This gives an estimate of the persistance of

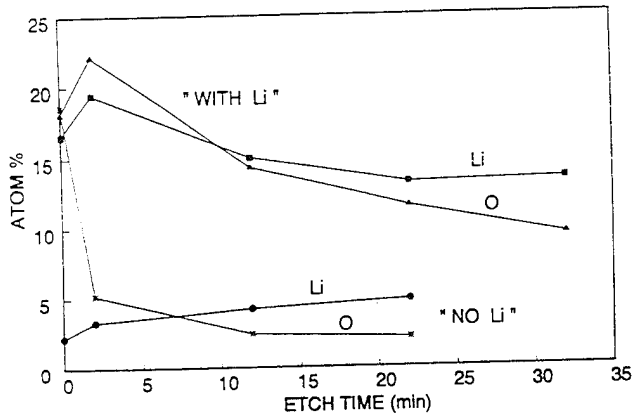

Fig. 4. XPS depth profiles of Li and O in ion-side middle samples. The nominal etch rate is 3 nm/min on aluminum. The sample consists mostly of carbon with some boron.

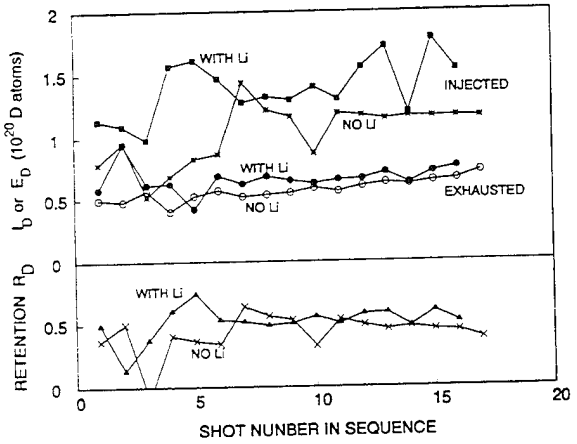

Fig. 5. Shot by shot evolution. (Top) Amount of D puffed I_D ($\pm 3\%$) and exhausted E_D ($\pm 10\%$) during and after the shot: (■) I_D with Li, (˙) I_D without Li, (●) E_D with Li, (○) E_D without Li. (Bottom) D retention fraction $R_D = (I_D - E_D)/I_D$: (▲) with Li, (×) without Li.

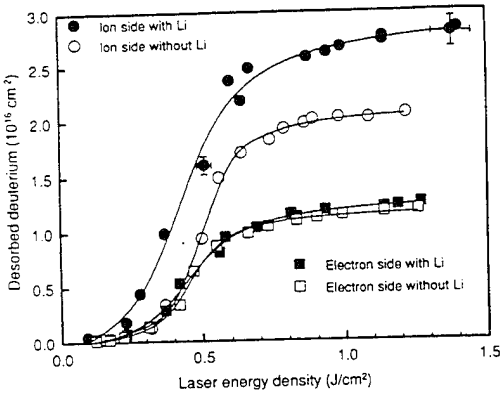

Fig. 6. Cumulative amounts of D atoms desorbed by laser pulses of increasing energy, versus the laser energy, for the middle samples, e-side and i-side.

Table 1
Deuterium PLD data, averaged over three graphite samples for each case. Units $(1 \pm 0.1) \times 10^{20}$ D/m^2

	Electron side	Ion side
With lithium	1.4	2.5
No lithium	1.5	2.0

deposited Li in tokamaks. We also note a clear quantitative correlation between the lithium and oxygen concentrations, which would suggest O gettering by Li.

Fig. 5 displays the shot-by-shot evolutions of I_D, E_D, and the short-term D retention fraction $= R_D = (I_D - E_D)/I_D$. The I_D required to maintain the same density is higher with Li deposition, while the H_α emission decreases, indicating a reduction of recycling during the shot. This is accompanied by a small increase in E_D, so that the short-term D retention is higher with Li deposition. The retention fractions averaged over each series of shots were $R_{D,Li} = 0.51 \pm 0.03$ with Li deposition and $R_{D,No} = 0.42 \pm 0.04$ without.

Fig. 6 shows the PLD data for the samples on the e- and i-sides in the middle of the holder. These graphs show the cumulative amount of D desorbed by successive laser shots of increasing energy. For the Li-conditioned samples, there is more retention on the i-side sample only. The averages for each group of three samples are given in Table 1. There is a 25% increase in retention on the i-side samples only. The increase in D retention associated with Li-conditioning was about 5×10^{19} atoms/m^2, much smaller than the Li coverage of $(3\text{–}10) \times 10^{20}$ atoms/m^2. Admittedly, there is also about 4 times more H than D in the samples, but the increase in the H content with Li is only $\sim 8\%$, because a large H inventory was present in the boronization layer before the experiment. Thus, it appears that Li did not permanently bind H isotopes with the full efficiency expected from LiH formation.

4. Summary

In the course of 14 ohmic shots, tens of monolayers of lithium were spread onto the walls of TdeV using a Li-containing crucible positioned in the SOL. There was evidence that Li was evaporated and transported by the plasma. Evidence of oxygen gettering by Li in collector samples was also found. An appreciable reduction in D recycling and concomittant enhancement of the D retention at the end of shot occurred. An increase in post-shot outgassing was also observed, such that the short-term D retention in the walls increased by at most 20%. The increment in short-term retention of both H and D due to Li was only $\frac{1}{10}$ to $\frac{1}{3}$ of the number of Li atoms in the walls. Therefore,

Li-conditioning is not likely to cause a pronounced increase in tritium vessel inventory in T-fuelled boronized devices.

Acknowledgements

We wish to thank D. Desroches, Y. Drolet, Y. Leblanc and S. Savoie for their remarkable technical contributions.

The authors at the Centre Canadien de Fusion Magnétique in Québec and the TdeV Group were supported by AECL, Hydro-Québec and INRS. The authors at the Plasma Physics Laboratory of the Princeton University were supported by US DoE contract DE-AC02-76-CH03073. The authors a the Vanderbilt University were supported by US Army Research Office contract DAAL-03-92-G-0037.

References

[1] J.A. Snipes et al., J. Nucl. Mater. 196–198 (1992) 686.
[2] R. Décoste et al., in: Controlled Fusion and Plasma Physics (18th Europ. Conf., Berlin, 1991) part I, p. 141.
[3] B. Terreault et al., J. Nucl. Mater. 200 (1993) 50.
[4] H. Y. Guo and B. Terreault, Plasma Phys. Control. Fusion 35 (1993) 1597.
[5] S.C. Bates and K.H. Burrell, Rev. Sci. Instr. 55 (1984) 934.
[6] R. Boivin, G.G. Ross and B. Terreault, J. Appl. Phys. 73 (1993) 1936.
[7] G.G. Ross and L. Leblanc, Nucl. Instr. and Meth. B 62 (1992) 484.
[8] J.M. Arps and R.A. Weller, Nucl. Instr. and Meth. B 79 (1993) 539.
[9] Y.S. Touloukian, in: A Physicist's Desk Reference (Amer. Inst. Phys., New York, 1989) p. 338.
[10] R.L. Freeman and E.M. Jones, Report CLM-R 137, Culham Laboratory, UKAEA, Abingdon, UK, 1973.

16. H sensitivity and depth resolution of forward-recoil spectrometry

Determination of the hydrogen sensitivity and depth resolution of medium-energy, time-of-flight, forward-recoil spectrometry

James H. Arps* and Robert A. Weller†

Vanderbilt University, Nashville, Tennessee 37235

Abstract

Medium energy time-of-flight forward recoil spectrometry has been developed recently as a complement to conventional ion beam analysis methods such as nuclear reaction analysis and elastic recoil detection. Here we report measurements of the minimum detectable surface concentration and near surface depth resolution for hydrogen by forward recoil spectrometry using a number of beam species and energies. The primary physical limitations encountered in these measurements are identified and discussed. Using an 810 keV Ar^{3+} beam, H on a carbon substrate can, in principle, be detected at areal densities as low as 1×10^{13} H/cm^2. A 540 keV O^{2+} beam has been found to be a suitable choice for depth profiling of H in Si achieving a resolution of approximately 6 nm near the surface. Examples are given which demonstrate the utility of the technique for hydrogen profiling.

* Present address Southwest Research Institute, San Antonio, TX.

† Corresponding author. e-mail: weller@vuse.vanderbilt.edu.

1. Introduction

Elastic recoil detection (ERD) and nuclear reaction analysis (NRA) are two methods widely used for the measurement of hydrogen in materials. Detection sensitivity and depth resolution are the primary attributes usually considered in assessing the capabilities of these ion beam analytical techniques and are often used as benchmarks for comparison. Szilagyi, *et al.*, have reported an optimized depth resolution of 2 nm for ERD using a 2.5 MeV C beam [1]. Nagai

and coworkers claim a detection limit of 2×10^{12} H/cm^2 based on the measurement of a single recoil atom [2]. In NRA, a near-surface depth resolution of 5 nm and a bulk sensitivity of less than 10 ppm can be achieved for hydrogen using the $^{15}N(p, \alpha\gamma)^{12}C$ reaction [3,4].

Medium energy time-of-flight forward recoil spectrometry has also been demonstrated to be a suitable method for determining the light element composition at or near the surface of a material [5]. A number of advantages may be realized over the methods noted above. A smaller, less expensive accelerator is needed, while good depth resolution near the surface is achieved due to the favorable timing properties of the time-of-flight spectrometer. Because the technique is sensitive to the velocity, rather than the energy of the recoil and scattered particles, separation and simultaneous identification of a number of light elements near the surface are possible without the use of an absorber foil. By using lower energy beams, sensitivity to light elements is increased due to the larger scattering cross sections and the total energy deposited in the sample is reduced. Recently, the first essentially nondestructive ion beam evaluations of radiation sensitive nitrocellulose and Langmuir-Blodgett organic thin films have been carried out using this technique [6].

This paper describes experiments designed to establish values for hydrogen sensitivity and depth resolution using medium energy time-of-flight (ToF) forward recoil spectrometry. A number of incident beam species and energies are considered in order to identify the optimal analysis conditions. Brief descriptions of the physical processes which affect sensitivity and depth resolution are given in order to identify the limiting factors associated with time-of-flight measurements. Lastly, the technique is applied in the measurement of buried H at C/Si interfaces and 500 eV H^+ implanted along random and channeled directions in Si.

2. Theoretical Considerations

Hydrogen sensitivity refers to the minimum surface or bulk H content that may be detected in a material at a prescribed confidence level. Ultimately, this requires the accumulation of a statistically significant number of counts associated with recoil H in the time-of-flight spectrum.

The number of real counts Y_R attributable to the feature of interest and the associated error σ_R determined by Poisson statistics are given by,

$$Y_R = Y_T - Y_B$$
$$\sigma_R = \sqrt{\sigma_T^2 + \sigma_B^2} = \sqrt{Y_R + 2Y_B} \qquad (1a,b)$$

where the subscripts T and B refer to the total and background counts and errors, respectively. In order for the measurement to be statistically significant, the number of real counts must be a factor α greater than the error in the measurement σ_R, where α=1, 2, or 3 at a 66, 95, or 99% confidence level, respectively. Solving for Y_R in terms of the number of background counts gives

$$Y_R = \frac{\alpha^2}{2}\left[1+\left(1+\frac{8Y_B}{\alpha^2}\right)^{1/2}\right] \qquad (2)$$

for the minimum detectable yield.

Background in a time-of-flight spectrometer is produced by random coincidences. These events occur when different particles initiate otherwise valid start and stop pulses. Hence, random coincidence background depends on the probability for generating valid start and stop events as well as the rate at which particles enter the spectrometer. The composition of the substrate is one factor contributing to this background because the flux of scattered particles depends on the mass of the substrate and, ultimately, the scattering cross section. The distribution of random counts is approximately uniform in time and increases linearly with current for a given total number of incident particles, since the rate of scattered particles scales directly with the rate of incident particles. Background subtraction, however, is particularly simple by using the kinematically inaccessible region of the spectrum as a baseline.

The solid angle and detection efficiency are fixed by the choice of geometry and spectrometer configuration (flight path, foil thickness, etc.), directly affecting the number of detected recoils. Two competing factors complicate the choice of beam species and energy for optimal sensitivity in analysis. While recoil H cross sections favor the use of high-Z analysis beams, the time-of-flight spectrometer's efficiency decreases with decreasing energy of the

recoil H. Sputtering of hydrogen by the incident beam is a further limitation on sensitivity and will be of the most concern in the use of a high-mass analysis beam. A formula has been proposed which considers sputtering along with a detailed treatment of the random coincidence background to arrive at a limit for sensitivity [7]. However, the magnitude of the sputtering contribution in the case of hydrogen is difficult to quantify since the rate of removal will likely be influenced by the host material. A reasonable order-of-magnitude estimate of the minimum detection limit imposed by sputtering might be an areal density of surface hydrogen equal to the ion dose used in the analysis. In most analyses by forward recoil spectrometry, it is likely that random coincidence background will be the dominant term affecting sensitivity.

The ability of a technique to resolve two distinct, same-element features separated by a certain thickness of material is characterized by the depth resolution of the system

$$\Delta x = \frac{\Delta E}{\varepsilon(E)} \tag{3}$$

$$\varepsilon(E) = \frac{1}{\cos\theta_1} K' S_i(E) + \frac{1}{\cos\theta_2} S_r(K'E) \tag{4}$$

where ΔE is the energy resolution and $\varepsilon(E)$ is the stopping cross section factor [8]. $S_i(E)$ and $S_r(K'E)$ represent stopping cross sections for the incident and recoil particles at the incident and recoil energies respectively. The energy resolution for a particular element may be inferred from the fwhm of a scattering peak corresponding to a monolayer or submonolayer coverage. Of course, for a thicker scattering feature, ΔE may be determined from the leading and trailing edge widths of the distribution.

Timing resolution, energy straggling, geometric broadening, and multiple scattering all contribute to the measured energy resolution. An electronic timing resolution of 1 ns will have a variable effect depending on the species mass and energy. For example, the contribution of

spectrometer timing to the energy spread of a 50 keV H recoil is approximately 1 keV. In general, the spread will increase for particles with higher energy and mass.

A geometric contribution to the energy resolution arises from the angular spread of scattered particles originating from a beam spot of finite size and sampled by a spectrometer with a finite aperture width. Particles detected at slightly different scattering angles will have different recoil energies. Paszti, *et al.*, discuss the optimization of an ERD system for depth resolution, and derive an expression for the geometrical effect [9]. A further approximation applies for scattering events in the near surface region.

$$\Delta E_g = 2K'E_0\Delta\gamma\tan\phi \tag{5}$$

where

$$\Delta\gamma = \frac{1}{D}\sqrt{w^2 + \frac{d^2\cos^2\theta_2}{\cos^2\theta_1}} \tag{6}$$

The angles θ_1 and θ_2 are the incident and exit angles measured from the surface normal. In the forward recoil configuration used in our laboratory, $\theta_1 = \theta_2 = 69°$, and $\phi = 42°$. The detector-target distance D is 30.5 cm, with an aperture width w = 0.42 cm and a typical beam width, d, of 0.5 cm measured in the scattering plane. The resultant broadening is equal to ~4% of the surface recoil energy, or 2 keV for 50 keV recoil H.

The ability to sense spatial variations in the elemental distribution depends not only on the intrinsic resolution and acceptance angle of the spectrometer but also on the energy straggling experienced by the ions in penetrating the target. The effect of energy straggling on the detector resolution is expected to be the dominant term, particularly for heavy ions, away from the near-surface region of the material. For numerical estimates of straggling at energies below 1 MeV the empirical formulae of Yang, O'Connor, and Wang may be used [10].

Multiple scattering gives rise to an uncertainty in energy as particles experience a gradual angular and lateral divergence in penetrating a material. The effect tends to dominate in situations where the incident or scattering angles with respect to the surface are very small (*i.e.*. large θ_1, θ_2 and small ϕ) and the penetration depth is large. Empirical estimates of the angular and lateral dispersion have been made in hydrogen ERD and RBS analyses aimed at optimized depth profiling [11]. These effects are minimal for the forward recoil geometry used in our laboratory because of the relatively large forward scattering angle. For instance, the angular spread experienced by 810 keV Ar traveling through 10 nm of Si contributes only 2 keV to the energy resolution, much less than the energy straggling for this thickness.

Multiple scattering also occurs when the incident or recoil species experiences more than one large-angle elastic collision. Such collisions, which add up to a net deflection of 42°, tend to produce particles with larger final energies than single scattering events. In a forward recoil time-of-flight spectrum, a small background tail is often seen to extend in front of the leading edge of a thick target recoil or scattering feature.

3. Experiment and Results

3.1 H Sensitivity Measurements

Detection limits for surface H on C and Si substrates were determined using 270 keV He^+, C^+, and Ar^+, 540 keV O^{2+} and Ne^{2+}, and 810 keV Ar^{3+} ion beams. Clean samples of silicon and graphite were analyzed in a bakable, hydrocarbon-free, stainless steel vacuum chamber at a pressure of approximately 2×10^{-8} Torr. Beam currents in the range 0.25-0.50 nA (with the exception of 2.5 nA for He) were used in order to minimize the random coincidence background in the measurements. The typical collection time for each spectrum was 30 minutes. Small, well separated peaks, attributable to surface H were observed in each spectrum. The minimum H yield was determined using Equation 2 at 99% confidence (α=3). From each spectrum, the number of background counts in the surface peak Y_B was computed by multiplying the measured peak width in channels by the average number of background counts per channel in a nearby, but

kinematically inaccessible region. Finally, the areal density of surface H was computed using the appropriate recoil cross section, spectrometer efficiency η, and solid angle.

The results for measuring H on carbon with various beams are compared in Table 1. The lower mass C substrate limits the flux of scattered beam particles and substrate recoils by more than a factor of three compared with the Si substrates. In some cases, such as the scattering of Ar from C, an angle of 42° is larger than the kinematic maximum for binary collisions. The large recoil cross section and reasonable H detection efficiency favor 810 keV Ar^{3+} for the sensitive measurement of surface H. It is important to note that by acquiring a spectrum over the span of an entire day, an order of magnitude additional charge could be applied at the same current. Such a measurement would lower the detection limit by more than a factor of three. The implied sensitivity of ~1×10^{13} H/cm^2 is equal to or better than the best values reported using conventional ERD when differences in the definition of sensitivity used by various authors are considered.

3.2 H Depth Resolution Measurements

The depth resolution for near surface H may be calculated from the same spectra used for the H sensitivity measurements. After transformation of the spectrum from the time to energy domain, the hydrogen surface peak was fit to a Gaussian, with ΔE equal to the fwhm separation. Stopping powers computed as in ref. [12] were used to calculate the stopping cross section factor $\varepsilon(E)$ and the depth resolution Δx was then determined. The resulting values are compiled in Table 2. The measured energy widths are generally consistent with the estimated contributions due to timing resolution and geometric broadening. No substantial improvement in the resolution is observed as a function of the analysis beam mass and energy. A possible explanation is that while the stopping cross section increases at higher energies the energy resolution of the spectrometer decreases. With increasing recoil H energy, the effects of spectrometer timing resolution and scattering geometry become more significant. The estimated

6 nm H depth resolution compares favorably with the results typically achieved by conventional ERD and NRA [1,3,4].

Since variation of the beam species and energy offers no clear advantage in depth resolution, issues of sensitivity and analyzable depth will play a defining role in choosing a beam for H profiling. The analyzable depth for light element profiling is reduced by heavier recoils or scattered beam ions from the surface having the same velocity (and flight time) as the recoils from deeper within the target. Figure 1 plots the analyzable depth as a function of beam energy for H in Si with the minimum energy before scattering determined by the point of interference from the next nearest scattering feature (either the scattered beam, for He, C, and O incident ions, or recoil C for Ne and Ar ions). Given that C and O produced generally similar results, a 540 keV O^{2+} beam was chosen for the sensitive depth profiling of H because it is easier to generate in our ion source.

An important test of any hydrogen depth profiling technique is the ability to resolve surface from buried hydrogen. To study this by medium-energy, time-of-flight spectrometry, five Si samples were cleaved from a 8-inch Si wafer, dipped in HF for ~2 minutes, then rinsed in deionized water. Carbon foils of varying thickness ($\rho = 2$ g/cm^3) were floated onto the surface of a water bath and drawn onto the Si samples. The carbon thicknesses stated by the manufacturer (ACF metals) were 1.8, 2.3, 3.0, and 5.0 μg/cm^2 with uncertainties of at least ±0.5 μg/cm^2. A significant concentration of H at the C/Si interface was observed, due perhaps to either trapped water or hydrocarbon contaminants introduced during preparation.

Figure 2 shows the time-of-flight and corresponding energy spectra from analysis of these samples by 540 keV O^{2+} at a deposited charge of 5 μC. Both the surface and buried H distributions are clearly resolved with the latter shifted lower in energy as the thickness of the C overlayer is increased. The measured positions of the buried H peaks were compared with calculations based on the standard energy loss equation

$$\delta E = K E_0 - E_c = \frac{d}{\cos\theta_1} K S_i(E_{in}) + \frac{d}{\cos\theta_2} S_r(E_{out}) \qquad (7)$$

where d is the carbon thickness and E_c is the position of the centroid. Values for the carbon layer thicknesses were determined by 810 keV Ar^{3+} forward recoil and 270 keV He^+ backscattering measurements. The experimental and calculated energy shifts and the measured foil thicknesses used in the calculations are given in Table 3. Agreement to ±15% is consistent with the uncertainties for the computed carbon foil thicknesses and energy losses, providing strong evidence that the hydrogen is confined to the interface. Based on estimates of the spectrometer timing uncertainty, multiple scattering, geometric broadening, and energy straggling, the energy widths of the buried H distributions are consistent with a thin hydrocarbon layer trapped at the C/Si interface.

A final demonstration of the application of forward recoil spectrometry to hydrogen profiling is the measurement of low energy proton implant distributions. For light ions with energies in the range 0.5-5 keV, the structure of a solid is known to strongly affect the mean projected range [13]. Experiments by Bourque, *et al.*, have determined the ranges and straggling of 1 keV deuterons in amorphous, polycrystalline, random and channeled Si [14]. Such measurements are particularly useful for comparison with TRIM [12] or other Monte Carlo simulations of low energy ion trajectories. Figure 3 compares time-of-flight and energy spectra for 0.5 keV H^+ implanted in randomly oriented (22.5° tilt) and channeled <110> Si. The two samples, prepared at the University of Quebec, have estimated peak H atomic concentrations of 10%. A control sample was also analyzed to identify the surface H contribution. As anticipated, the implanted range increases along the channeling direction. A mean projected range of 10 nm was estimated for the randomly oriented sample using TRIM and is consistent with the measured profile.

4. Conclusions

A number of buried and implanted hydrogen distributions have been measured by medium energy time-of-flight forward recoil spectrometry. Results show that this technique compares favorably with conventional ion beam analytical techniques in sensitivity and resolution for near

surface H. Minimum coverages of 1×10^{13} H/cm^2 can, in principle, be measured using an 810 keV Ar^{3+} analysis beam while a near-surface depth resolution of approximately 6 nm has been achieved with 540 keV O^{2+} ions. Further optimizations of the time-of-flight spectrometer and the scattering geometry should result in substantial improvement over these quoted values.

Acknowledgments

The authors are very grateful to Gilles Bourque and Bernard Terreault of the University of Quebec for their preparation of the H-implanted Si. This work was supported in part by the U.S. Army Research Office under contract DAAL 03-92-G-0037.

References

[1] E. Szilagyi, F. Paszti, V. Quillet, and F. Abel, Nucl. Instr. and Meth. B85 (1994) 63.

[2] H. Nagai, *et al.*, Nucl. Instr. and Meth. B28 (1987) 59.

[3] B. Maurel and G. Amsel, Nucl. Instr. and Meth. 218 (1983) 159.

[4] D. Endisch, H. Sturm, and F. Rauch, Nucl. Instr. and Meth.B84 (1994) 380.

[5] J.H. Arps and R.A. Weller, Nucl. Instr. Meth. B79 (1993) 539.

[6] J.H. Arps and R.A. Weller, Nucl. Instr. Meth. B99 (1995) 623.

[7] R.A. Weller, Nucl. Instr. and Meth. B79 (1993) 817.

[8] W.K. Chu, J.W. Mayer, and M.A. Nicolet, *Backscattering Spectrometry,* (Academic Press, 1978) p. 74.

[9] F. Paszti, E. Szilagyi, and E. Kotai, Nucl. Instr. and Meth. B54 (1991) 507.

[10] Q. Yang, D. J. O'Connor, and Z. Wang, Nucl. Instr. and Meth. B61 (1991) 149.

[11] J.S. Williams and W. Moller, Nucl. Instr. and Meth. 157 (1978) 213.

[12] J. F. Ziegler, J. P. Biersack and U. Littmark, The Stopping and Range of Ions in Solids, (Pergamon Press, 1985) p. 218.

[13] M. Hou and M.T. Robinson, Nucl. Instr. and Meth. 132 (1976) 641.

[14] G. Bourque, B. Terreault, G.G. Ross, and D. Theriault, Nucl. Instr. and Meth. B90 (1994) 175.

Table Captions

Table 1. Comparison of H minimum detection limits (N_H) for various analysis beams incident on a C substrate. The background counts in the surface peak (Y_B), minimum detectable yield (Y_R), deposited charge (Q), recoil cross section (σ_H), and effective solid angle ($\eta \cdot \Omega_H$) used in each computation are also provided.

Table 2. Effect of analysis beam on near-surface energy resolution (ΔE) and depth resolution (Δx) for H on a C substrate.

Table 3. Measured and calculated energy shifts, δE_{exp} and δE_{calc} for H at four C/Si interfaces. See corresponding spectra in fig. 2.

Figure Captions

Figure 1. Analyzable depth for H in Si as a function of beam species.

Figure 2. (a) Time-of-flight and (b) energy spectra of recoil H from Si surfaces covered by C layers of varying thicknesses: (a) bare Si, (b) 1.8 μg/cm^2, (c) 2.3 μg/cm^2, (d) 3.0 μg/cm^2, (e) 5.0 μg/cm^2. The ion beam was 540 keV O^{2+}.

Figure 3. (a) Time-of-flight and (b) energy spectra of recoil H from Si surfaces implanted with 500 eV H^+ along the [110] direction and in a pseudo-random direction. The beam was 540 keV O^{2+}.

Beam / Energy (keV)	Y_B (counts)	Y_R (counts)	Q (10^{12} ions)	σ_H (10^{-22} cm^2/sr)	$\eta \cdot \Omega_H$ (10^{-5} sr)	N_H (10^{13}/cm^2)
He / 270	37	31	31	.173	3.0	69
C / 270	9.5	18	3.1	10.2	2.1	9.8
O / 540	4.4	14	3.1	7.77	2.6	8.0
Ne / 540	7.5	17	1.6	18.2	2.4	8.8
Ar / 270	140	55	1.3	675	0.5	4.4
Ar / 810	7.3	17	1.0	92.1	2.1	3.0

Table 1

Beam / Energy (keV)	ΔE (keV)	$\varepsilon(E)$ (eV/10^{15} /cm^2)	Δx (10^{15} /cm^2)/ (nm)
He / 270	5.5	26.1	75.5 / 6.7
C / 270	3.5	23.2	54.1 / 4.8
C / 540	5.0	27.7	64.7 / 5.7
O / 540	4.5	25.6	63.0 / 5.6
Ne / 540	4.0	22.6	63.4 / 5.6
Ar / 270	2.5	16.0	56.0 / 5.0
Ar / 810	3.5	20.3	61.8 / 5.5

Table 2

Sample	C thickness (10^{17} atoms/cm^2)	δE_{exp} (keV)	δE_{calc} (keV)
b	1.0	8.5	7.1
c	1.1	9.8	7.8
d	1.8	12.3	12.8
e	2.3	18.7	16.3

Table 3

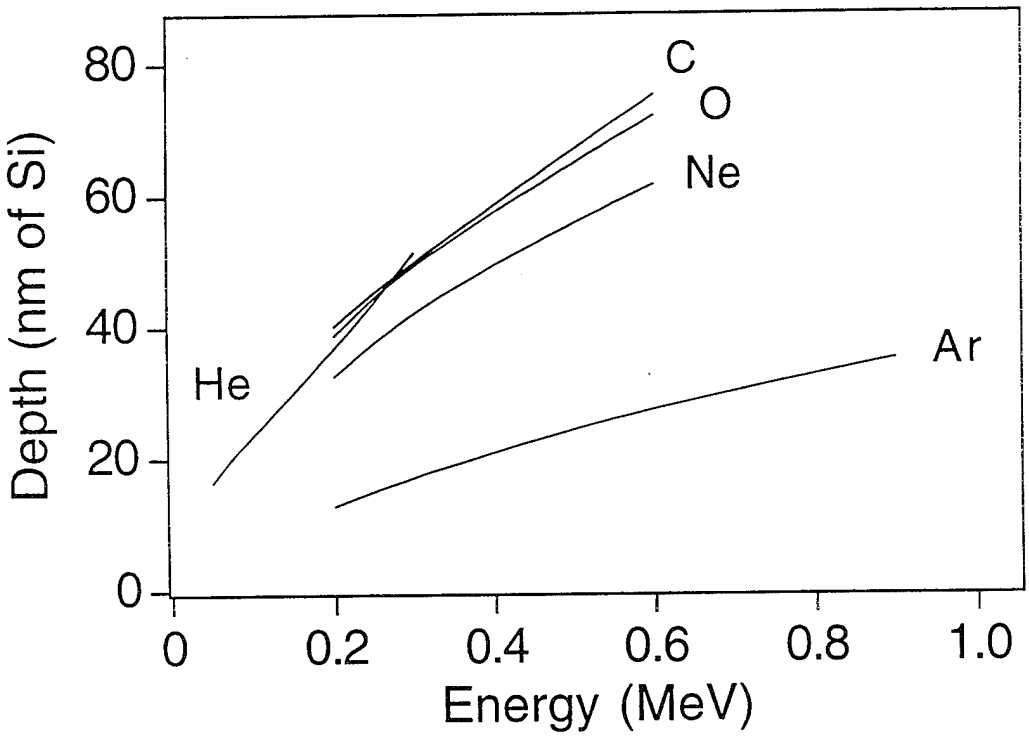

Figure 1

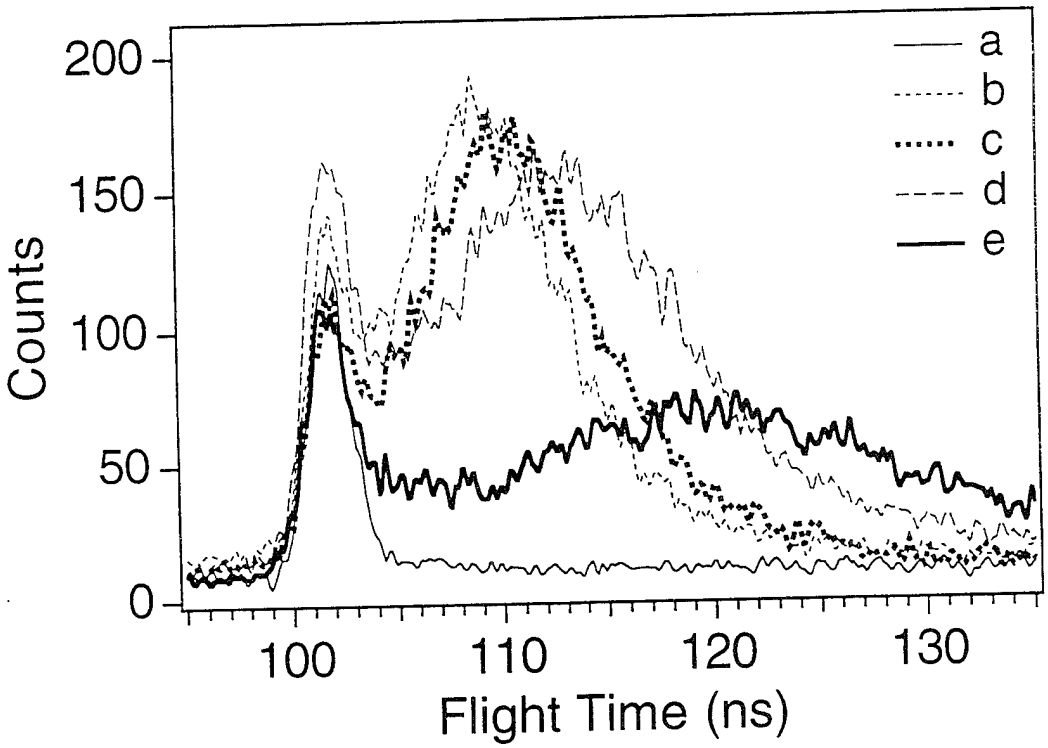

Figure 2a

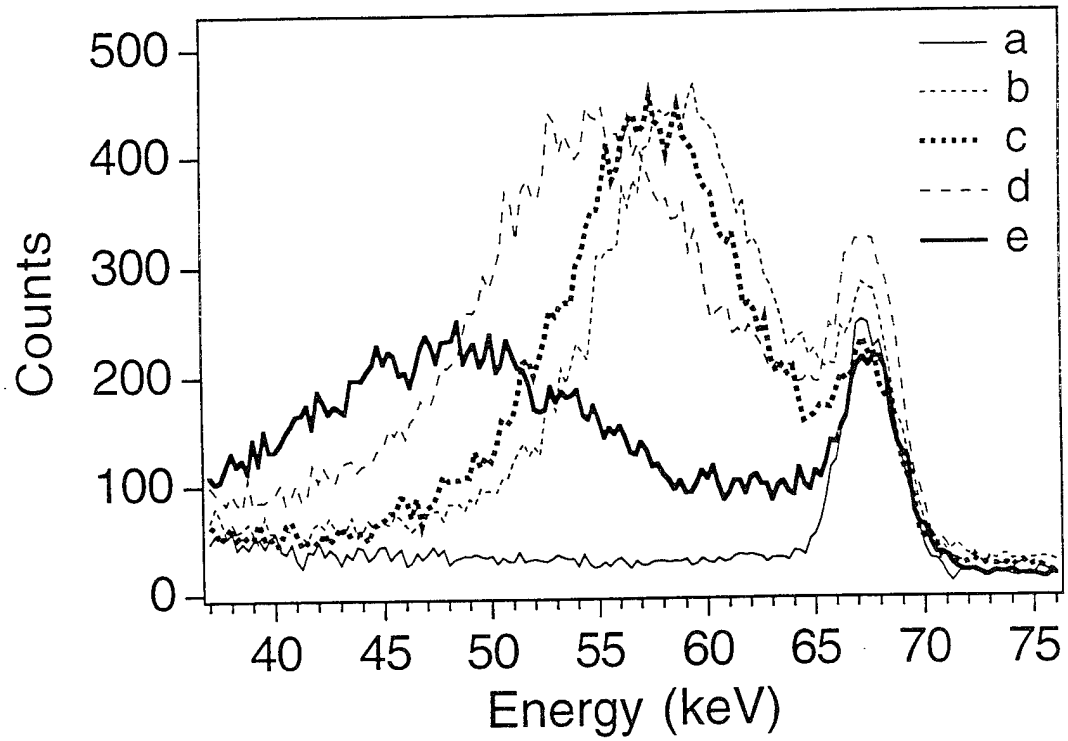
500
400
300
200
100
0
Counts
40
45
50
55
60
65
70
75
Energy (keV)
a
b
c
d
e

Figure 2b

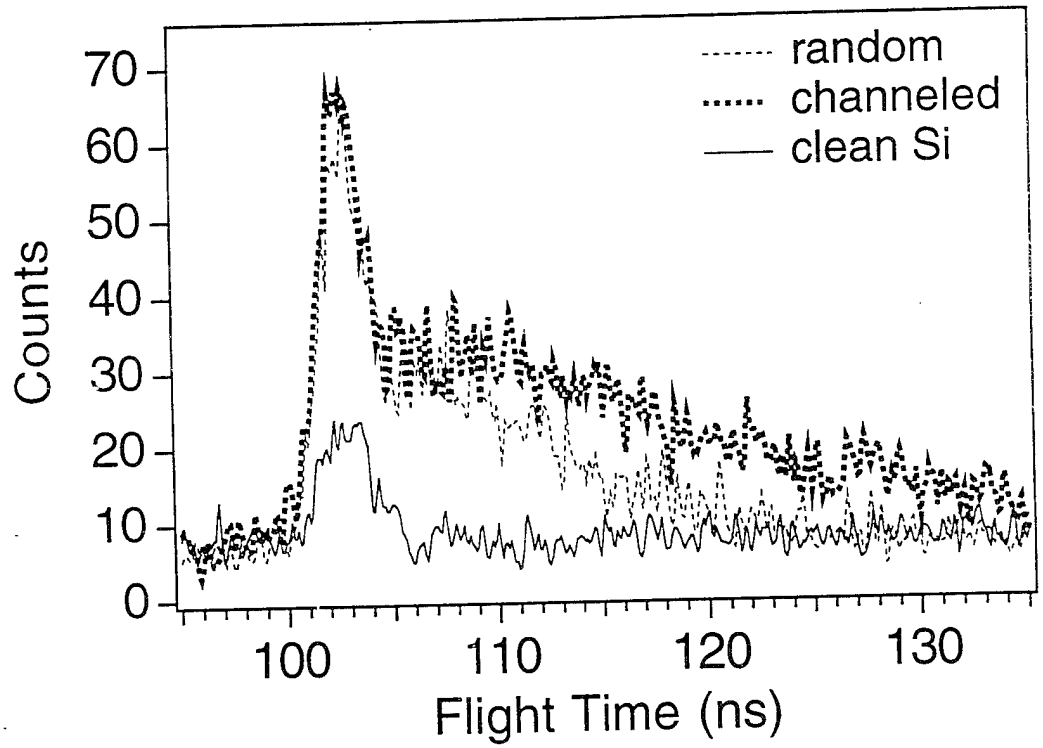
random
channeled
clean Si
Counts
70
60
50
40
30
20
10
0
100
110
120
130
Flight Time (ns)

Figure 3a

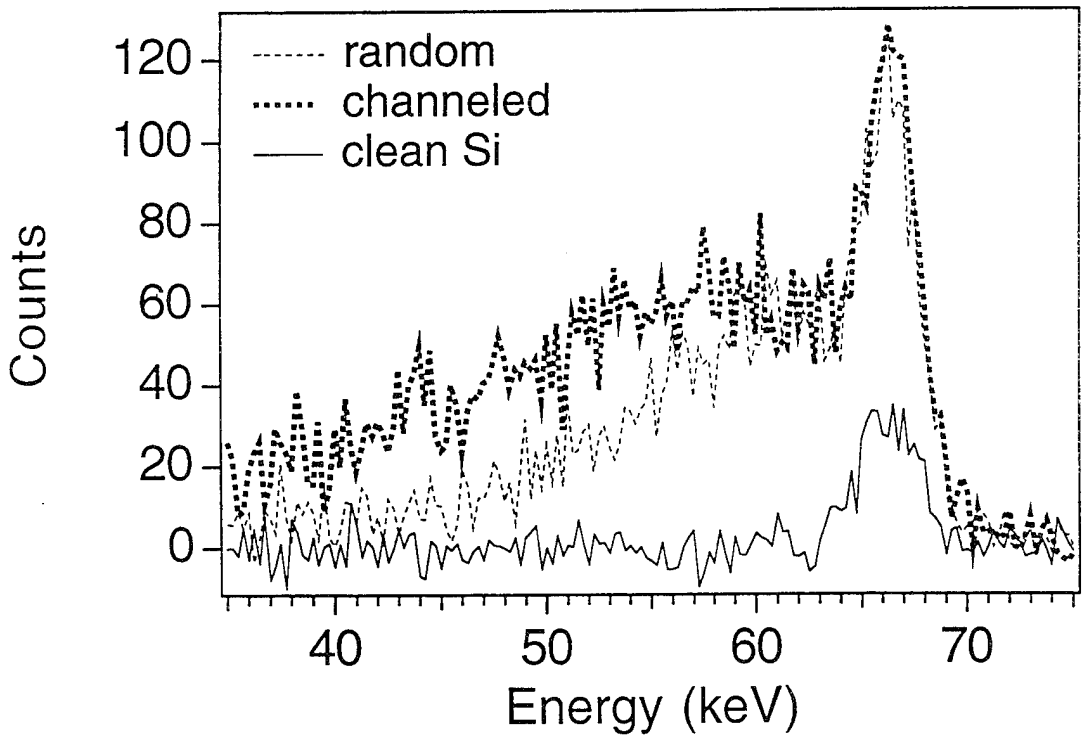
random
channeled
clean Si
120
100
80
60
40
20
0
Counts
40
50
60
70
Energy (keV)

Figure 3b